



Università degli Studi di Ferrara

DOTTORATO DI RICERCA IN "FISICA"

CICLO XXI

COORDINATORE Prof. Filippo Frontera

Internal polarized gas targets: systematic studies on intensity and correlated effects

Settore Scientifico Disciplinare FIS/01

Dottorando

Dott. Barion Luca

Tutore

Dott. Lenisa Paolo

Tutore Aggiunto

Prof. Ferretti Dalpiaz Paola

Anni 2006/2008

Dedicata a ...

Contents

1	Spin-physics and polarized antiprotons	3
1.1	The spin of the proton	3
1.2	Polarized antiprotons	7
2	The SpinLab facility in Ferrara	11
2.1	Unpolarized Atomic Beam Source (ABS1)	11
2.1.1	Dissociator	12
2.1.2	Vacuum chambers	12
2.2	Diagnostic system	14
2.2.1	Motor speed stabilization circuit	19
2.2.2	Time Of Flight (TOF)	22
2.3	Polarized Atomic Beam Source (ABS2)	25
2.3.1	Pumping system	25
2.3.2	Dissociator	27
2.3.3	Magnetic system	27
2.4	Data Acquisition System (DAQ)	30
2.4.1	ABS1	30
2.4.2	ABS2	35
2.4.3	Computer <i>spinlab6</i>	35
2.4.4	Fox Box	38
2.5	Ntuples	38
3	Elastic scattering of the ABS beam with residual gas. Evaluation of attenuation coefficients and cross-sections	41
3.1	Motivation	41
3.1.1	Historical background	41
3.1.2	Rest Gas Attenuation	43
3.2	Measurement of the attenuation coefficient A_n	44
3.2.1	Experimental procedure	46
3.3	Cross section evaluation method	56
4	New ideas part A: Finned injection tubes	59
4.1	Intensity of polarized internal targets	59
4.2	Finned injection tubes	60
4.3	Measurements	62
4.3.1	Injection tube conductance	62

4.3.2	Atomic beam intensity	64
4.4	Target thickness estimation	65
4.5	Comparison to simulations	66
4.6	Conclusions	69
5	New ideas part B: Trumpet nozzle	71
5.1	Introduction	71
5.2	Monte-Carlo simulations	72
5.3	Measurements	76
5.3.1	Procedure for data-taking	77
5.3.2	Data analysis and results	79
5.4	Conclusions	82
A	Atomic Beam Sources magnetic system	83
B	Beer law	87
C	Files for trumpet nozzle simulation program DS2G	93
C.1	read_1000.f	93
C.2	DS2GD-trumpet2b.TXT	95
D	Time Of Flight	107
D.1	Time Of Flight analysis procedure	107
D.2	Program sources	110
D.2.1	cleanup_single.csh	110
D.2.2	header.dat	110
D.2.3	template.ctr	111
D.2.4	conv.inc	111
D.2.5	labparam.inc	112
D.2.6	shared.inc	112
D.2.7	convolute.f	112
D.2.8	fitit.f	122
D.2.9	runfit.csh	124

Introduction

The work presented in this thesis has been performed in the frame of the PAX collaboration. PAX is the acronym of *Polarized Antiproton eXperiments*. The collaboration has proposed an experimental program to create a stored intense and polarized antiproton beam at the future facility FAIR (Facility for Antiproton and Ion Research) at GSI - Darmstadt, Germany. See for reference the technical report [1].

The polarizing method proposed is based on the spin selective scattering of an initially unpolarized antiproton beam, stored in a ring, passing many times through a gas of polarized protons. This spin-selective *filtering* is obtained using an internal polarized gas target, installed on the antiproton storage ring.

The *filtering* targets performance is crucial for the success of the PAX project. In particular, the experiment would highly benefit from an increase in the target thickness, on which, since more than 10 years, no substantial progresses have been accomplished.

These gas targets consist of a light tube, called *cell*, coaxial with the circulating beam and filled at its center with nuclear polarized atomic gas from an Atomic Beam Source (ABS). Due to wall collisions, the thickness of these targets is a factor 100 larger than the atomic jet alone. This technique, suggested by W.Haeblerli at the end of 1960s [2] has proven very successful in various experiments. Among others, it is worthwhile to mention HERMES, and its contributions to the understanding of the nucleon spin structure [3]. An exhaustive review of this technique is presented in ref. [4].

Gas targets have a high (80-90%) polarization without dilution and the polarization direction can be reversed in milliseconds. However, the experimental luminosity is limited by the low target thickness, typically $10^{14} \text{ atoms/cm}^2$. The thickness is limited both by the geometry of the cell and the maximum intensity available from the ABS that fills the cell.

This thesis has been dedicated to systematic studies on the limiting mechanisms of the target thickness and to propose new ideas for overcoming these limits; the tests have been carried out at the Spinlab laboratory of Università di Ferrara.

The beam attenuation in the focusing chambers is a limiting factor for existing and future ABS, not fully understood at present. This effect is due both to beam particle collision with the background gas particles (*rest-gas*) and to *intra-beam scattering*. The total scattering cross section for collisions of beam particles with *rest-gas* particles is the physical relevant quantity that allows to evaluate independently the *rest-gas* attenuation, disentangling this effect from *intra-beam scattering*. Up to now, no data or theoretical previsions exist on this cross section, in the temperature range of interest for ABS. In the frame of this thesis, this problem has been addressed. Using a combination of beam simulations and dedicated test bench measurements, the total scattering cross sections for atomic and molecular collisions of hydrogen and deuterium in the temperature range 200 – 300 K

have been extracted. These cross sections are reported for the first time in terms of relative velocity of the colliding particles. They are therefore physical quantities, independent from the different systems conditions and can be used to design new ABS. Besides ABS applications, the extraction of these cross sections is interesting in many physics fields, as astrophysics (transport phenomena), Bose-Einstein condensation, hydrogen masers, or polarized fusion [5][6].

Concerning new ideas to increase the target thickness, a study on the effect of a modified *injection tube* has been undertaken, adding radial fins to a traditional cylindrical tube. In this way, ideally, the incoming ABS beam is not affected, but the atoms diffusing back out the injection tube itself are partially obstructed, increasing therefore the target thickness. No improvement is foreseen for the PAX target geometry. On the other hand, from an analysis that takes into account the results of the simulations, compared with the measured data, for the first time a non-zero azimuthal component of the velocity of atoms of the beam has been demonstrated. This result has been published in [7].

More promising are the effects on the ABS hydrogen jet intensity of a *trumpet* nozzle, as suggested by W. Kubischta, who deduced a particular shape for the nozzle from Monte Carlo simulations. The nozzle has been produced in the Ferrara mechanical workshop and tested on the Spinlab test bench. At present the measurements confirm the trends foreseen with the simulations.

This thesis is organized as follows.

In the first section of Chapter 1 an overview of the physic motivations at the basis of PAX proposal is presented. The second section contains a short report on the *status of art* of the antiprotons polarization, with particular emphasis on the polarization mechanism connected with the *filtering method*.

Chapter 2 describes in detail the facilities available in Spinlab laboratory of Università di Ferrara. They consist in two different Atomic Beam Sources, a beam diagnostic system, a calibrated gas supply system and a data acquisition system.

Chapter 3 discusses the *rest-gas* attenuation studies and the extraction of the cross sections for the molecular-molecular and atomic-molecular interactions for hydrogen and deuterium.

In Chapters 4 and 5 the effects of low conductance injection tube and of the *trumpet* nozzle are treated.

The acceptance of focusing magnetic system for ABS is addressed in Appendix A. Appendix B contains a detailed treatment of the Beer's law for the extraction of the attenuation coefficients. Appendix C contains an example of Monte-Carlo input file and the code necessary to use the MC simulation program "DS2G", together with a ray tracking program. Finally Appendix D reports the Time Of Flight measurement procedure, and contains the listing of all the used codes.

Chapter 1

Spin-physics and polarized antiprotons

1.1 The spin of the proton

Mass, charge and spin are fundamental properties of particles and their origin is subject of intense studies. The experiments in this field of physics were started by Rutherford in 1911, with his studies on the internal constituents of atoms [8]. He explored the electromagnetic structure of the atom by analyzing α particles scattered off a gold foil. The angular distribution of scattered particles, in fact, can give information on the inner structure of target atoms. The observation of big deflection angles (even 180°) induced the conclusion that inside atoms there was a hard core (nucleus) where the positive charge was concentrated.

This led, in 1913, to the formulation of the *Bohr Model*, in which the atom is depicted as a small positively charged nucleus, surrounded by electrons that travel in circular orbits around it, with electrostatic forces providing attraction.

Then experiments went further, focusing on the investigation of even smaller dimensions: the structure and composition of sub-atomic particles that constitutes the nucleus (protons p and neutrons n).

By studying the deviations from Coulomb scattering of α particles, Rutherford had already found an approximation for the nuclear radius: about 10^5 times smaller than an atomic radius, but the exact size of nucleons was still unknown.

The hint that also nucleons should have a finite size and an inner structure came in 1933 from the experiments by Frisch and Stern[9][10]: the measured magnetic moment of proton was larger (more than double) than the value predicted by Dirac's theory, thus incompatible with a point-like particle. In fact the gyro-magnetic ratio g ($\vec{\mu} = eg\vec{S}/2m$) predicted by Dirac model is 2 for p and 0 for n , while the measured value was 5.58 for proton and -3.82 for neutron.

To investigate in more detail the nucleon configuration, the key is to reach smaller scales, by increasing the beam energy; in fact the higher the energy of the probe is, the smaller the size it can access.

In the 1950s Hofstadter, using intense and energetic beams of electrons, investigated the

electro-magnetic structure of the nucleons by studying elastic scattering reactions.

$$e^- + p \rightarrow e^- + p \quad (1.1)$$

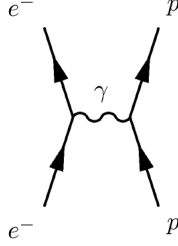


Figure 1.1: Elastic Scattering.

In the hypothesis of one gamma exchange, the cross section of reaction eq. 1.1 (described by the Feynman diagram of fig. 1.1) is given by eq. 1.2:

$$\left(\frac{d\sigma}{d\Omega}\right)_{meas} = \left(\frac{d\sigma}{d\Omega}\right)_{Mott} |F(q)|^2 \quad (1.2)$$

where $\left(\frac{d\sigma}{d\Omega}\right)_{meas}$ is the measured cross section, $\left(\frac{d\sigma}{d\Omega}\right)_{Mott}$ is the Mott formula for the cross section (point-like, spin-less target), q is the four-momentum transferred in the interaction and $|F(q)|^2$ are the electro-magnetic form factors of p . Form factors parameterize the difference between scattering from a point-like target and the measured data, and can be derived from the measured differential elastic cross sections. The experiments were performed at Stanford Linear Accelerator Center (SLAC), where an electron beam (accelerated by a linac) was scattered off a liquid hydrogen or deuterium target.

For the results [11][12] published in 1955-56, Hofstadter was awarded the Nobel Prize in Physics in 1961.

Studies continued in that direction, increasing further the electron beam energy and so switching from elastic scattering to Deep Inelastic Scattering (DIS), in which the energy is so high that the reaction products are different from the colliding particles, which can break into their constituents; new particles can be created from the energy in excess. When passing from elastic scattering to DIS (fig. 1.2a), Structure Functions (SF) have to

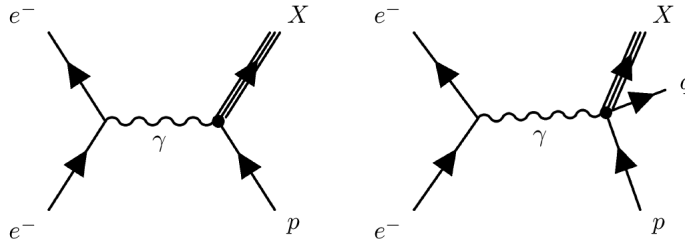


Figure 1.2: (a) Deep Inelastic Scattering, (b) Semi Inclusive Deep Inelastic Scattering.

be introduced; the excitation energy of the proton adds a second degree of freedom, so SF are functions of two independent parameters.

The first DIS experiments (1969)[13][14] revealed different results from the previous elastic scattering experiments: the proton was not as supposed (a fuzzy ball of positive electric charge), but rather had an internal structure, made of hard scattering centers, that could explain the large deflection angles observed.

These experiments showed that proton is made of much smaller particles, in a similar way as Rutherford found that atoms instead of being structure-less as initially supposed, are made of smaller particles.

Feynman in 1969 introduced the *parton model*[15], in which protons are composed of an infinite number of point-like *partons* (later matched to *quarks* and *gluons*) and are considered in the *infinite-momentum frame* so, in DIS case, they have a very high energy. For this reason the following approximations can be introduced: the transverse momentum of the parton can be neglected (since it is small, it is possible to consider only the longitudinal momentum) and its mass can be approximated to zero.

In this model, at high energy, interactions are described as occurring between the incident lepton and the point-like *partons*, considered as quasi-free constituents of the nucleon (fig. 1.2b). As a result the total cross section for the nucleon is obtained by the sum of the individual partons cross sections contributions. The point-like internal constituents of nucleons were identified as *quarks*, that had already been theoretically foreseen in 1964 by Gellmann[16].

These results opened the way to the development of a new theory of hadrons called Quantum Chromodynamics (QCD), that now is a part of the Standard Model. The resulting model for the structure of nucleons is the following: proton is composed of 3 quarks, two up quarks (*u*) with electric charge $+2/3$ and one down quark (*d*) with electric charge $-1/3$; in this way the net electric charge is $+1$ (in units of e). Neutron is composed of 3 quarks: one up quark (*u*) with electric charge $+2/3$ and two down quarks (*d*) with electric charge $-1/3$; in this way the net electric charge is 0. Quarks are bind together by massless and chargeless exchange bosons, called gluons.

In 1980s, the EMC (European Muon Collaboration) experiments at CERN, revealed that only a small fraction of the nucleon total spin is carried by the quarks and thus opened the so called “spin-crisis”[17][18]. The result was subsequently confirmed by SLAC and the spin entered in the new scenario as the tool to understand the nucleons structure.

The three already known quarks were called *valence quarks*, and the hypothesis of the existence of the *sea quarks* (couples of $q\bar{q}$) and *sea gluons* was made. The single constituents’ spins, their corresponding angular motion and binding bosons (*gluons*) are now considered possible sources of the total nucleon spin, according the formula:

$$S_z^N = \frac{1}{2} = \Delta q + \Delta G + \Delta L_z^q + \Delta L_z^g \quad (1.3)$$

where S_z^N is the z component of nucleon spin, Δq and ΔG are the contributions from quarks and gluons spins, ΔL_z^q and ΔL_z^g are the contribution from quarks and gluons angular momenta.

The importance of dedicated experiments to measure these quantities is evident. At present the theoretical models are based on the fact that, at leading-twist order, the quark structure of hadrons is completely described only by three structure functions. These functions are the quark momentum distribution $F_1(x, Q^2)$, the *helicity* distribution $g_1(x, Q^2)$ and *transversity* distribution $h_1^q(x, Q^2)$.

Quark momentum distribution $F_1(x, Q^2)$ describes the number of quarks (or antiquarks)

of designated flavor that carry a momentum fraction between x and $x + dx$ of the proton's momentum, in the infinite-momentum frame.

Helicity distribution $g_1(x, Q^2)$ describes the difference between the probability to find a quark (with momentum fraction x) with spin aligned and spin anti-aligned to the spin of the longitudinally polarized nucleon ($Prob(\uparrow\uparrow) - Prob(\uparrow\downarrow)$).

Transversity h_1 describes the difference between the probability to find a parton (with momentum fraction x) with spin aligned and spin anti-aligned to the spin of the transversely polarized nucleon ($Prob(\uparrow\uparrow) - Prob(\uparrow\downarrow)$).

Using Deep Inelastic Scattering, experimental and theoretical studies led to improved knowledge of $F_1(x, Q^2)$ and $g_1(x, Q^2)$; in order to complete the description of the partonic structure of the nucleon, today one piece is still missing: *transversity*.

Up to now, little is known about transversity because it is the most difficult SF to measure, since it is a *chiral-odd* function. For this reason it is not possible to measure transversity in DIS experiments.

Electroweak and strong interactions conserve chirality, so in DIS events, h_1 cannot occur alone, but has to be combined to a second chiral-odd quantity.

Thus it is necessary to use one of the following reactions: Semi-Inclusive Deep Inelastic Scattering (SIDIS) (h_1 coupled to a chiral-odd fragmentation function called Collins function); transverse Single Spin Asymmetries (SSA) in inclusive processes like $p^\uparrow p \rightarrow \pi X$ (h_1 coupled to Collins function); polarized Drell-Yan processes (product of two transversity distributions).

Recently Anselmino and collaborators have extracted h_1 with a simultaneous analysis of DIS experiments (HERMES and COMPASS) and the annihilation experiment BELLE [19]. The value obtained for h_1 was found to be rather small respect the calculations of the quark models. This opened very interesting speculations and made more urgent the direct measurement of the transversity with the Drell-Yan events produced in the annihilation of protons and antiprotons, both polarized:

$$p^\uparrow + \bar{p}^\uparrow \rightarrow e^+ + e^- + X \quad (1.4)$$

Measuring the double transverse spin asymmetry A_{TT} , a direct measurement of transversity can be obtained. It should be noted that it is necessary to use \bar{p} beam, because a proton beam (available for example at RHIC) would give a much lower useful event-rate; in fact the proton beam would probe the sea quarks, instead of the valence quarks, therefore leading to a much lower cross section.

1.2 Polarized antiprotons

The most challenging part of the PAX program is to find a way to produce an intense circulating stored beam of polarized antiprotons. In fact, such a tool is still not existing, despite the efforts lasted many years (see [20]).

For instance it is interesting to remind that, in 1985, O. Chamberlain and A. Krish organized a workshop at Bodega Bay (CA, USA)[21], with the aim to provide a deep discussion on all the ideas proposed to polarize antiprotons. Prof A. Krish, in his review talk, listed twelve ideas.

1. Polarized antiprotons from in flight decay of antihyperons.
2. Spin filtering of antiprotons by a polarized hydrogen target.
3. Stochastic technique (see stochastic cooling).
4. DNP in flight using polarized electrons and microwave radiation.
5. Spin-Flip from synchrotron radiation induced by X-ray laser.
6. Spontaneous Spin-Flip from synchrotron radiation.
7. Polarization by scattering.
8. Repeated Stern-Gerlach deflections.
9. Polarized antiprotons via the formation of anti-hydrogen, and the application of ABS method.
10. Polarization during storage in a penning trap.
11. Polarization by channeling.
12. Polarization through interaction with polarized X-rays from a diamond crystal.

Several of this ideas survived the workshop for a significant period of time. In particular idea (1) has been successfully applied at FNAL, by the E704 Collaboration [22], leading to secondary 500 GeV/c beams of protons and antiprotons. However, no accumulation and storage have ever been tried.

Idea (2), the spin filtering of stored beams, was rated as practical and promising. In fact in 2007 Daresbury Workshop[23] emerged that the only method survived, among the ones proposed in the Bodega workshop, was the spin filtering. It is interesting to observe that this idea is certainly not new. There were a number of examples of production of polarized nucleons via interactions with polarized targets. In 1966 Shapiro[24] showed that, due to strong spin dependence in the (n,p) cross section, polarized neutrons could be produced by means of spin-selective attenuation in a solid polarized proton target. In 1970 a test[25] successfully used an underground nuclear explosion in conjunction with a solid polarized target as a polarized neutron source. This was one of the first experimental demonstrations of the spin filtering. Today the most effective way to polarize beams of thermal neutrons is spin filtering by a high pressure polarized ^3He gas target[26], resulting in high transmission and polarization.

P.L. Csonka, in 1968, proposed[27] to polarize the ISR 30 GeV/c protons at CERN using

strong interactions of the proton beam with the protons of a polarized gas hydrogen target installed on the ring. Meanwhile, polarized beams of stable ions were generated by a polarized ion source, followed by acceleration. The suggestion [27] has never been tested at high energies.

After the discovery of antiprotons, in 1955 by Chamberlain, Segre and others, their interactions with nuclei was studied using secondary beams at various Laboratories (BNL, CERN, FNAL, KEK, Serpukov).

In the early 1980s the CERN antiproton source project allowed for the first time the storage of antiprotons in collector and experimental storage rings like the Antiproton Accumulator (AA) and the Super Proton Synchrotron (SPS) collider.

In 1982 Kilian and Moehl proposed spin filtering of antiprotons in the Low-Energy Antiproton cooler Ring LEAR[28]. In 1984 Povh, Steffens and Walcher worked out a realistic proposal for LEAR, including a feasibility test with protons at the Heidelberg Test Storage Ring (TSR). The proposal was presented[29] at the third LEAR workshop in January 1985.

The feasibility test has been actually done in the early 1990s, and it has proven to work with protons in the FILTEX experiment[30] at TSR, Heidelberg; in fact, after about 90 minutes, a polarization of about 2% was measured.

In the 2007 Daresbury Workshop the attention of the experts in this field has been focused on the processes involved in the polarization buildup through filtering.

Csonka[27] has suggested to use strong interactions to polarize proton beams using a polarized hydrogen gas target, installed on the proton storage ring. Based on this idea, calculations on the TSR filtering experiment results have been done, using the pp scattering data (see [31]). The puzzling difference among the measured polarization build-up rate and the theoretical one, presented in [30] and revised in [32], is exhaustively discussed in [33]. The measured polarization build-up rate resulted less of the foreseen one. This fact has induced the formulation of a model[34][35] based on three different contributions: spin-transfer of polarized electrons to stored proton beam (electro-magnetic), scattering of target (polarized) protons in the ring acceptance, and hadronic (strong) interactions of proton beam with target proton. This led to quantitative agreement to the data and was, for nearly 20 years, accepted as the explanation for the FILTEX results.

It is worthwhile to notice that in [34] the contribution of the polarized electrons of the target to the antiproton polarization building-up was considered important and it has induced many controversial speculations on the possibility to use either an electron polarized hydrogen target, or an electron beam to induce the antiproton polarization. Various theoretical approaches to the problem have been published (see [36] for the references).

From the other hand, in their papers, the authors [34] and [35] emphasize for the first time the importance of the interference of the Coulomb amplitude and the spin-dependent part of the hadronic amplitude. Under the FILTEX condition, this effect diminishes the corresponding cross-section more than 40%. This has been confirmed recently by [37] and [38] and leads, with a revision of the analysis of the FILTEX experiment, to an essential agreement among theory and experiment.

In 2004 the PAX Collaboration has proposed to use spin filtering to polarize the antiprotons of the FAIR facility at Darmstadt. In this frame, an experimental program to test the electro-magnetic contribution to the polarization build-up has been carried out at COSY (Cooler Synchrotron - Forschungszentrum Julich). In order to experimentally test the possible electro-magnetic contribution from electrons/positrons, as proposed by

T. Walcher[39], and determine the spin-exchange cross section, a dedicated study has been set up at COSY[40] in February 2008. It consisted in trying to depolarize an initially polarized proton beam, by interaction with unpolarized co-moving electrons (from a detuned electron-cooler). The (de)polarizing cross section (at small relative velocity) calculated by Walcher for electrons is huge: $2 \cdot 10^{13}$ barn, so even if the target density of electron cooler is much smaller ($1 \cdot 10^8$ cm^{-2}) compared to gaseous targets ($1 \cdot 10^{14}$ cm^{-2}), the polarizing effect should have been clearly visible[40]. During this test no effect has been observed [41].

It seems therefore experimentally demonstrated that the electro-magnetic interaction does not change the beam polarization. From this result, the only contribution that remains is the nuclear interaction, as [27] suggested.

At COSY the FILTEX experiment will be reproduced, in slightly different conditions. With this experiment, that is in preparation and will be ready at the end of 2009, the PAX collaboration will confirm the FILTEX results for protons, with a setup that can be used without modifications on AD (Antiproton Decelerator) ring, at CERN, where the spin filtering with antiprotons will be finally tested for the first time. See on this item [42].

Chapter 2

The SpinLab facility in Ferrara

The facilities available in the “SpinLab” laboratory of Ferrara consist of two Atomic Beam Sources (ABS), the unpolarized ABS1 and the polarized ABS2, a diagnostic system equipped with a Quadrupole Mass Analyzer (QMA), a *chopper* and a Time Of Flight (TOF) measurement device, a calibrated gas injection system, an optical spectrometer (see detailed description in [43]), and a data acquisition system (DAQ).

2.1 Unpolarized Atomic Beam Source (ABS1)

The apparatus called ABS1 (see fig.2.1) is an unpolarized Atomic Beam Source, that was originally part of the Jet Polarized Target (JPT) laboratory at CERN.

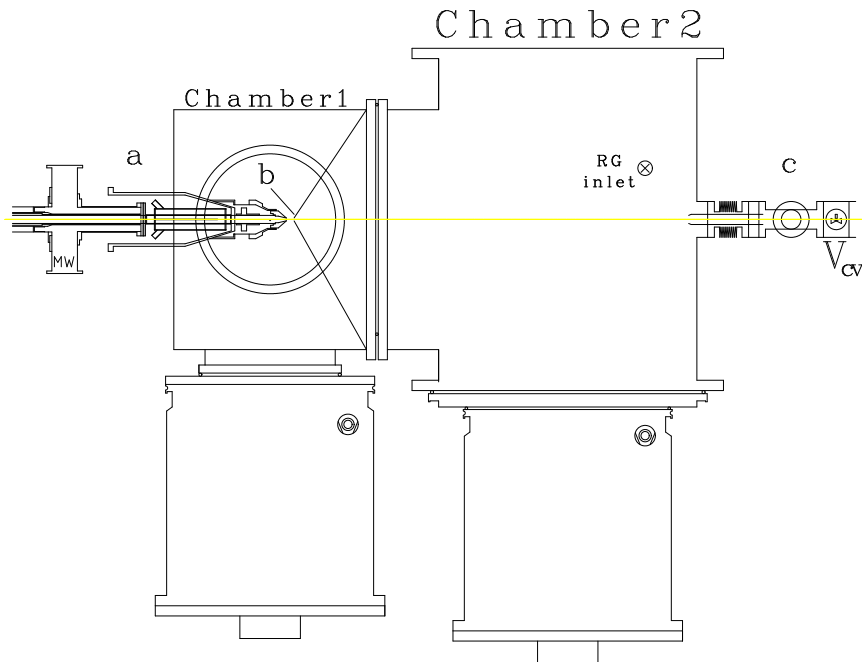


Figure 2.1: Atomic Beam Source “ABS1” scheme. (a) dissociator, (b) skimmer, (c) Compression Volume, (RG inlet) Rest Gas inlet.

It is composed of a dissociator and two vacuum chambers connected by a small aperture

(skimmer) in order to obtain a collimated beam, directed as the system axis. Furthermore, in this way, a differential pumping system is obtained.

2.1.1 Dissociator

The dissociator is schematically shown in fig. 2.2.

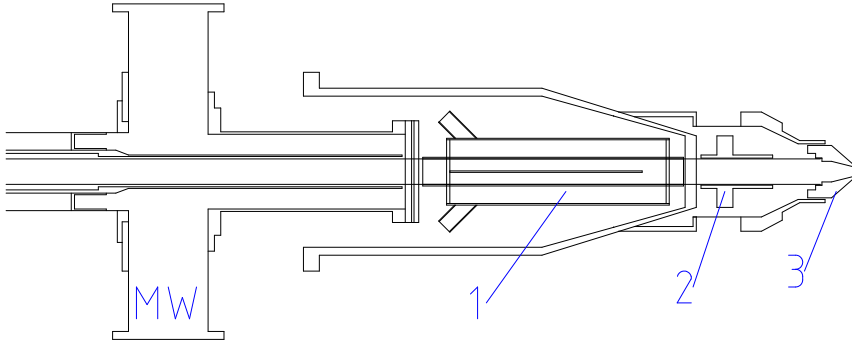


Figure 2.2: ABS1 dissociator. (MW) Microwave cavity, (1) Water cooling, (2) Collar, (3) Nozzle.

Its design is based on a waveguide surfatron plasma source (Moisan scheme[44]). A flux of hydrogen/deuterium, precisely controlled by a flow controller, passes through a “NHI-100” quartz tube of inner(outer) diameter 13(15) mm and length 85 cm. Before installation the tube is immersed, for cleaning, in a 2:5 mixture of $HF:H_2O$ for 5 minutes, washed in pure water, 10 minutes in 2:1 mixture of $HCl:H_2O$ and washed again in pure water. Inside the tube, molecules are dissociated into atoms by microwaves operating at 2.45 GHz and 600 – 800 W power. The standard operating pressure of the dissociator is of the order of ≈ 1 mbar and is measured by a baratron (Pfeiffer CMR 263, 10 mbar FS).

After dissociation, the atomic gas is cooled by a series of stages of decreasing temperature as shown in fig. 2.2: (1) a water jacket ($-20^\circ \div 10^\circ C$), (2) a copper collar ($70 \div 200 K$) around the quartz tube and finally (3) an aluminum nozzle ($70 \div 290 K$). A good thermal contact for the water jacket, which is not under vacuum, is obtained with thermal grease, the one of the collar (inside vacuum) instead is obtained with indium foil pressed between the quartz tube and the collar itself.

The temperatures are stabilized by three dedicated electronic heaters. The setpoint of each of the stages can be varied separately inside its range. Various nozzles can be mounted, for testing purposes. The nozzles used in this thesis are three. They are all made of “anticorodal” aluminum and cleaned with ethanol. Their geometry is shown in fig. 2.3.

2.1.2 Vacuum chambers

Chamber 1 is pumped by a 3500 l/s (Leybold NT 3500) and a 2200 l/s (Pfeiffer TPH 200) turbomolecular pumps; its pressure is measured by a cold cathode gauge (Pfeiffer PKR261). The two turbomolecular pumps are connected to the prevacuum pump (Pfeiffer DUO 65, 65 m³/h) through a root pump (Leybold WS2000, 1750 m³/h) that improves the pumping speed of the system during normal operation with high gas load (≈ 120 sccm).

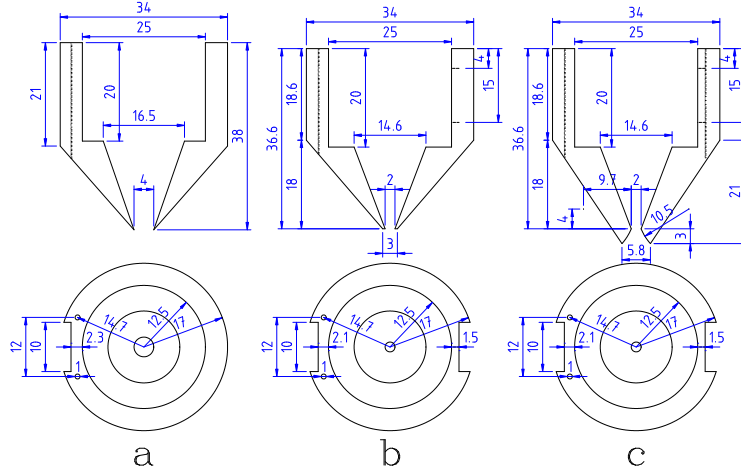


Figure 2.3: Available Nozzles: (a) sonic 4 mm, (b) sonic 2 mm, (c) trumpet 2 mm.

Between Chamber 1 and 2 a skimmer is mounted, selecting the central part of the beam. In this region the particles have a velocity almost aligned with the beam axis (yellow dashed line of fig. 2.1). At the same time such a diaphragm provides also a differential pumping system between the two chambers.

The available skimmers are presently two: 6 mm diameter and 2 mm diameter (see fig. 2.4).

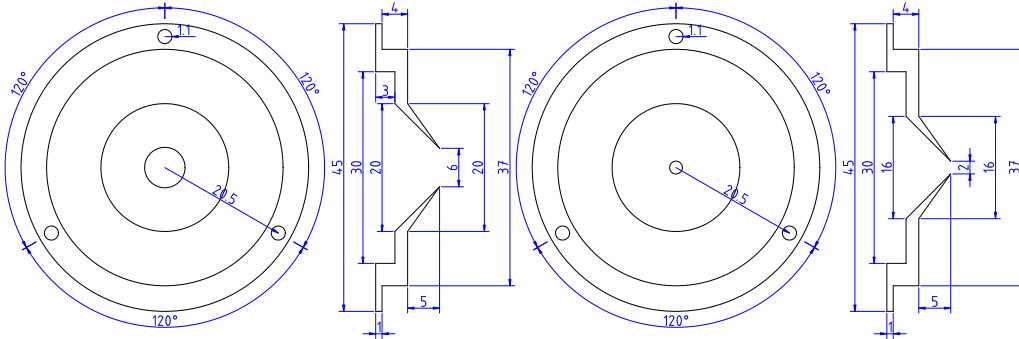


Figure 2.4: Skimmers: 6 mm diameter (left) and 2 mm diameter (right).

Chamber 2 is pumped by a 3500 l/s (Leybold NT 3500) and a 2200 l/s (Pfeiffer TPH 200) turbomolecular pumps; its pressure is measured by a full-range cold-cathode gauge (Pfeiffer PKR251) and a full-range hot-cathode gauge (Pfeiffer PBR260). The gas load on this chamber is only about 5 scm ; since it is much smaller than the previous one, the root pump is a Leybold WS 250 (210 m^3/h) and the prevacuum pump is an Alcatel mod. pascal 2021 (21 m^3/h).

The base pressure (no beam) in Chamber 1 and 2 is about $4 \cdot 10^{-8} mbar$ and $2 \cdot 10^{-8} mbar$ respectively. During normal operation (125 scm , H_2 beam, 50% of flow controller full scale) the pressure is $3 \cdot 10^{-4} mbar$ in chamber one and about $2 \cdot 10^{-5} mbar$ in chamber two. Almost all the hydrogen flow goes to the first two chambers: 95% is pumped through Chamber 1, 5% through Chamber 2 and only a very small fraction (0.005%) of the initial flux reaches the diagnostic system.

Chamber 2 is equipped with a “rest gas inlet”, connected to a MKS flow controller, that allows to uniformly increase its pressure, by injecting a calibrated hydrogen or deuterium flux.

The inlet is composed of a MKS flow controller (mod. “20sccm/H2”) connected to a stainless steel tube of inner diameter 4 mm properly shaped¹ in order to produce an homogeneous increase of the scattering chamber pressure. The increase in Chamber 2 pressure, obtained with this inlet, is used for the Rest Gas Attenuation measurements (see chapter 3) and to calibrate *HV2*, *HV2b*, *CV* and *CV2* gauges. After traversing Chamber 2 the beam enters the diagnostic system, described in the next paragraph.

2.2 Diagnostic system

The diagnostic system is composed of a Compression Volume (CV) and two vacuum chambers (Chamber 3 and 4) equipped with a Quadrupole Mass Analyzer, as shown in fig. 2.5.

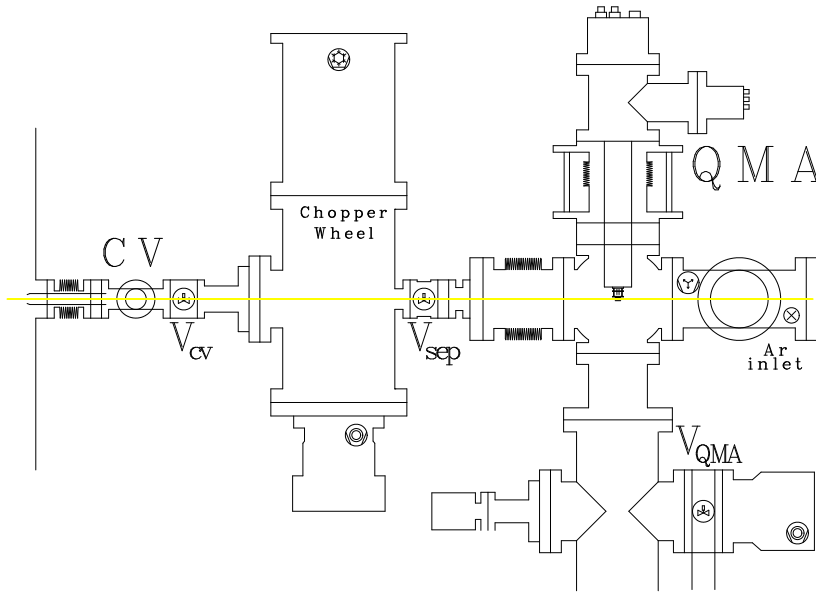


Figure 2.5: Diagnostic system composed of Compression Volume (CV), Chamber 3 (CW chamber) and Chamber 4 (QMA chamber).

The Compression Volume consists in a cylindrical aluminum tube called *compression tube* (see fig. 2.6), connected to a small volume (see fig. 2.5 and fig. 2.7) that is closed by a Full-metal VAT valve called V_{CV} . Beam passes through the compression tube and enters this small volume, causing an increase in its pressure (ΔP_{CV}), detected by a full-range ion gauge (Pfeiffer PBR260) that is proportional to the beam intensity I (see also chapter 4):

$$I = \frac{1}{k_B T} Q = \frac{1}{k_B T} \Delta P_{CV} C_{CT} \quad (2.1)$$

¹The exit part of the tube points towards the inner surface of the vacuum chamber: in this way the molecules motion is randomized and the gas density in the vacuum chamber can be considered homogeneous.

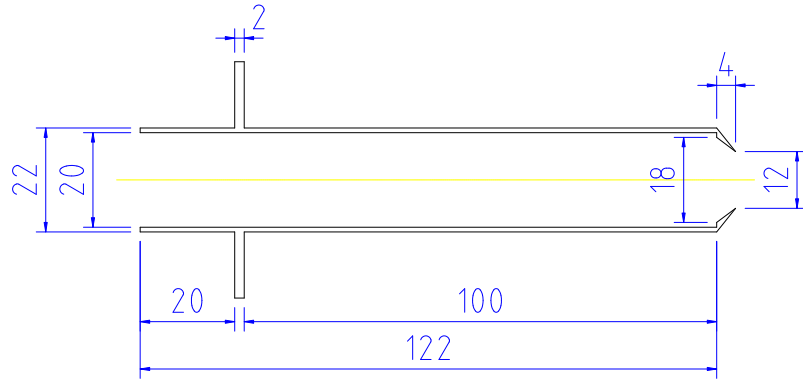


Figure 2.6: ABS1 compression tube geometry. Its conductance is equivalent to a cylindrical tube of 10 cm length and 1 cm diameter.

where C_{CT} is the conductance of the compression tube. In front of the CV a *flag* is mounted (metallic plate, connected to a vacuum rotary manipulator) that can block the beam entering the compression volume with the aim of evaluating the background of Chamber 2 in the CV measurements.

The compression volume is also connected to the calibrated gas injection system presented in fig. 2.7.

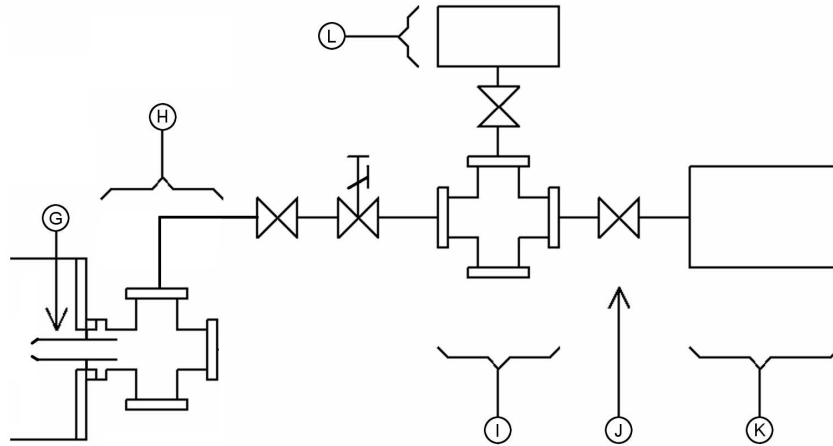


Figure 2.7: Calibrated gas injection system connected to the Compression Volume (H): (G) compression tube, (I) constant pressure volume (V_{cal}), (J) Regulating Valve, (K) Hydrogen gas buffer, (L) calibrated volume.

The calibrated system is composed of a volume (V_{cal}), in which the pressure is kept constant by a regulating valve, driven by a PID controller that reads actual pressure from one of the two available capacitive gauges (Pfeiffer CMR261 and CMR271). This volume is connected to the CV through an adjustable leak valve and a bellow. The flux supplied by the system depends therefore on the V_{cal} pressure and opening of the leak valve. This system is movable and can be connected to ABS1 CV, ABS1 Chamber 4 or ABS2 CV.

When V_{CV} is open, the beam passes through and reaches Chamber 3. Chamber 3,

called Chopper/Wheel (CW) chamber, is equipped with two different aluminum disks (see fig. 2.8): a vacuum manipulator can select which of the two to put on beam axis: *chopper* or *wheel*. It is also possible to take out both disks and let the beam pass through unaffected.

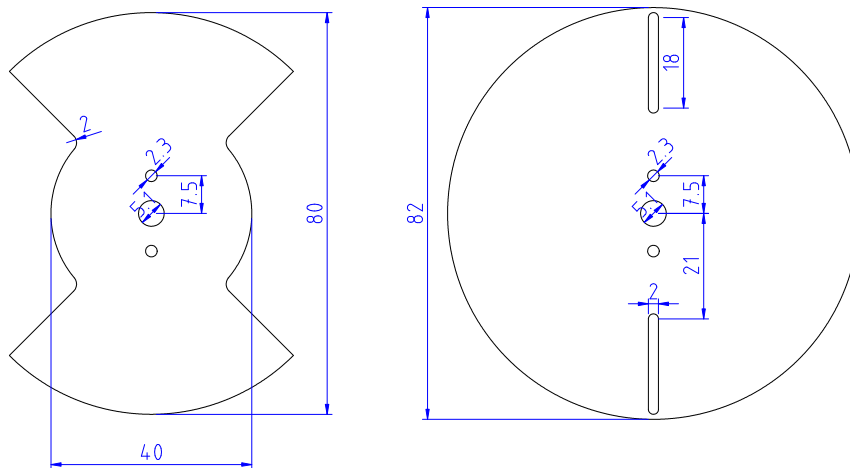


Figure 2.8: Chopper (left) and Wheel (right) geometries.

This chamber is pumped by a 500 l/s (Pfeiffer TMU521P) turbomolecular pump and a 1500 l/s (Edwards Coolstar 1500) cryogenic pump. The pressure of Chamber 3 is about $3 \cdot 10^{-8} mbar$ both with and without beam; its pressure is measured by a full-range ion gauge (Pfeiffer PBR 260).

Chopper

The chopper is used for degree of dissociation (α) and beam density measurements. It has two big apertures: the beam is chopped at 50% duty-cycle (the open time is equal to the close time).

In fig. 2.9 an example of chopped beam signal and trigger is presented on a digital oscilloscope, while fig. 2.10 shows the acquired waveform obtained with Labview, averaged over 40 single spectra. The rotation speed of the *Chopper* is kept constant at 16.5 Hz by a feedback micro-controller circuit (see next section 2.2.1) that drives its DC brushed motor.

Wheel

The *Wheel* is used for Time Of Flight (TOF) measurements. Section 2.2.2 and Appendix D describe in detail the TOF technique and how it is used to extract beam velocity distribution. *Wheel* has two narrow slits (2×20 mm) that let only a small fraction of the beam pass through. The small slits aperture and its rotational speed (150 Hz, stabilized by a brush-less motor control board), were chosen to approximate its opening function as a delta function. For calibration purposes the speed of the *wheel* can be varied between 6 and 175 Hz.

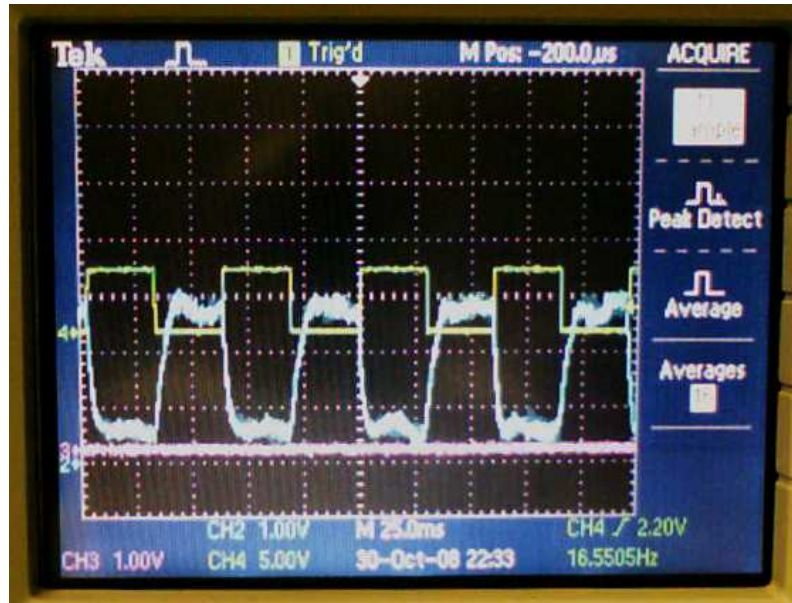


Figure 2.9: Chopper signal directly seen on a digital oscilloscope. Single spectrum (no average).

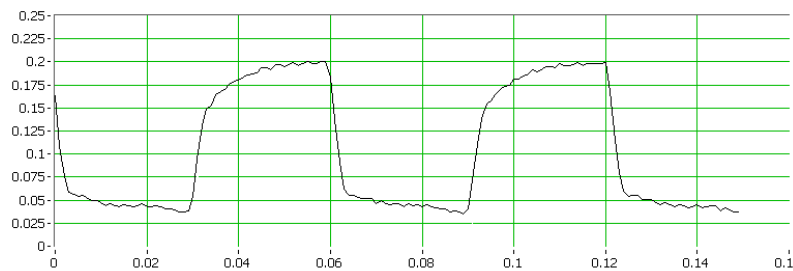


Figure 2.10: Chopper signal (average of 40 spectra) obtained with Labview dedicated program.

Finally the chopped beam reaches the Quadrupole Mass Analyzer (QMA) in the last chamber: Chamber 4.

Between Chamber 3 and 4 a 4 mm diameter collimator is mounted, in order to obtain a differential pumping system and to avoid that the outer part of the beam hits the ionization volume or the ion optics of the QMA.

Chamber 4 is pumped by a 300 l/s (Varian TV300HT) turbomolecular pump, a 100 l/s (Varian Diode) ionic pump and a titanium-sublimation (Ti-Ball) pump cooled by water at about 13°C. The base pressure of Chamber 4 is $< 5 \cdot 10^{-10}$ mbar, while during normal operation is about $2 \cdot 10^{-9}$ mbar.

Chamber 4 is also equipped with a gas inlet that can be connected to the calibrated gas injection system in order to maintain a constant and selectable pressure in the chamber; in this way various calibrations of the QMA can be carried out.

Quadrupole Mass Analyzer

The instrument installed is a Cross-Beam Quadrupole Mass Analyzer (see fig. 2.11), which detects the “particle number density” n (particles per unit of volume, $[m^{-3}]$). When par-

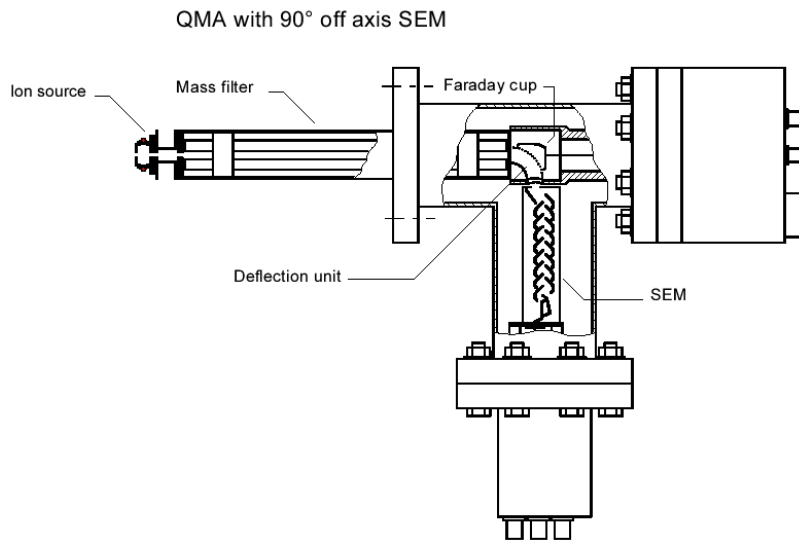


Figure 2.11: Quadrupole Mass Analyzer scheme (model Pfeiffer QMA-410).

ticles (atoms/molecules) enter the “ionization volume” they are ionized by impact from electrons that are thermally emitted by a hot tungsten filament and focused by electrical extraction fields. The ions created are extracted from the volume by electric field and focused to the mass-filter, which provides mass selection (m/e), by means of a combination of RF and a constant DC component. Finally they reach one of the two available detection stages: Faraday-cup or Secondary Electron Multiplier (SEM).

Faraday-cup is a metallic collector on which ions can deposit their electric charge. The resulting signal is therefore a positive current proportional to the number of detected ions per second.

If high sensitivity is required, ions can be deflected by the 90° *deflection unit* into the SEM, which is a fast high-gain electron-current amplifier similar to a photo-multiplier. It is composed of a series of 17 Cu-Be dynodes that provide an amplification up to 10^8 ; the measured gain (when the SEM is new) is about 10^4 if a potential of 1470 V is applied between the end dynodes. The drawback of this kind of detector is the aging: during normal working conditions, the amplification process, by multiple electron emission occurring on the surface of the dynodes, causes a degradation of the surface itself and thus diminish the total amplification. The decrease in gain can be compensated by increasing the high voltage supply. When reaching the maximum allowed voltage (in this model is 3.5 KV) the SEM has to be replaced with a new one. The not-fixed gain implies that if an absolute measurement is required, the SEM has to be calibrated with respect to the Faraday-cup. The current-signal from Faraday-cup or SEM is then pre-amplified and converted to a voltage signal by the “electrometer preamplifier” (EP). The resulting voltage signal can be displayed on an oscilloscope or digitalized by an acquisition board (see section 2.4.1, paragraph “Computer *spinlab2*”).

The raw signal from the QMA has a noise component that prevents it from being directly

used for precise measurements. The noise attenuation is accomplished by the standard averaging technique. By synchronizing the acquisition of the QMA signal to the rotation of the chopper or of the wheel, by means of fast optical triggers, it is possible to improve measurement precision: by averaging tens (if chopper is used) or thousands (if wheel is used) single spectra it is possible to greatly reduce the noise and obtain a clean signal. The fast optical trigger consists in a LED (light emitting diode) mounted on a ‘U’ shaped support, facing a photo-transistor connected to an integrated pre-amplifier: when the chopper or wheel blocks the light path from the LED to the photo-transistor the device provides a TTL output trigger.

2.2.1 Motor speed stabilization circuit

The motor speed stabilization circuit is a custom device that can keep constant the rotation speed of the chopper motor. In this way the chopped beam signal can be easily averaged and the resulting waveform presents low noise.

It is based on a programmable micro-controller produced by Microchip (PIC16F88). A custom program is burned on its flash memory and the device adjusts the motor voltage in order to keep the rotation speed constant. It has been developed in C language, compiled with `sdcc`[45] and burned on the PIC with `picprog`[46], using PIC-programmer 2 hardware[47].

The working principle is the following: the micro-controller constantly measures the time between two rising trigger edges and adjusts the voltage that drives the motor in order to keep its rotation speed constant.

Since this micro-controller has no internal DAC (Digital to Analog Converter), to obtain an analog output to drive the motor, use has been made of the built-in PWM (Pulse Width Modulation) module.

The square wave produced by the PWM module is fed to a low-pass RC-filter: the resulting DC is proportional to the duty-cycle of the square wave. In this way a DC output is produced, that can be varied from 0 to 4 V. The scheme of the electronic circuit is shown in fig. 2.12, while the external connections are presented in fig. 2.13

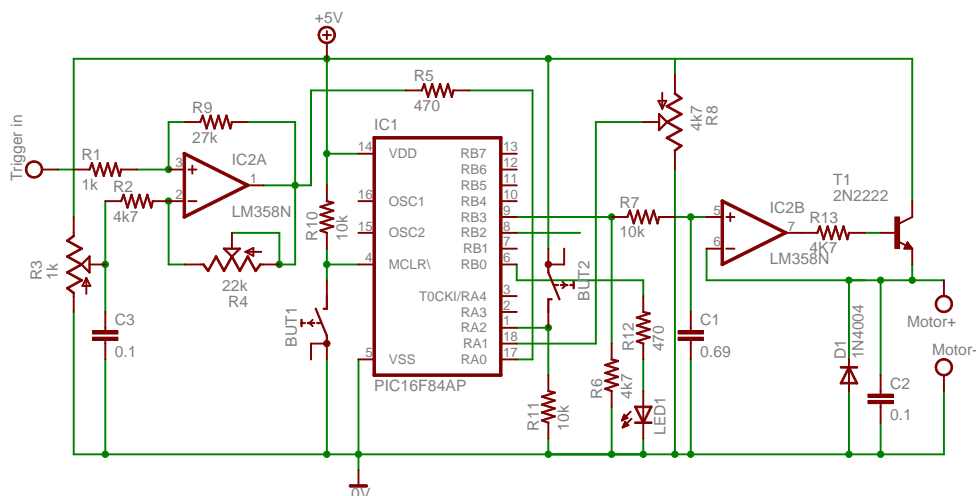


Figure 2.12: Scheme of the regulating electronic circuit.

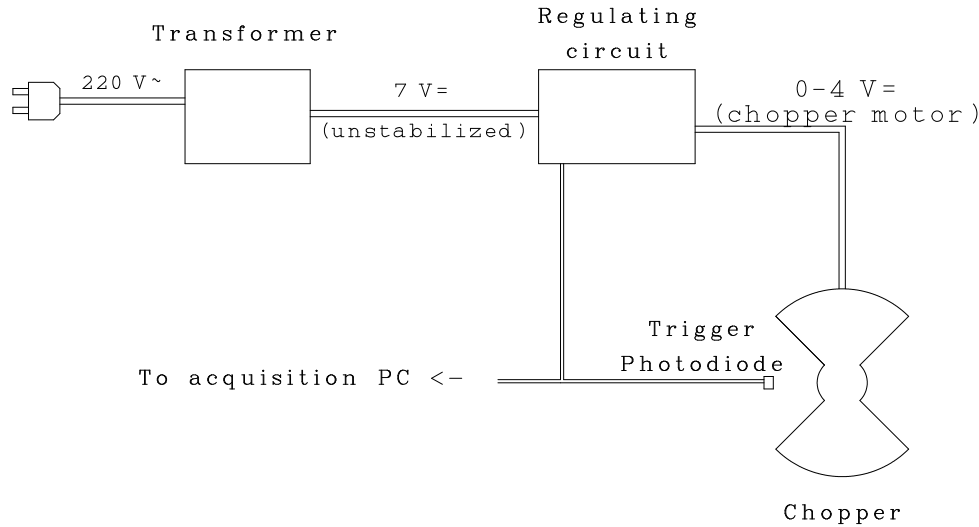


Figure 2.13: Scheme of electrical connections of the regulating circuit.

With a push-button on the front panel one of the following four algorithm can be selected (the number of initial slow blinks of the green LED corresponds to the selected function):

- f1. Keep rotation speed constant, stabilizing the trigger at 16.5 Hz.
- f2. Debug 1 (used to tune the PID parameters).
- f3. Debug 2 (used to tune the PID parameters).
- f4. Identical to 1, but with setpoint frequency selectable from 12.9 to 22.2 Hz by the knob on the front panel.
- f5. No automatic stabilization: fixed Duty-cycle of PWM, according to position of the front knob. Output voltage is adjustable from 0 to 4 V.

In functions f4 and f5, the position of the knob is continuously read by the micro-controller, so it is immediately sensitive to a change of its setting.

The green LED on the front panel stays on during the measuring time (between two subsequent rising triggers in f1 f2 f3 ed f4), blinks fast in f5. If the LED stays off it means that no trigger is received.

The algorithm implemented in the control software is a simplified version of a standard PID (Proportional, Integrative, Derivative). In this way a fast reaction to motor rotation instabilities is obtained and the circuit is able to keep the chopper rotation stabilized with a precision of less than 0.5%. The improvement in the stability of the rotational speed of the chopper obtained with the implementation of feedback circuit is evident by comparing fig. 2.14 and fig. 2.15 (plots have different vertical scale).

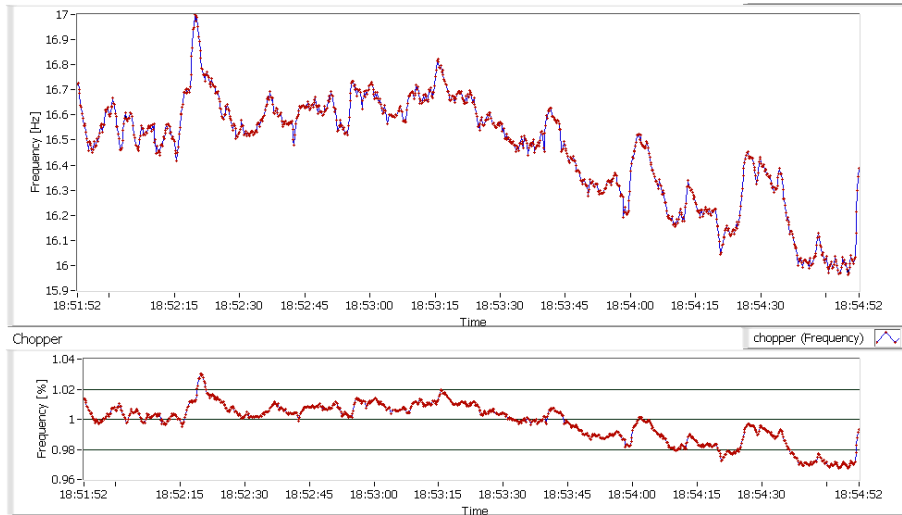


Figure 2.14: Chopper frequency stability check before the implementation of the stabilization circuit. Top panel shows measured frequency f , while bottom panel shows ratio between f and setpoint $f_0 = 16.5 \text{ Hz}$.

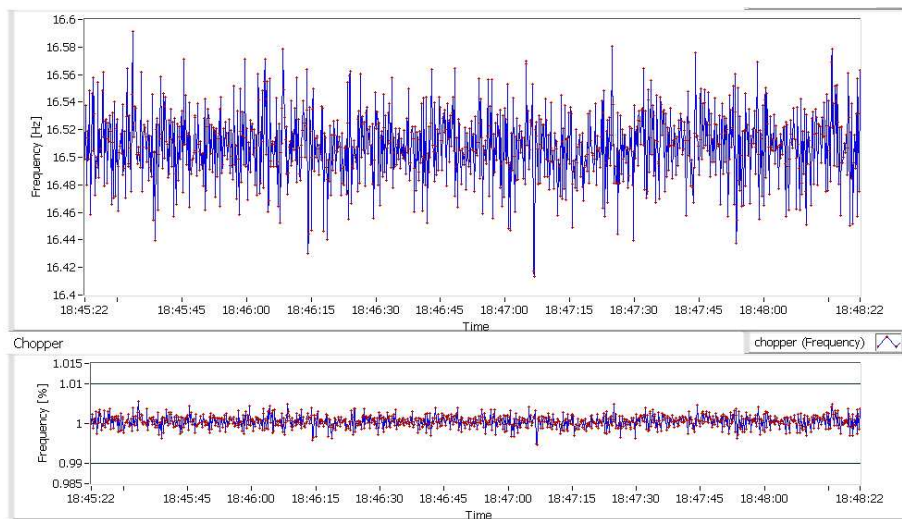


Figure 2.15: Chopper frequency stability check after the implementation of the stabilization circuit. Top panel shows measured frequency f , while bottom panel shows ratio between f and setpoint $f_0 = 16.5 \text{ Hz}$ (vertical scales are different from the previous picture).

2.2.2 Time Of Flight (TOF)

In order to determine the beam velocity distribution, use has been made of the Time Of Flight technique (TOF), that consists in measuring the time required by a particle to travel a precise distance: in our case the distance between the *wheel* and the QMA, that is 51 cm (see fig.2.16).

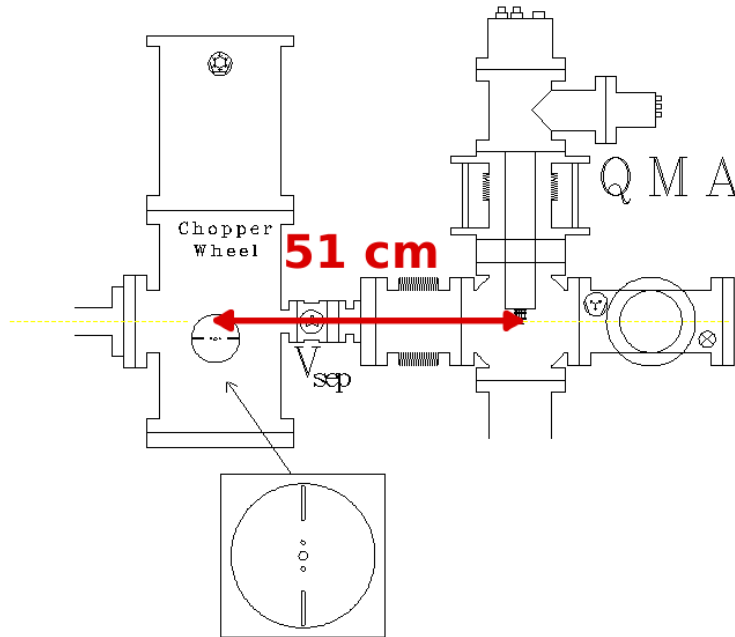


Figure 2.16: Detail of the detection system showing the distance between *wheel* and QMA.

The continuous beam entering the diagnostic system is chopped by a high speed *wheel* that let only very short pulses of particles pass through. A dedicated Labview program measures the time between the start time of the bunch, provided by the optical trigger, and the stop time when the bunch reaches the QMA. The quadrupole mass analyzer signal is acquired by a National Instrument board (see section 2.4.1, paragraph “Computer *spinlab2*”) through a fast pre-amplifier. A basic scheme of this technique is presented in fig. 2.17, where the evolution of the bunch shape during the path to the QMA is also shown. The sliver of beam produced by the narrow slit on the *wheel* becomes wider as it travels to the spectrometer, due to the different velocities of the particles: the faster ones arrive at the QMA before the slower ones.

The amplified signal from QMA is acquired by a dedicated Labview program that averages over thousands of spectra, in order to improve the signal to noise ratio. The result is (in an ideal case) a *time distribution* $F(t)$, from which the *velocity distribution* $f(v)$ can be derived:

$$f(v) \propto t^2 F(t) \quad (2.2)$$

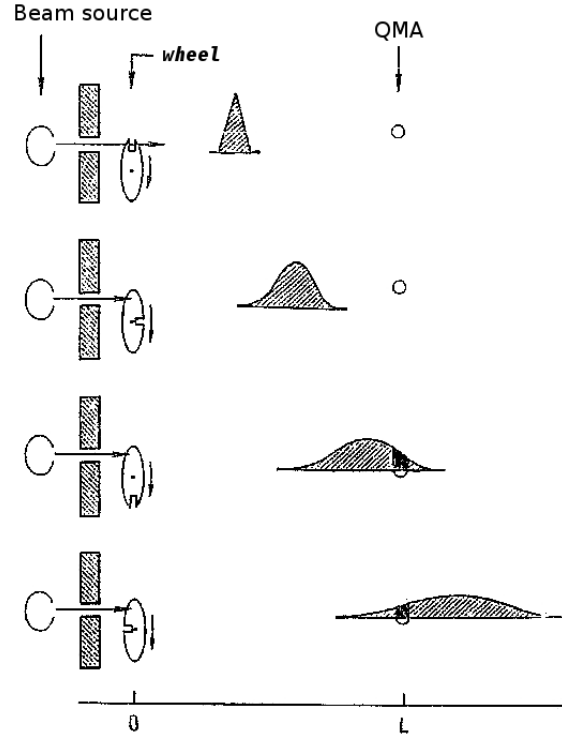


Figure 2.17: Time Of Flight basic scheme. The areas highlighted in grey represent the evolution of the shape of the signal while it travels from the wheel to the detector.

Unfortunately the QMA signal $S(t)$ is not coincident with $F(t)$, but it is rather its convolution with different functions that account for the difference between the real measurement and the ideal conditions:

$$S(t) = \int_0^t K(t) \int_0^\lambda F(\lambda - \psi) A(\psi) d\psi d\lambda \quad (2.3)$$

where:

- $F(t)$ - time (of flight) distribution.
- $A(t) = \sin(\pi t/T)$ - opening function of the *wheel*, where $T=75.3$ ms.
- $K(t) = \frac{1}{\tau_e} e^{-t/\tau_e}$ - time response of electronics.

Furthermore the raw $S_{raw}(t)$ from the QMA has to be corrected for three systematic errors:

- trigger offset: the time between optical trigger and the passing of the beam through the *wheel*; since the optical trigger is on the opposite side of the wheel respect to the beam, geometrical imperfection and errors in alignment can cause time shift between the trigger and the real time when the bunch of particles starts.
- drift time: the time necessary for an ion contained in the QMA ionization volume to travel to the detection dynode, through mass filter, deflector and SEM.

- constant background level, due to the residual gas in QMA chamber.

A test function $f^t(v)$ is calculated from the ideal velocity distribution of gas expansion in vacuum²:

$$f^t(v) \propto v^2 \exp \left[-\frac{m}{2k_b T_b} (v - v_d)^2 \right] \quad (2.4)$$

where T_b is the beam temperature and v_d is the drift velocity. The corresponding $F^t(t)$ is derived and convoluted in order to obtain $S^t(t)$. The resulting curve is compared with the measured data and the starting parameters v_d and T_b are optimized by minimizing the χ^2 between $S(t)$ and $S^t(t)$:

$$\chi^2(C, v_d, T_b) = \Sigma \frac{[CS_t(i) - S(i)]^2}{\delta^2 S(i)} \quad (2.5)$$

where C is a normalization constant (to match the amplitude), $\delta S(i)$ is the error for the considered point.

For a more detailed description of the Time Of Flight analysis procedure see also Appendix D. From this procedure the drift velocity, the beam temperature and the velocity distribution, are obtained for every nozzle temperature. By setting the appropriate mass in the mass filter of QMA both the molecular and the atomic velocity distribution can be measured, from a partially dissociated beam.

²H. Pauly chapter 2.1.1 and 3.6.4

2.3 Polarized Atomic Beam Source (ABS2)

The apparatus called ABS2 is presented in fig. 2.18. It is a standard ABS[48], with focusing sextupole magnets, built at the beginning of 1990s at the University of Wisconsin and formerly used at the Indiana University Cyclotron Facility (IUCF), where it has been in operation until its removal to Ferrara in 2002.

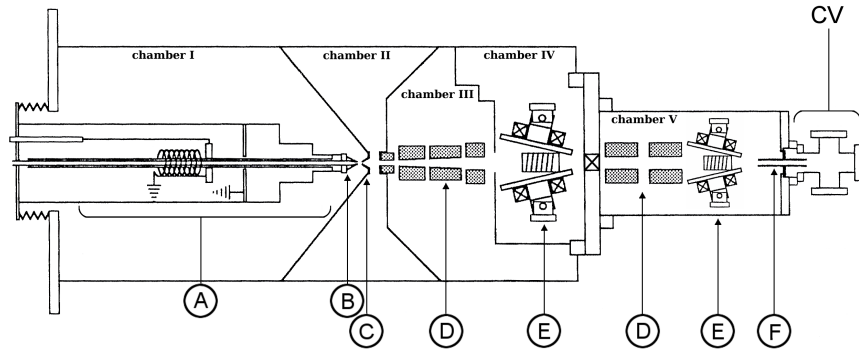


Figure 2.18: Atomic Beam Source “ABS2”: (A) Dissociator, (B) nozzle, (C) skimmer, (D) sextupole magnets, (E) RF transition units, (F) injection tube, (CV) compression volume.

The system is located in five vacuum chambers. Hydrogen or deuterium is dissociated by a RF dissociator, coupled to a cooled nozzle as described in paragraph 2.3.2. Atoms with electronic spin state $m_j = +1/2$ are focused by two sets of sextupole permanent magnets, described in paragraph 2.3.3; atoms with spin state $m_j = -1/2$ are defocused and thus removed from the beam. Between the two sets of magnets is located a MFT (Medium Field RF Transition unit) as shown in fig. 2.18, label (E). For a detailed description of this item see [49].

2.3.1 Pumping system

The five pumping chambers are separated by baffles, shown in fig. 2.18 and 2.19, whose geometry was chosen in order to maximize the conductance from the beam axis to the pumps.

The location of the pumps connections for chamber three and four is not evident from the drawing since they are connected on the sides of the vacuum chambers, in order to provide a high pumping conductance.

A scheme of the pumping system is presented in fig. 2.19. Table 2.1 lists the characteristics of the pumps and the pressures during normal operation (hydrogen beam).

Pressures in chambers 1-5 are measured by cold cathode gauges mounted on the chambers walls. The pressure between turbomolecular pumps and prevacuum pumps is measured by capacitance manometers.

The first chamber is pumped by two turbomolecular pumps in parallel, since it has the highest gas load: 85% of the total. The second chamber is pumped by a single turbomolecular pump. The three turbomolecular pumps exhausts (modified from the standard design in order to obtain larger conductance) are connected in parallel to a series of two root pumps and a mechanical prevacuum pump.

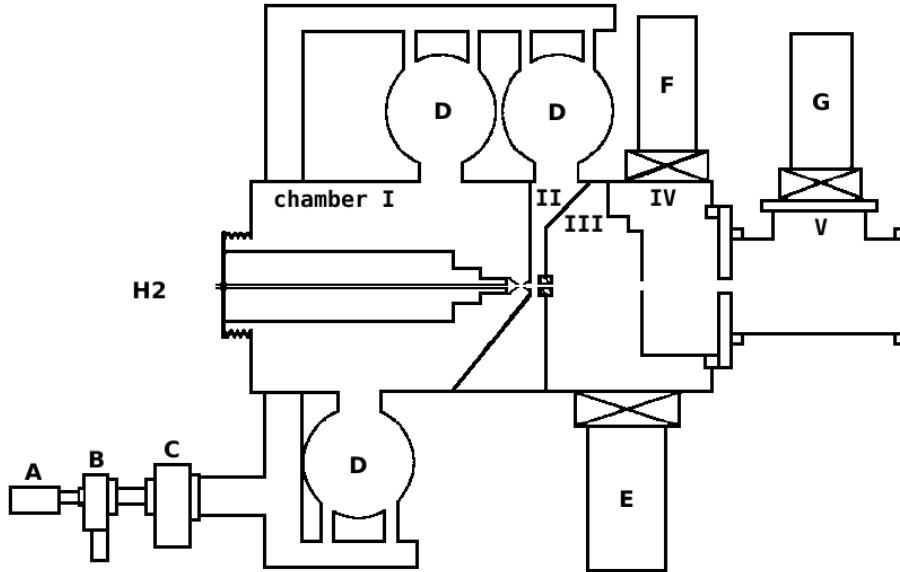


Figure 2.19: ABS2 pumping system. (A) Prevacuum Leybold trivac D60A pump, (B) Root Pfeiffer WKP250A SP pump, (C) Root Leybold ruvac WSU1001H pump, (D) Turbomolecular Pfeiffer TPU2200 pumps, (E) Cryogenic Ricor coolstar 1500 pump, (F) Cryogenic Varian HV8 pump, (G) Cryogenic Varian HV8 pump.

Table 2.1: Vacuum pumps

Chamber #	Label	Pump type	Pumping speed (H_2) [l/s]	Chamber pressure [mbar]
1	D	turbomolecular	2800	$3.4 \cdot 10^{-4}$
1	D	turbomolecular	2800	$3.4 \cdot 10^{-4}$
2	D	turbomolecular	2800	$6.5 \cdot 10^{-5}$
3	E	cryogenic	2500	$1.9 \cdot 10^{-6}$
4	F	cryogenic	2200	$8.8 \cdot 10^{-7}$
5	G	cryogenic	2200	$7.3 \cdot 10^{-7}$

The pumping speed of the first root pump was chosen to keep the fore-line pressure below $2.5 \cdot 10^{-2} \text{ mbar}$ at 5 mbar l/s gas load. At a reduced gas load of 1.7 mbar l/s the measured pressures are $1.0 \cdot 10^{-2}$ in the prevacuum and $6.5 \cdot 10^{-5}$ in chamber two. The resulting compression ratio is 170.

Chamber 3, 4 and 5 are pumped respectively by three cryogenic pumps. These pumps have valves that allow to isolate them from the chambers; a separate pumping system connected to a small turbo pump allows to regenerate them easily.

During normal operation the time between regeneration of cryo pumps is in the order of few days.

2.3.2 Dissociator

A schematic layout of the dissociator is displayed in fig. 2.20. Molecular gas, flowing through a pyrex tube of 9 mm inner diameter and 1 mm thickness, is dissociated into H atoms by an RF sustained discharge. The dissociator operates at a frequency of about 18 MHz and 200 W RF power, coupled capacitively to the hydrogen gas. Gas exits the dissociator through a standard 2 mm sonic nozzle, made of aluminum and cleaned with concentrated HNO_3 . This treatment provides the formation of an uniform layer of Al oxide that prevents the recombination on inner nozzle surface. The gap between the pyrex tube and the nozzle is kept as short as possible (less than 1.5 mm) in order to avoid elevated temperature region that could lead to intense recombination. The pyrex tube is cooled by water flow at a temperature of 13°C. The nozzle is cooled to 84 K by a liquid nitrogen dedicated line. This temperature is the ideal one to prevent surface recombination of atoms into molecules, both for aluminum and for pyrex.

A 4 mm skimmer (at a distance of 15 mm, see fig.2.20) together with a differential pumping system form a collimated beam that is focused at the end of the last chamber by sextupole permanent magnets.

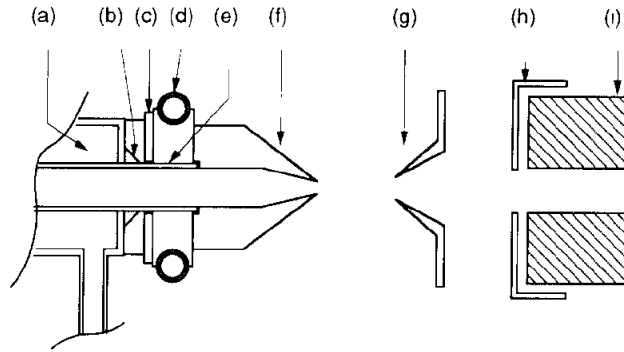


Figure 2.20: ABS2 nozzle and skimmer detail: (a) water cooling, (b) indium vacuum seal, (c) PTFE thermal insulator, (d) liquid N_2 cooling, (e) copper to pyrex indium joint, (f) nozzle, (g) skimmer, (h) collimator, (i) first magnet element.

2.3.3 Magnetic system

Two sets of permanent sextupole magnets provide the focusing on the beam axis of $+1/2$ electronic spin states and defocus $-1/2$. In order to improve the pumping system and therefore the vacuum, the magnets have been built as sets of three short sections instead of bulk magnets.

Multi-pole magnets are composed of segments permanently magnetized, whose magnetization axis advances azimuthally by an angle

$$\phi = \frac{2\pi(N/2 + 1)}{M} \quad (2.6)$$

where N is the number of wanted poles (6 in this case) and M is the total number of segments. Their geometry details are shown in fig. 2.21 and table 2.2.

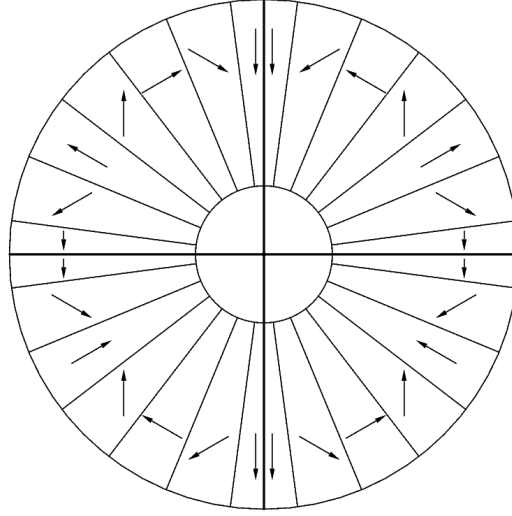


Figure 2.21: Magnetization direction of a 24-segments sextupolar permanent magnet.

Table 2.2: Magnets geometry (element number follows beam direction)

Element #	Entrance diam. [mm]	Length [mm]	Exit diam. [mm]	Elements spacing [mm]
1	10.5	25	10.5	10
2	12	50	16.5	10
3	16.6	60	22	12
4	25	35	25	360
5	25	62.5	25	10
6	25	62.5	25	-

The magnetic field in the bore of the magnets can be calculated from the geometry and the remnant field of the magnet material B_0 , using the following formula[48]:

$$B(r) = \left(\frac{r}{r_1}\right)^2 B_0 \frac{3}{2} \left[1 - \left(\frac{r}{r_0}\right)^2\right] \cos^3(\pi/M) \frac{\sin(3\pi/M)}{(3\pi/M)} \quad (2.7)$$

where r_1 is the radius of the bore and, r_0 is the outer radius of the magnet and M is the number of segments.

The first set of three magnets has a smaller inner diameter: for this reason it is composed of 12 segments only, in order to increase mechanical robustness. The remaining three magnets are composed of 24 segments and have a field (1.49 T at pole tip) that is larger than the 12 segments one (1.36 T). Segments magnetized radially and segments magnetized tangentially are made from different materials, which differ in the remnant field: 1.3 T vs 1.1 T. For the purpose of the calculations a mean value of $B_0 = 1.2 T$ has been used. Magnets are enclosed in welded stainless steel cans (of 0.3 mm thickness) in order to prevent magnetic material deterioration caused by atomic hydrogen. The gradual fall-off of the field at the ends of the magnets is not a problem if the integral under the curve (see

fig. 2.22) can be properly calculated. In this case the measured one (continuous line) is 8.34

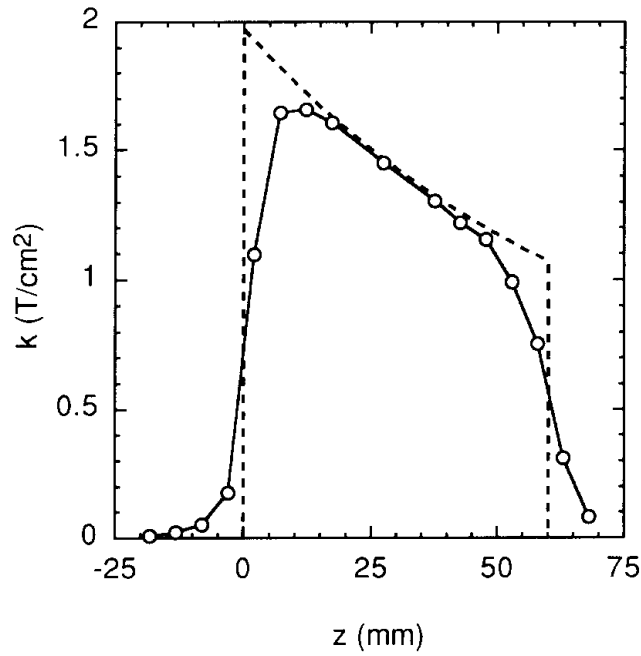


Figure 2.22: Measured quadratic coefficient k for the magnetic field in a 12 segment conical bore permanent sextupole magnet. The dashed line shows the field calculated. The points correspond to the measured data.

T/cm while the calculated one (dashed line) is 8.74 T/cm. The agreement is satisfactory and is similar for all the magnets.

2.4 Data Acquisition System (DAQ)

The SpinLab data acquisition system is based on a set of five personal computers (*spinlab1*, *spinlab2*, *spinlab3*, *spinlab4* and *spinlab6*), that are used for monitoring, control and acquisition purposes and a backup server (*hermes1*). They are all connected to an internal private network based on standard TCP/IP protocol and static IP addressing.

The software used for data acquisition, managing and storage is Labview[50], which can create Virtual Instruments (VI) that can both plot incoming data and send control signals. A virtual instrument is essentially a file (with extension *.vi*) and is presented to the user with two windows: "front panel" and a "block diagram".

The "front panel" is the window containing the live plots, indicators and controls. The user can interact with it by mouse/keyboard, also while the program is running, to change plots scales, change setpoints, send commands etc.

The "block diagram" represents what lies behind the VI and makes it work (data sources, virtual wiring connections, data analysis, loops etc). It can be modified only when the program is not running.

2.4.1 ABS1

The layout of ABS1 acquisition system is presented in fig. 2.23.

Computer *spinlab1*

Two VI "ControlABS" and "MonitPx_Pressioni" are present On the first PC *spinlab1*. *ControlABS* is dedicated to the first two chambers of ABS1: it reads (through RS-232 connection) the following pressures:

From Pfeiffer Multiguage (mod. TPG 256A) controller 1:

- P0 (pressure of the dissociator).
- PV1 (PreVacuum pressure for turbo 1).
- PV2 (PreVacuum pressure for turbo 2).
- HV1 (HighVacuum in Chamber 1).
- HV2 (HighVacuum in Chamber 2).
- HV2B (HighVacuum in Chamber 2, second gauge).

From MKS pressure/flow controller (mod. PR4000-S2V1N):

- Pressure in Chamber 2 or rest gas inlet flow depending on the device connected (vacuum *baratron gauge* mod. 627B-24340, 0.02 mbar full range or *mass-flow controller* mod. 20 SCCM/H₂).

From Oxford Instruments ITC (Intelligent Temperature Controller mod. 503):

- Nozzle temperature and heater voltage.

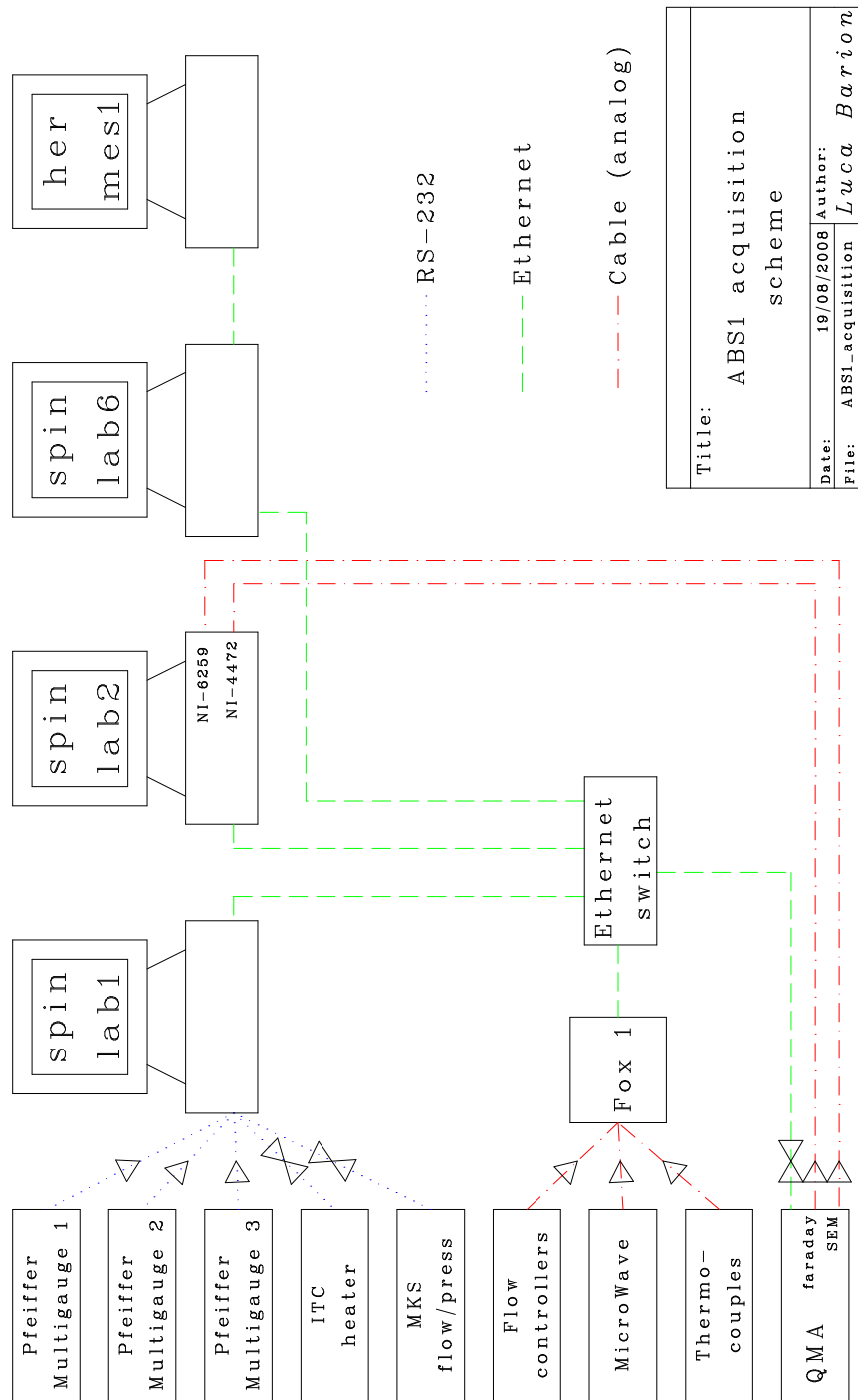


Figure 2.23: Data acquisition system scheme for ABS1.

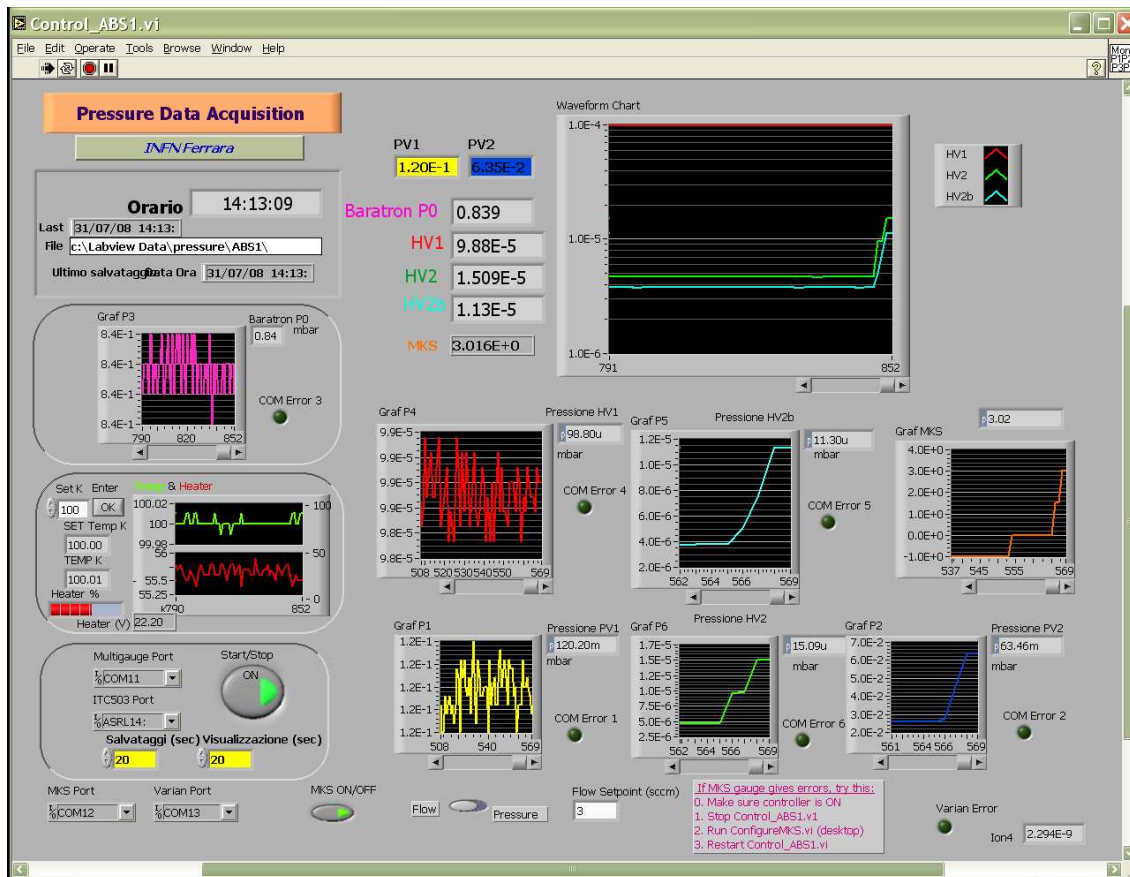


Figure 2.24: Control_ABS1.vi front panel.

This VI is used to log the data listed above (the data are saved on a plain-text file called ABS1_\$.DATE.txt) and has also two controls:

- MKS flow: when MKS controller is connected to the flow controller for rest gas inlet (see section 2.1.2), it varies the flow setpoint.
- Nozzle temperature: it can change the nozzle temperature setpoint on ITC.

Monit_px (see fig. 2.25) is dedicated to the vacuum of the diagnostic system: Chopper/Wheel (CW) Chamber 3 and Quadrupole Mass Analyzer (QMA) Chamber 4 of ABS1. It reads (through RS-232 connection) the following pressures:

From Pfeiffer Multigauge 2 controller:

- PV (PreVacuum pressure, common to Chamber 3 and 4).
- P_CV (pressure inside Compression Volume, connected to the exit of Chamber 2, on beam axis).
- P_CW (pressure in Chopper/Wheel Chamber 3).

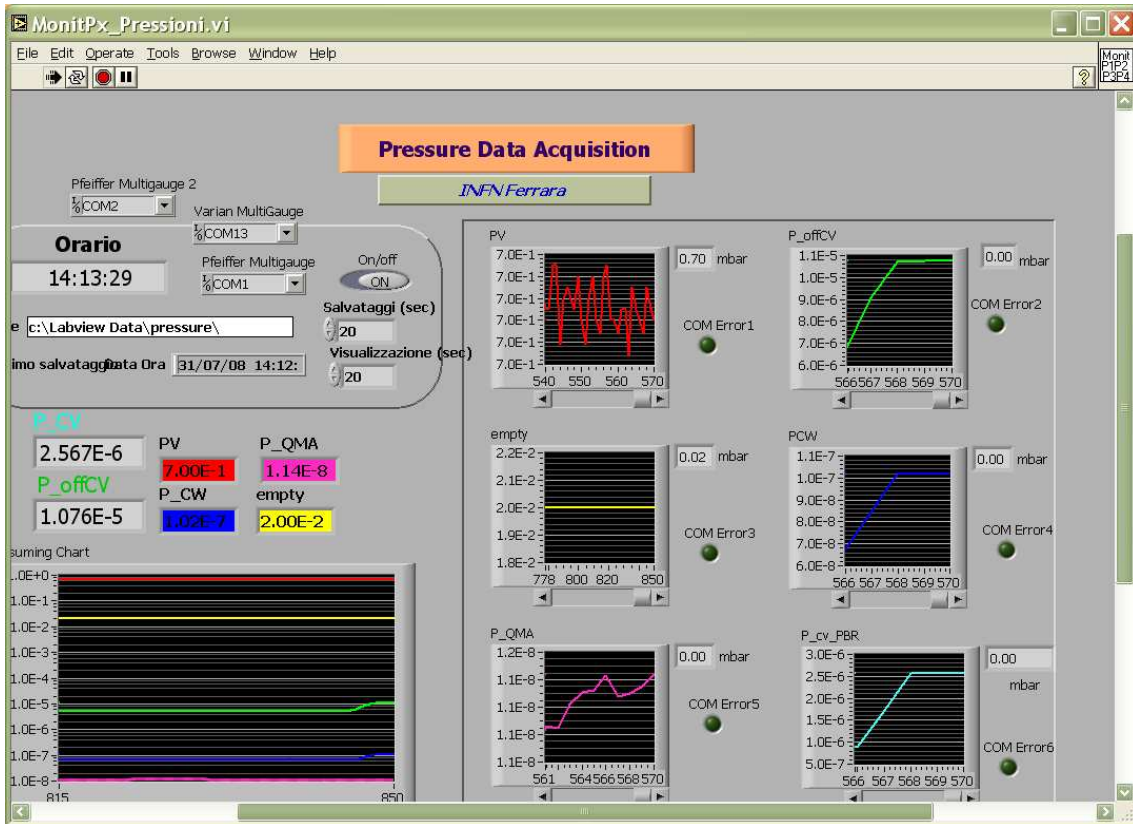


Figure 2.25: MonitPx_Pressioni.vi front panel.

- P_QMA (pressure in QMA Chamber 4).

From Pfeiffer Multigaugge 3 controller:

- P_offCV (pressure inside Compression Volume 2, that is off beam axis about 16°).

This VI is used to log the data listed above; the data are saved on a plain-text file called `Diag_$DATE.txt`.

Computer *spinlab2*

The second PC, *spinlab2*, is dedicated to the diagnostic system (Chamber 3 and 4 of ABS1) signals. It is equipped with two PCI-cards from National Instruments[50]:

- NI-4472 (slower, digital+analog trigger) used for alpha (degree of dissociation) measurements.
- NI-6259 (faster, digital trigger) used for TOF and OptMon measurements.

It runs two VIs (not at the same time): "Alphatime" and "TOF".

Alphatime plots (and saves to a file called *Alpha.txt*) the following data:

From NI-4472:

- *qat/qat_bkg* (QMA atomic signal and background).
- *qmol/qmol_bkg* (QMA molecular signal and background).
- α_{QMA} (dissociation measured with the QMA, calculated from the quantities above).
- chopper frequency.

From NI-6259:

- *OM_atoms* (integrated atomic signals from the Optical Monitor).
- *OM_molecules* (integrated molecular signals from the Optical Monitor).
- α_{OptMon} (dissociation measured with the Optical Monitor, calculated from the above quantities).
- *OM_water* (water peak integral from OpticalMonitor).

From FoxBox 1:

- temperatures (*oring*, *collar*, *nozzle*, *chamber 2 walls* + *cooling water* and *heater1* *heater2* that are saved but not displayed).
- gas flux (*H₂*, *O₂*, *N₂*, *He*).
- MW (Microwave forward and reflected power).

TOF instead is used for Time Of Flight measurements. It reads the QMA atomic and molecular signals (in different runs) through the NI-6259 board. The data are displayed and saved to a plain-text file chosen by the operator at the end of the acquisition cycle. Both VIs control the QMG700 through ethernet connection by means of the OPC³ commands *start*, *stop*, *change_mass*.

Computer *spinlab4*

It is a standard PC used to control the QMG700 with its own software, called *Quadera* and to store documentation/datasheets in electronic format.

³OLE for Process Control, an industrial standard

2.4.2 ABS2

The layout of the data acquisition system for ABS2 is presented in fig. 2.26.

Computer *spinlab3*

The *spinlab3* computer is dedicated to ABS2 and calibrated gas injection system. It runs the VI called "MonitPx_ABS2", that plots and saves the following pressures and temperatures from FoxBox2 (through ethernet connection):

- Chamber 1.
- Chamber 2.
- Chamber 3.
- Chamber 4.
- MKS (baratron on compression volume).
- Water_temp (temperature of cooling water for pumps).

and the following pressure from Pfeiffer Multigauge (through RS-232 connection):

- P0 (dissociator pressure).
- Prf_mag (pressure in the rf/magnet chamber).
- P1b (second gauge of chamber 1).
- Pcv (Compression Volume pressure).
- CV_cmr (Compression Volume pressure second gauge).
- Beam_mon (Pressure of calibration volume).

On *spinlab3* runs also a set of three VI controlling the regulating valve of the calibrated gas injection system. They allow to set a defined setpoint, to gradually increase the setpoint from a starting value to a final value in steps of 50 mV or to monitor the actual pressure.

2.4.3 Computer *spinlab6*

It runs Debian GNU/Linux v 4.0 and is mainly a server machine, since it offers the following services:

- gateway to Internet (with masquerading of internal IP addresses).
- port forwarding which gives the possibility to reach some internal services from outside the private network.
- backup services (data files are sent to a separate storage server *hermes1* every night).
- network testing programs.

On *spinlab6* general purpose utilities/servers such as network testing, ssh, textutils etc. are also installed.

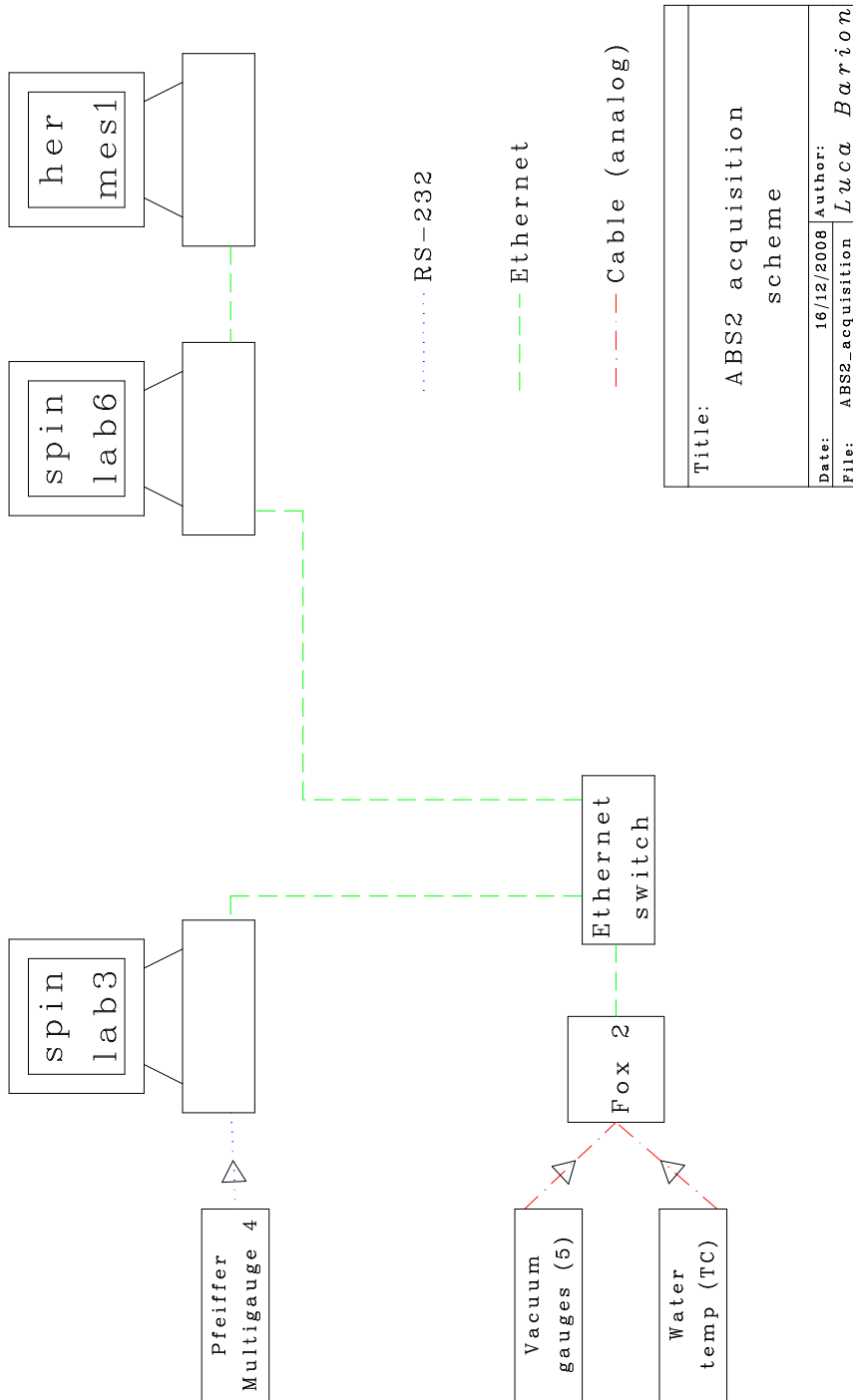


Figure 2.26: Data acquisition system scheme for ABS2.

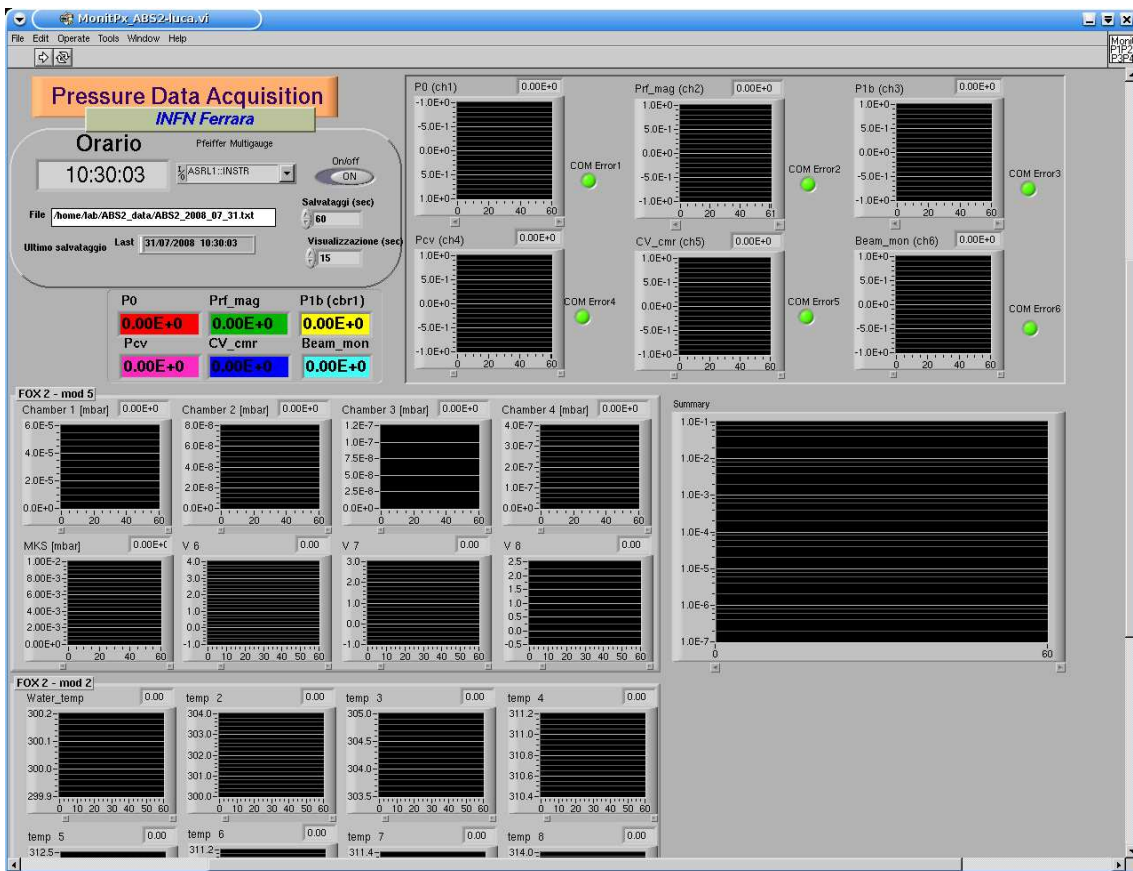


Figure 2.27: MonitPx_ABS2.vi front panel.

2.4.4 Fox Box

FoxBox is a data acquisition system based on ethernet connection. It runs a customized embedded version of Gentoo Linux.

It presents two key features: it makes possible to read remotely 16 analog inputs (-10V to +10V) and 16 temperatures (ThermoCouples type J) with one single ethernet cable; additionally it allows the digitalization of the signals near the source, so the noise is kept very low. It is composed of standard industrial components enclosed in a metallic box:

- One Fox board from Acmesystems s.r.l. [51]. A small PC on a tiny board of 66 x 72 mm (so called system-on-chip), that runs Linux (kernel version 2.4.31).
- Four Idam modules [52]. Industrial modules that read analog voltages (mod. *I* – 7017, precision 0.1V) or thermocouples (mod. *I* – 7018, precision 0.1°C). The communication port is a standard RS-485.
- One RS-485 to USB converter (to connect the interface of Idam modules to the USB port of the Fox board).
- four push-buttons to control the programs on the Fox board.
- One LCD display (HD44780 compatible).
- One potentiometer to adjust display contrast.

The Fox board runs a program that waits commands on a TCP socket. The command is typically "read module n". Upon receiving such a command from the acquisition PC, it reads, through RS-485, the 8 channels of the requested module, formats the data in a human readable string and sends them back through the same TCP socket, to the computer. Then the connection is closed and the board is ready to receive the next command. All this information exchange is rather fast (for a slow control system) as it requires only ≈ 0.2 s.

On the same Fox board a program is also running, that manages the LCD display (see fig. 2.28). By means of 4 buttons on the front panel it is possible to select the voltages/temperatures displayed on the LCD panel (auto updated every 5 s). The LCD display program uses the same method to read the data through network connection to the listening tcp socket. In this way it is also possible to display the voltages/temperatures from another FoxBox on the same network segment. A third program reads the status of the four buttons and executes various tasks accordingly.

2.5 Ntuples

All the data are saved to human-readable text files on the computers *spinlab1*, *spinlab2* and *spinlab3*.

As already mentioned every night text files are automatically sent, through network, to the backup server called *hermes1*.

On this server a program is available that merges the text files containing the ABS1 and diagnostic system data and saves the result as an ntuple in *hbook* format. The ntuple can be read with *PAW* or converted to a *ROOT file* with the program *h2root* included in the *ROOT* package.

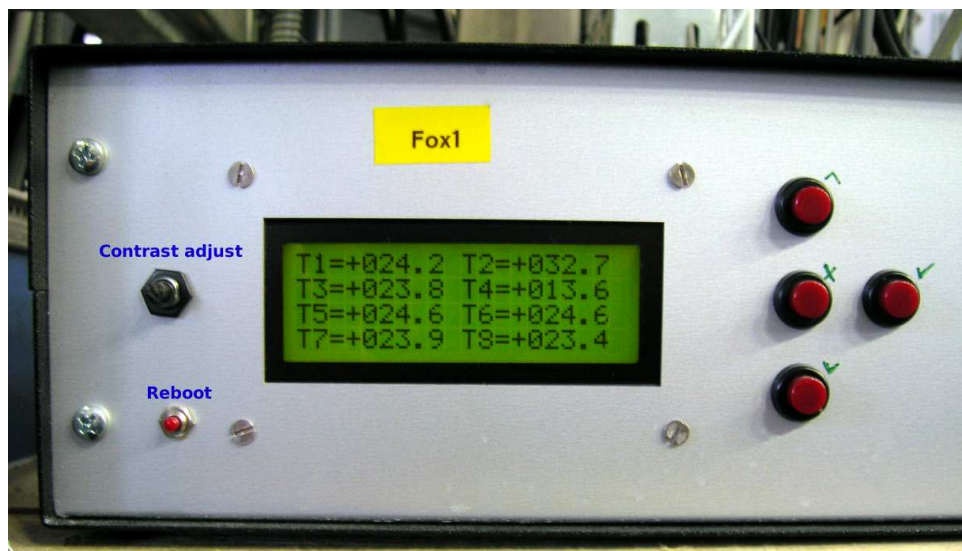


Figure 2.28: FOX box front panel with LCD display, reboot button, LCD contrast adjust knob and control buttons.

Chapter 3

Elastic scattering of the ABS beam with residual gas. Evaluation of attenuation coefficients and cross-sections

3.1 Motivation

3.1.1 Historical background

The most simple way to increase the target thickness might seem to be to increase the atomic beam intensity I . Unfortunately this is not as straightforward as it might look like. In fact experiments have evidenced a sort of saturation effect of the atomic beam intensity of an ABS as function of the input flux. This effect is clearly demonstrated in the plot of fig. 3.1 where the results of the RHIC ABS [53][54] are shown.

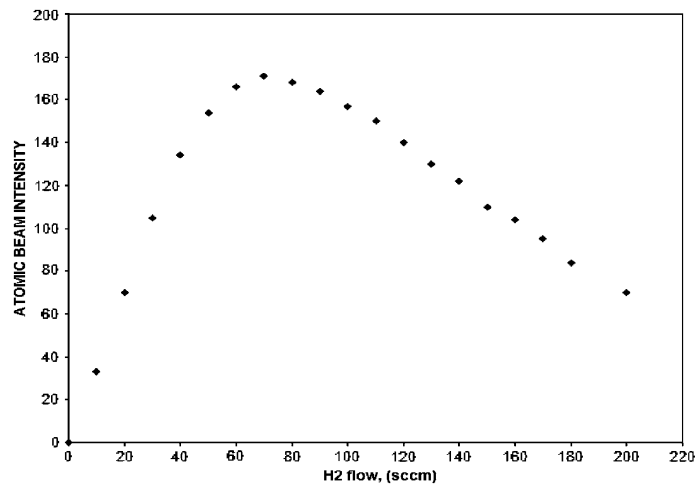


Figure 3.1: RHIC ABS beam intensity (in arbitrary units) as a function of input flux.

The intensity of an ABS depends on many correlated factors: the degree of dissociation in the discharge tube, the efficiency of the beam formation system, the temperature of the nozzle that defines the velocity distribution of the beam, the attenuation of the beam in the focusing system due to scattering with the background atoms and molecules and to intra beam scattering. Among others, the properties of the polarizing and focusing magnetic system are especially relevant.

The intensities of various atomic beam sources are presented in fig. 3.2, as function of the time of fabrication. The saturation effect quoted above is present, in the most different

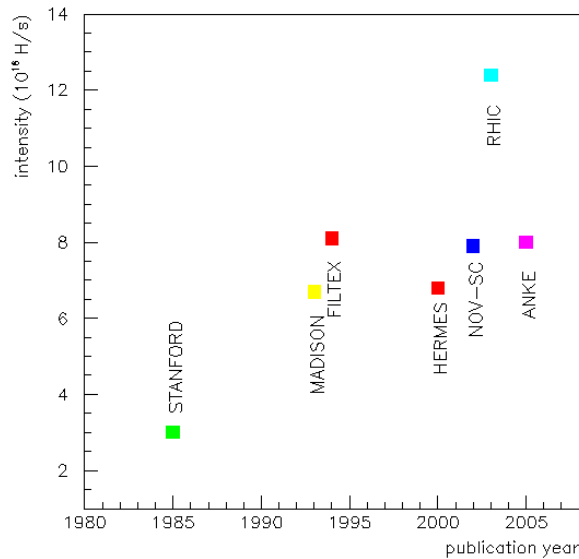


Figure 3.2: Atomic Beam Sources intensities in [$atoms/s$] listed according to publication year.

conditions in which the various ABS operate.

It is however interesting to draw attention on some features. All the ABS presented in fig. 3.2 have an axial symmetric magnetic system, generally consisting of a variable number of sextupoles. It can be demonstrated that for this typical geometry the acceptance atoms solid angle is proportional to the magnetic field strength at the largest usable radius of the magnet: the “pole tip” magnetic field. See for reference Appendix A of this thesis and ref. [4] and [55].

The Novosibirsk ABS (NOV-SC) is the only super-conducting source, reaching even $4.8 T$ at pole-tip [56], while all the other ABS of fig. 3.2 are normal conducting sources, with a pole-tip field of the order of $1 T$. Therefore based on the higher magnetic field of the focusing system an higher intensity was expected, compared to the other normal-conducting sources. The foreseen increase of the atomic beam intensity has not been observed.

The possible reason has been identified with *intra beam scattering*, which was not considered until the Novosibirsk result. On this basis, for a short period, it seemed that a physical limit to the ABS intensity had been reached.

Two years later the RHIC results opened the way to new speculations. In fact, from the simulations, the RHIC ABS intensity was expected to be about $8 \cdot 10^{16} atoms/s$ while the measured intensity is surprisingly higher. This result is still unexplained.

The mechanism responsible for the attenuation of an atomic beam produced in an ABS is still unknown. Understanding it is therefore of the utmost importance for future develop-

ments.

In particular it is not clear how to distinguish the attenuation caused by the collisions of the beam atoms with the background (*Rest Gas*, RG) from the *intra-beam scattering*.

3.1.2 Rest Gas Attenuation

The relevant quantity that allows to estimate the Rest Gas Attenuation (RGA) is the total cross section σ_{tot} for collision of the beam particles and the RG. This quantity is at present unknown, for the standard operational conditions of the various ABS.

We assume that the RG, extremely rarefied and uniformly distributed at constant pressure and temperature, can be considered a perfect gas, with intermolecular potential equal to zero and a Maxwellian velocity distribution. In this hypothesis the collisions between beam and rest gas particles are most likely to be binary collisions, involving only two particles (see [57]) and can be considered elastic. In order to obtain the attenuation of the beam that passes through the RG, in these conditions, it is possible to use the Beer's law.

Beer's law states that there is a logarithmic dependence between the transmission of a particle beam through a substance and the product of the absorption coefficient of the substance and the distance the beam travels through the substance (the path length), L . If the initial beam intensity is I_0 and the beam traverses a RG of length L , then the resulting intensity I is:

$$I = I_0 \exp \left[-\frac{A_I}{k_B T_{RG}} \int_0^L P dl \right] \quad (3.1)$$

where P and T_{RG} are the rest gas pressure and temperature, k_B is the Boltzmann constant and A_I is the *attenuation coefficient* that has the dimensions of an area.

In case of an homogeneous (temperature and pressure) gas, eq. 3.1 can be simplified:

$$I = I_0 \exp \left[-A_I \frac{PL}{k_B T_{RG}} \right] \quad (3.2)$$

This formula, that can be found in text books (for example [58]), has been derived in Appendix B for a monochromatic beam.

The attenuation coefficient A_I is connected to the total elastic cross section σ_{tot} , as discussed in section 3.3, in a complex way. In fact it can be demonstrated that the *attenuation coefficient* results from the convolution of three functions: the velocity distribution of the beam, the velocity distribution of the RG and the total cross section (see eq. 3.8). While the velocity distribution of the RG is similar in the various ABS and easy to calculate, the beam velocity distribution varies from an ABS to another, due to different nozzle temperature and geometries.

By measuring the *attenuation coefficient* and the velocity distributions it is possible to evaluate the total cross section, discriminating among various cross section models, in a range of temperature between 200 and 300K, where either experimental data or theoretical previsions are missing.

Previous studies of RGA report only the attenuation coefficient of the atomic beam as a function of the nozzle temperature [59] and therefore related to a well defined setup. Attenuation coefficients and total cross sections measured in this thesis as a function of the beam mean velocity are absolute physical quantities and can be used in the design of any ABS.

It is worthwhile to stress that apart the ABS field, the knowledge of such total cross sections σ_{tot} are of interest for many field in physics, as astrophysics, Bose-Einstein condensation, and polarized fusion.

In this chapter absolute measurements of the RGA and an evaluation of σ_{tot} as a function of the beam velocity are presented. The measurements have been carried out using the ABS1 apparatus described in chapter 3, section 2.4.1. Atomic and molecular beams of hydrogen and deuterium have been studied and their velocity distribution measured with the TOF technique (see section 2.2).

Section 3.2 presents in detail the measurement of the attenuation coefficient as a function of the beam velocity.

Section 3.3 describes an evaluation of the total cross section.

3.2 Measurement of the attenuation coefficient A_n

A beam that traverses a chamber containing *rest gas* will lose intensity due to collisions between beam particles and *rest gas* particles. The fraction of beam (n/n_0) that is not lost due to RGA is given by the equation:

$$\frac{n}{n_0} = \exp \left[-A_n \frac{PL}{k_B T_{RG}} \right] \quad (3.3)$$

where P is the pressure in the chamber, L is its length, k_B is the Boltzmann constant and T_{RG} is the rest gas temperature. A_n is the attenuation coefficient given in terms of the “number density” n of the beam, while A_I of equation 3.1 and 3.2 is the attenuation coefficient given in terms of beam intensity. A_n and A_I represent the weighted effective cross section as evident from the following equations (see Appendix B):

$$A_n = \frac{\int f(v_b) \sigma_{eff}(v_b) dv_b}{\int f(v_b) dv_b} \quad (B.16)$$

$$A_I = \frac{\int v_b f(v_b) \sigma_{eff}(v_b) dv_b}{\int v_b f(v_b) dv_b} \quad (B.17)$$

It is important to remind that with the QMA it is possible to measure n , while the compression volume measures I .

Using the unpolarized ABS1 apparatus, together with the diagnostic system, described in chapter 2, section 2.1 and 2.2, A_n can be determined varying the pressure in Chamber 2, by means of a side gas inlet (see fig. 2.1) and recording the corresponding beam density n measured with the QMA. Chamber 2 is large and unobstructed, therefore the rest gas is uniformly distributed and can be considered a very diluted perfect gas. The chamber pressure is monitored by a full-range hot cathode gauge and a full-range cold cathode gauge, both calibrated with a baratron to reduce the systematic error on the absolute chamber pressure to less than 5%.

The attenuation coefficient of hydrogen and deuterium beams, both atomic and molecular, was measured for several different beam velocity distributions by varying the nozzle temperature (see table 3.1) and diameter (see fig. 3.3). For each measurement, the beam

velocity distribution was directly measured with the TOF technique (see chapter 2, section 2.2 and Appendix D).

After dissociation, the beam is collimated by the skimmer that separates Chambers 1 and 2. The pressure in Chamber 2 can be increased by adding gas through the side inlet (see fig. 2.1 of chapter 2). Chamber 3 contains *chopper* and *wheel* that are used, respectively, for measuring the beam density and the beam velocity distribution. A time analysis of the resulting QMA signal reveals the beam's velocity distribution.

The dependence of the background-subtracted QMA signal S on the pressure P in Chamber 2 is given by the following equation, derived from the Beer's law (see previous section 3.1.2):

$$\ln(S) = \ln(S_0) - \frac{A_n P L}{k_B T_{RG}} \quad (3.4)$$

where S_0 is the beam signal in the QMA for null pressure (no attenuation) in Chamber 2, $L = 0.79 \text{ m}$ is the length of Chamber 2, T_{RG} is the temperature of the rest gas and k_B is Boltzmann's constant. As it will be presented in the next section, the attenuation constant A_n was measured for a particular nozzle geometry and temperature by varying the pressure in Chamber 2 in small steps until the QMA signal was 2/3 or less of its initial value.

Table 3.1: Nozzle temperatures

Data set	Nozzle temperatures
1	15 20 30 40 55 75 85 100 130 190 250 290
2,3	44 50 60 75 85 90 100 130 190 250 290
4	15 20 35 50 75 100 130 170 20 230 260 290
5	10 25 40 75 100 130 150 200 250 290
6,7	25 50 75 100 130 170

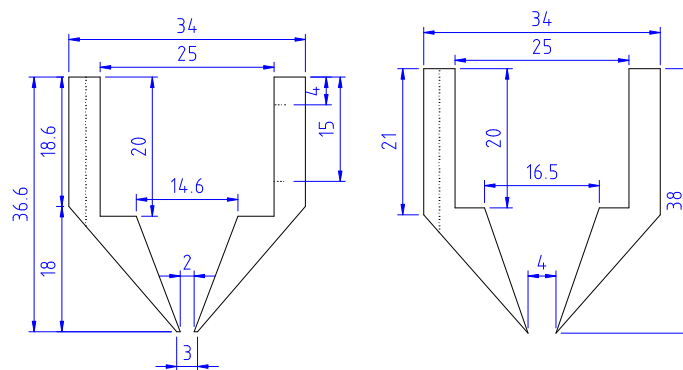


Figure 3.3: Nozzles geometries. Left: 2 mm (standard), right: 4mm.

3.2.1 Experimental procedure

The procedure adopted for the measurement of the attenuation coefficient consists in repeating the following steps for each nozzle temperature (table 3.1) and data sets (table 3.2):

- Measurement of the beam velocity distribution.
- Measurement of the beam density with the spectrometer QMA, while varying the pressure in the scattering chamber, Chamber 2.
- Correction of the QMA signal for drift (see below).
- Linear fit of $\ln(QMA)$ vs pressure in the scattering chamber ($HV2$).
- Extraction of A_n from the slope of the fit using eq. 3.5 (derived from eq. 3.2 and eq. 3.4).

$$A_n = -slope \cdot k_B \cdot T_{RG} / L_{eff} \quad (3.5)$$

where L_{eff} is used in place of L to account for the correction for attenuation losses between the scattering chamber and the spectrometer, as described below.

Before reaching the QMA, the beam travels through Chamber 2, Compression Volume CV and Chopper/Wheel chamber CW, as evident in fig. 2.1 of chapter 2.

The operational pressure in CV (P_{CV}) is about $2 - 4 \cdot 10^{-6} mbar$ and its length is about 30 cm and contributes to attenuation. For this reason, a correction is necessary: in place of real Chamber 2 length, an effective length (L_{eff}) has been introduced, that takes into account the attenuation in Compression Volume chamber.

The operational pressure in CW (P_{CW}) is less than $10^{-7} mbar$ and its length is 45 cm: the attenuation in this chamber is small (the contribution to L_{eff} is less than 0.1%) and can be neglected.

The ratio P_{CV}/P_{HV2} has been assumed as constant during a single measurement, but it might change between measurements. This change leads to different effective lengths.

The effective length has been calculated using the following equation:

$$L_{eff} = L_0 + 0.55 \cdot \frac{P_{CV}}{P_{HV2}} \quad (3.6)$$

where L_0 is the real Chamber 2 length (0.79 m) and 0.55 is a coefficient obtained from the ratio of Chamber 2 and CV length, and takes also into account pressure bumps caused by CV chamber geometry. L_{eff} is calculated for each nozzle temperature, for each data sample and is larger than real length L_0 of the scattering chamber.

Data Sets

Data on molecular and atomic hydrogen and deuterium have been collected using 2 mm and 4 mm nozzles (see fig. 3.3). These data are divided into seven data sets, as listed in table 3.2.

The first two data sets correspond to the study of $H_2 - H_2$ scattering, in case of pure molecular hydrogen beam, and $H_2 - H_2$ scattering of the molecular part of a dissociated

Table 3.2: Data sets

Data set	Gas	Nozzle diam. [mm]	beam	microwave
1	Hydrogen	2	molecular	off
2	Hydrogen	2	molecular	on
3	Hydrogen	2	atomic	on
4	Hydrogen	4	molecular	off
5	Deuterium	2	molecular	off
6	Deuterium	2	molecular	on
7	Deuterium	2	atomic	on

hydrogen beam with the molecular rest gas.

The third refers to the interaction of the dissociated atomic beam and the rest gas, $H_1 - H_2$. The fourth one was carried out in order to explore the possible influence of a different nozzle geometry; in this case the data of a pure molecular beam produced in a dissociator equipped with a 4 mm nozzle have been taken (see fig. 3.3, right part).

The deuterium rest gas attenuation was also studied. Data set 5, 6 and 7 reproduce the same experimental conditions as set 1, 2 and 3, but with a different gas (both beam and RG): deuterium instead of hydrogen.

Procedure for data-taking

All the measurements have been performed after the system had reached stable conditions. The fixed parameters for all the measurements are listed in tables 3.3 and 3.4 (see also fig. 2.2 of chapter 2).

Table 3.3: Fixed parameters for hydrogen

	Discharge off	Discharge on
Collar heater	135 K	135 K
H_2 dissociator flow	125 sccm (50% of 250 sccm)	125 sccm (50% of 5 sccm)
O_2 dissociator flow	0 sccm (0% of 5 sccm)	2.5 sccm (50% of 5 sccm)
Microwave power	0	600 W

Table 3.4: Fixed parameters for deuterium

	Discharge off	Discharge on
Collar heater	135 K	135 K
H_2 dissociator flow	50 sccm (20% of 250 sccm)	50 sccm (20% of 5 sccm)
O_2 dissociator flow	0 sccm (0% of 5 sccm)	0.25 sccm (5% of 5 sccm)
Microwave power	0	600 W

For each nozzle temperature listed in table 3.1 the following procedure has been applied.

The ABS1 was set to a defined nozzle temperature and let stabilize, until the values for the temperatures, pressures and QMA signals were stable. The time required was of the order of one hour and dependent mainly on the time required by the nozzle to reach the temperature setpoint.

At the beginning of the measurement, a beam velocity distribution was recorded by means of the Time Of Flight technique (as described in sec. 2.2.2 of chapter 2).

After recording the initial conditions, the pressure in Chamber 2 was increased, by injecting H_2 (or D_2) from the RG side inlet (see fig. 2.1 of chapter 2 and section 2.1.2). After 5 minutes, enough to reach stable conditions, the data of pressure and QMA signal were recorded. The data listed in table 3.5 were monitored in order to check the stability of the ABS. The signal from the spectrometer and the pressure in Chamber 2 are the relevant

Table 3.5: Acquired data

signal name	unit	explanation
P_0	[mbar]	Dissociator pressure
$HV1$	[mbar]	Chamber 1 pressure
$HV2$	[mbar]	Chamber 2 pressure
$HV2b$	[mbar]	Chamber 2 pressure
P_{CV}	[mbar]	Compression Volume 1 pressure
P_{CV2}	[mbar]	Compression Volume 2 pressure
P_{QMA}	[mbar]	Quadrupole Mass Analyzer chamber pressure
T_{or}	[K]	O-ring temperature
T_{coll}	[K]	Collar temperature
T_{noz}	[K]	Nozzle temperature
$Chopper$	[Hz]	Chopper rotation speed
$H2$	[sccm]	Hydrogen or Deuterium flux through dissociator
$O2$	[sccm]	Hydrogen flux through dissociator
$MW/rerfl$	[W]	Microwave forward/reflected power

data for the calculations of the attenuation coefficient.

This procedure was repeated for increasing flows from the RG inlet (see tables 3.6, 3.7 and 3.8) until the signal from the QMA was reduced to about 2/3 of the initial value.

At the end of the measurement, the starting conditions of pressure in Chamber 2 were restored, in order to control the reproducibility and to possibly compensate for time instabilities.

After completing this procedure (that took few hours) the temperature of the nozzle was changed and the procedure started again at the new nozzle temperature.

Data analysis

Figure 3.4 and 3.5 report the different steps of the analysis for the A_n extraction.

The two plots of fig.3.4 show the raw data: the QMA signal (left panel) and the scattering chamber pressure (right panel) as a function of time.

Two modifications are made to the raw data before extracting the slope:

Table 3.6: Data set 1

Nozzle temperature [K]	RG inlet fluxes [sccm]
15	0.0 - 0.2 - 0.4 - 0.8 - 1.2 - 1.6 - 1.8
20	0.0 - 0.2 - 0.4 - 0.8 - 1.2 - 1.6 - 1.8 - 0.0
30	0.0 - 0.2 - 0.4 - 0.8 - 1.2 - 1.6 - 1.8 - 0.0
40	0.0 - 0.2 - 0.4 - 0.6 - 0.8
55	0.0 - 0.3 - 0.6 - 1.0 - 1.4 - 1.8 - 2.2 - 0.0
85	0.0 - 0.3 - 0.6 - 1.0 - 1.4 - 1.8 - 2.2 - 0.0
100	0.0 - 0.2 - 0.5 - 1.0 - 1.6 - 2.1 - 2.4 - 0.0
130	0.0 - 0.2 - 0.4 - 0.6 - 0.8 - 1.2 - 1.6 - 2.0 - 2.2
190	0.0 - 0.2 - 0.4 - 0.8 - 1.2 - 1.8 - 2.2 - 2.4 - 2.6 - 2.8
250	0.0 - 0.2 - 0.4 - 0.8 - 1.2 - 1.8 - 2.4 - 2.8 - 0.0
290	0.0 - 1.6 - 0.8 - 2.4 - 3.2 - 4.0 - 0.0

Table 3.7: Data set 2 and 3

Nozzle temperature [K]	RG inlet fluxes [sccm]
44	0.0 - 0.2 - 0.2 - 0.5 - 0.5 - 1.0 - 1.0 - 1.4 - 1.4 - 2.0 - 2.0 - 0.0
50	0.0 - 0.2 - 0.4 - 0.8 - 1.2 - 1.6 - 2.0 - 2.2 - 2.6 - 2.8 - 3.0 - 0.0
60	0.0 - 0.4 - 0.8 - 1.4 - 1.8 - 2.2 - 2.6 - 3.0 - 0.0
75	0.0 - 0.2 - 0.4 - 0.8 - 1.2 - 1.6 - 0.0
85	0.0 - 0.4 - 0.8 - 1.2 - 1.6 - 2.0 - 2.4 - 3.0 - 0.0
90	0.0 - 0.2 - 0.8 - 1.2 - 1.6 - 2.0 - 2.4 - 3.0 - 0.0
100	0.0 - 0.3 - 0.8 - 1.4 - 1.8 - 2.2 - 2.6 - 3.0 - 0.0
130	0.0 - 0.3 - 0.8 - 1.4 - 1.8 - 2.2 - 2.6 - 3.0 - 0.0
190	0.0 - 0.2 - 0.8 - 1.4 - 1.8 - 2.2 - 2.6 - 3.0 - 0.0
250	0.0 - 0.4 - 0.8 - 1.4 - 2.0 - 2.6 - 3.0 - 3.4 - 0.0
290	0.0 - 0.4 - 0.8 - 1.2 - 1.6 - 2.0 - 2.4 - 3.0 - 3.4 - 4.0 - 0.0

- the drift in time, if any, of the QMA signal is accounted for.
- the points corresponding to a change in chamber pressure are excluded.

The drift of the QMA signal can be observed in the right panel of figure 3.4, in which the QMA signal does not return to its initial value at the end of the measurement even if the pressure in Chamber 2 (see left panel) returns to the starting value. Two possible explanations for such a drift exist:

- Unstable dissociation. The atomic fraction of the mixed beam which depends strongly on the surface conditions inside the dissociator could change during time.

Table 3.8: Data set 4

Nozzle temperature [K]	RG inlet fluxes [sccm]
15	0.0 - 0.2 - 0.4 - 0.8 - 1.2 - 1.6 - 1.8 - 0.0
20	0.0 - 0.2 - 0.4 - 0.8 - 1.2 - 1.6 - 1.8 - 0.0
35	0.0 - 0.2 - 0.4 - 0.8 - 1.2 - 1.6 - 2.0 - 0.0
50	0.0 - 0.4 - 0.8 - 1.2 - 1.6 - 1.8 - 2.2 - 0.0
75	0.0 - 0.4 - 0.8 - 1.2 - 1.6 - 2.0 - 2.4 - 0.0
100	0.0 - 0.4 - 0.8 - 1.2 - 1.6 - 2.0 - 2.4 - 0.0
130	0.0 - 0.4 - 0.8 - 1.2 - 1.8 - 2.2 - 2.6 - 0.0
170	0.0 - 0.4 - 0.8 - 1.2 - 1.8 - 2.2 - 2.6 - 0.0
200	0.0 - 0.4 - 0.8 - 1.2 - 2.0 - 2.4 - 2.8 - 0.0
230	0.0 - 0.4 - 1.0 - 1.5 - 2.0 - 2.6 - 3.0 - 0.0
260	0.0 - 1.0 - 2.0 - 2.5 - 3.0 - 3.4 - 3.8 - 0.0
290	0.0 - 0.5 - 1.0 - 1.6 - 2.5 - 3.2 - 4.0 - 0.0

- Instabilities in the temperature of the filament of the QMA and in general its ion source.

Before performing the linear fit, the QMA data are corrected for the drift, according to the formula:

$$\ln(QMA) = \ln(S_2) + C \cdot t. \quad (3.7)$$

where QMA is the corrected spectrometer signal, S_2 is the real spectrometer signal and $C = (S_2(t_{end}) - S_2(t_{start})) / (t_{end} - t_{start})$ is the difference between the signal S_2 at the beginning and at the end of the measurement, divided by the total time of the measurement.

Figure 3.5 shows the data before (left panel) and after (right panel) this correction.

The values of C for each measurement are reported in tables 3.9 and 3.10.

The left plot of fig. 3.5 shows how the transition points are removed. After correcting for QMA time drift, all the points are fitted to a line to determine preliminary values for the fit parameters. Transition points are identified as those outside a *reasonable*¹ distance from the line, indicated in the fit.

The fit parameters are subsequently re-calculated excluding these points, and the result is shown in right panel.

These two corrections improve the fit quality (χ^2/ndf), as indicated on the plots legends of fig. 3.5.

The attenuation coefficient A_n is proportional to the slope obtained from the fit.

This procedure is repeated for all the nozzle temperatures of all the data sets. The resulting data are listed in tables 3.9 and 3.10, where all the quantities related to the analysis are shown.

A systematic error on A_n is included, corresponding to the accuracy of the determination of C , that is $\Delta C = 0.364 \times 10^{-4} \text{ s}^{-1}$.

¹reasonable distance is judged by eye

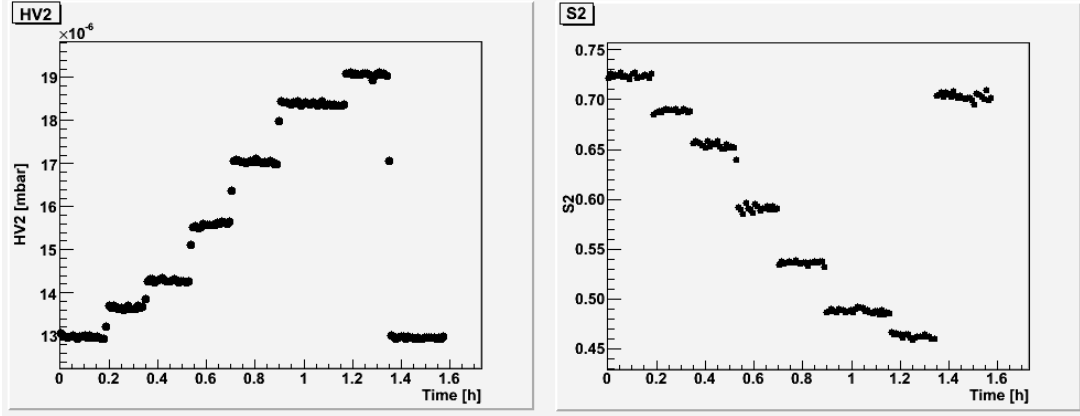


Figure 3.4: Data analysis first step. Pressure in scattering chamber (Chamber 2) and raw signal from QMA are plotted as a function of time ($T_{noz} = 20K$, data set 1).

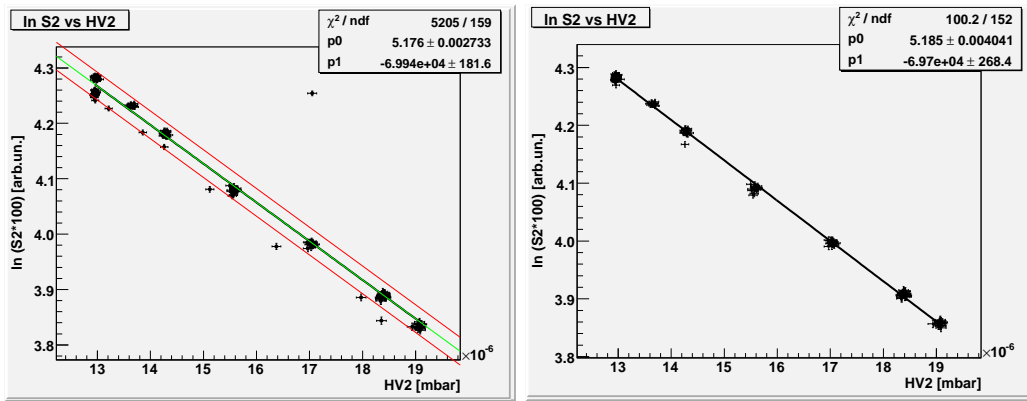


Figure 3.5: Data analysis procedure. In the left panel the QMA raw signal is plotted as a function of the Chamber 2 pressure. In the right panel a correction for time drift (see eq. 3.7) has been applied to the QMA signal and transition points (those outside the red lines in left panel) have been removed; the fit is performed on the remaining data. ($T_{noz} = 20K$, data set 1).

If at the end of the measurement the chamber pressure did not return to its starting value, a systematic error equal to the average correction of the other measurements was assigned to the extracted slope.

Time Of Flight

In order to relate the attenuation coefficients A_n to the mean beam velocity, a time of flight distribution was measured for every nozzle temperature listed in table 3.1. An example of TOF analysis can be found in Appendix D.

Table 3.9: Rest Gas attenuation data for sets 1 and 2

Data set 1						
Nozzle	v_b	χ^2/dof	slope	C	L_{eff}	A_n
[K]	[m/s]		[mbar-1]	$10^{-4} [s^{-1}]$	[m]	$[A^2]$
15	1027	85.4/181	-74720.2 ± 243.7	1.106	0.897	138.50 ± 6.74
20	1067	100.2/152	-69696.5 ± 268.4	1.824	0.897	129.19 ± 3.40
30	1125	147.6/176	-67367.6 ± 232.1	0.832	0.898	124.73 ± 2.31
40	1162	82.9/122	-66275.3 ± 589.7	1.106	0.897	122.85 ± 9.84
55	1249	85.2/143	-61003.8 ± 235.3	0.000	0.897	113.07 ± 4.36
75	1326	175.4/223	-51534.9 ± 142.5	1.106	0.888	96.49 ± 7.82
85	1391	80.1/129	-54891.0 ± 227.8	1.809	0.898	101.63 ± 2.51
100	1458	70.6/112	-52135.4 ± 226.8	0.000	0.897	96.64 ± 1.78
130	1540	1168/374	-42716.3 ± 109.9	1.106	0.891	79.71 ± 9.42
190	1712	188.2/221	-39209.2 ± 100.2	1.106	0.889	73.33 ± 4.39
250	1903	138.8/142	-41604.1 ± 195.1	2.171	0.897	77.12 ± 1.50
290	1941	1013/176	-38371.6 ± 102.1	-1.409	0.895	71.28 ± 1.29
Data set 2						
Nozzle	v_b	χ^2/dof	slope	C	L_{eff}	A_n
[K]	[m/s]		[mbar-1]	$10^{-4} [s^{-1}]$	[m]	$[A^2]$
44	1612	71.7/163	-45704.9 ± 313.5	-0.910	0.902	84.25 ± 1.82
50	1614	147.8/238	-44673.2 ± 225.4	-1.800	0.899	82.62 ± 1.66
60	1650	86.7/162	-43925.8 ± 281.5	-1.460	0.898	81.33 ± 1.56
75	1700	273.7/248	-44369.7 ± 160.5	1.248	0.890	82.89 ± 5.46
85	1727	80.4/172	-41396.6 ± 272.6	0.723	0.899	76.56 ± 1.50
90	1756	153.8/214	-42899.0 ± 210.9	0.832	0.899	79.34 ± 2.13
100	1786	54.5/159	-40474.5 ± 312.7	0.358	0.899	74.86 ± 1.48
130	1893	145/190	-39546.3 ± 202.6	0.000	0.899	73.14 ± 1.49
190	1959	73.9/188	-37818.2 ± 175.9	0.000	0.897	70.10 ± 1.84
250	2058	113.3/165	-37113.1 ± 191.9	2.160	0.897	68.79 ± 1.31
290	2085	196.7/238	-36831.1 ± 125.5	-1.950	0.897	68.27 ± 1.75

Table 3.10: Rest Gas attenuation data for sets 3 and 4

Data set 3						
Nozzle	v_b	χ^2/dof	slope	C	L_{eff}	A_n
[K]	[m/s]		[mbar-1]	$10^{-4} [s^{-1}]$	[m]	$[A^2]$
44	1737	438.7/161	-37901.8 ± 109.4	0.000	0.902	69.86 ± 1.56
50	1736	30.3/236	-38265.2 ± 317.1	4.690	0.899	70.77 ± 1.56
60	1791	30.8/156	-37903.4 ± 417.0	4.730	0.898	70.18 ± 1.52
75	1896	133.4/252	-35985.0 ± 143.1	0.000	0.890	67.23 ± 5.40
85	1896	22.4/168	-36475.4 ± 433.1	3.980	0.899	67.46 ± 1.50
90	1935	47.2/210	-36082.9 ± 350.3	1.250	0.899	66.73 ± 2.07
100	1967	17.5/158	-35281.2 ± 467.8	2.150	0.899	65.25 ± 1.49
130	2114	555.2/194	-33443.0 ± 67.4	-0.455	0.899	61.85 ± 1.31
190	2199	226.5/169	-31288.7 ± 86.1	-0.234	0.897	58.00 ± 1.61
250	2308	312.3/156	-31018.2 ± 132.6	1.440	0.897	57.49 ± 1.11
290	2296	337.3/235	-31697.2 ± 185.5	4.680	0.897	58.75 ± 1.67
Data set 4						
Nozzle	v_b	χ^2/dof	slope	C	L_{eff}	A_n
[K]	[m/s]		[mbar-1]	$10^{-4} [s^{-1}]$	[m]	$[A^2]$
15	959	108.3/140	-76887.6 ± 296.8	-0.723	0.892	143.32 ± 2.59
20	987	124.7/131	-75471.5 ± 298.0	0.000	0.892	140.68 ± 2.54
35	1067	89.8/126	-69912.5 ± 268.3	0.072	0.892	130.31 ± 2.34
50	1143	130.9/136	-65492.8 ± 216.4	0.000	0.892	122.08 ± 2.19
75	1213	474.7/114	-59668.4 ± 220.3	3.570	0.892	111.22 ± 2.09
100	1312	136.1/134	-54970.0 ± 183.6	0.000	0.892	102.46 ± 2.05
130	1419	104.3/122	-51192.3 ± 172.6	0.000	0.892	95.42 ± 1.80
170	1531	175.1/127	-47927.2 ± 164.0	0.000	0.892	89.33 ± 1.76
200	1610	210.5/120	-44943.4 ± 152.6	0.000	0.892	83.77 ± 1.64
230	1678	293.7/125	-43432.8 ± 142.3	0.000	0.892	80.96 ± 1.45
260	1738	109.6/109	-40191.2 ± 122.8	-3.700	0.891	75.00 ± 1.31
290	1795	424.3/129	-41040.9 ± 117.7	0.592	0.892	76.50 ± 1.34

Hydrogen

The measured attenuation coefficient A_n for molecular hydrogen beam are presented in fig. 3.6, as function of the nozzle temperature (top panel) and of the mean velocity (bottom panel).

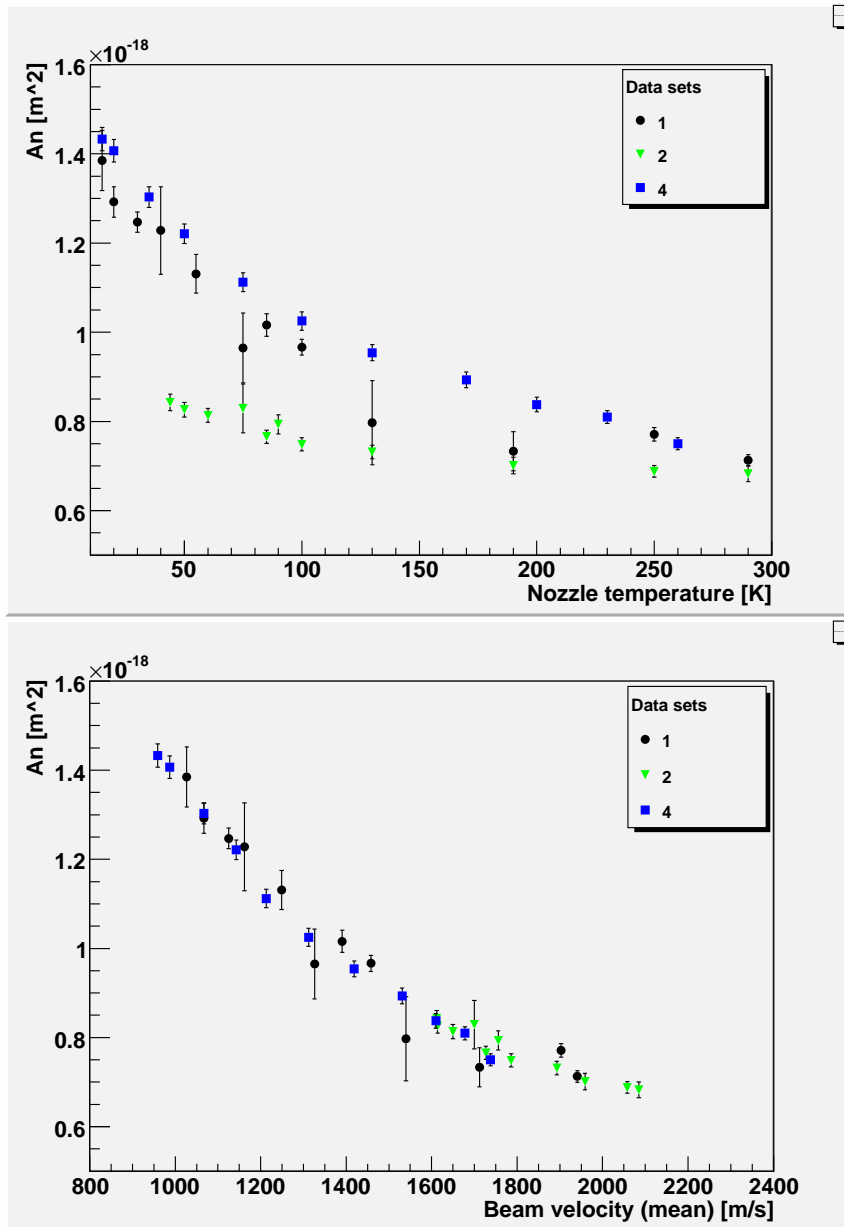


Figure 3.6: Measured attenuation coefficient for molecular hydrogen beams as function of nozzle temperature (top panel) and beam mean velocity (bottom panel).

All the molecular data sets have been included: both the pure molecular hydrogen beams (2mm and 4 mm nozzle) and the H_2 fraction of the dissociated beam are presented in the same plot.

As clearly visible in the top plot, the different data sets 1, 2 and 4 (see table 3.1) do not

lie on the same line, if they are plotted as a function of the nozzle temperature.

This fact is due to the different beam formation conditions, even for the same temperature of the nozzle: a larger diameter nozzle provides different conditions for the gas expansion; also the presence or absence of atoms (discharge on or off) affects the properties of the molecular beam, especially particles velocities).

The discrepancy disappears if the A_n are plotted (bottom panel) as a function of beam mean velocity.

This evidence is shown here for the first time, since usually the ABS attenuation coefficients are given in terms of nozzle temperature (see ref. [4] and [59]).

As already mentioned this choice allows the application of the results of the measurements to different Atomic Beam Sources.

Deuterium

The attenuation coefficient have been measured also for molecular and atomic deuterium (sets 5 to 7). The results are presented in figure 3.7, which shows the attenuation coefficient for a molecular deuterium beam. Considering the bottom panel of fig. 3.6 and fig. 3.7

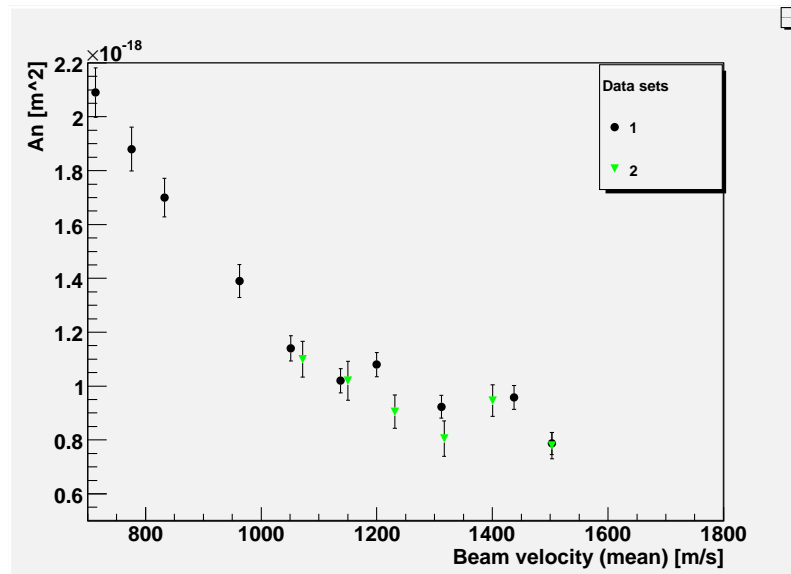


Figure 3.7: Measured attenuation coefficient for deuterium molecular beams as function of beam mean velocity.

it is possible to relate the attenuation coefficients for molecular hydrogen and deuterium. Comparing these two plots it is evident that these coefficients are similar and that A_n is slightly larger for hydrogen compared to deuterium, for the same beam mean velocity.

Atomic beams

The same conclusions are valid also comparing the atomic data for hydrogen and deuterium, as presented in fig. 3.8.

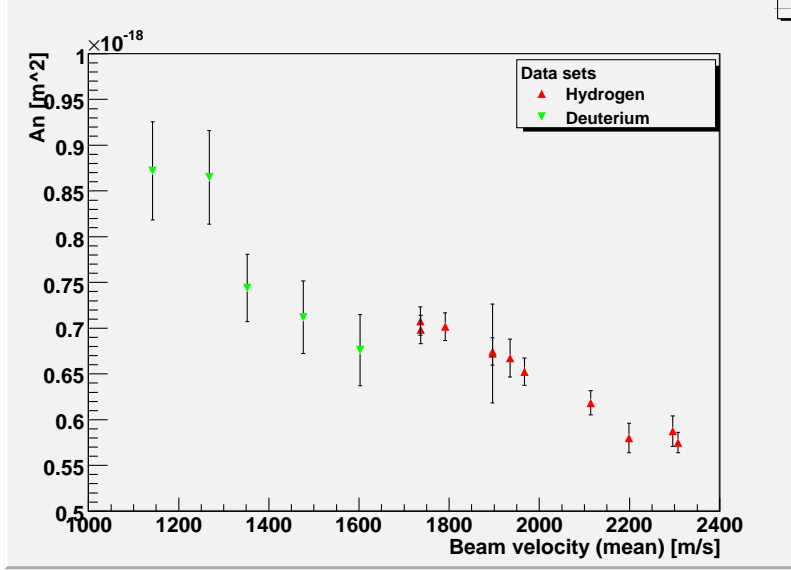


Figure 3.8: Measured attenuation coefficient for hydrogen and deuterium atomic beam as function of beam mean velocity.

3.3 Cross section evaluation method

The attenuation coefficient A_n can be expressed in the form:

$$A_n = \frac{1}{v_{mp}} \frac{\int f(v_b)dv_b \int \sigma_{tot}(g) \frac{g}{v_b} f(g, v_b)dg}{\int f(v_b)dv_b} \quad (3.8)$$

where v_b is the beam particle velocity, g is the relative velocity between beam and rest gas, and the relative velocity distribution $f(g, v_b)$ has been defined with the equation B.22 (see appendix B). Beam velocity distribution $f(v_b)$ and attenuation coefficient A_n are known from the measurements. However σ_{tot} can not be extracted analytically.

From the other hand, eq. 3.8 can be used to check the validity of various models for σ_{tot} . The *Hard Sphere* model (HS), the *Variable Hard Sphere* model (VHS) and generalized hard sphere model have been taken in consideration, together with an empirical linear model, to evaluate a calculated attenuation coefficient, called A_n^{calc} .

A_n^{calc} has been then compared to the data through the χ^2 method.

The method used to evaluate the total cross-section σ_{tot} consists in a comparison between calculated and measured attenuation coefficients, A_n^{calc} and A_n respectively.

The analysis steps are the following:

- different test functions called $\sigma_t(g)$ are created to describe the dependence of the cross section from the relative velocity g (for example $\sigma_{t1}(g) = C_1$, $\sigma_{t2}(g) = C_2 + C_3 \cdot g$, etc.).
- the result of the following convolution is calculated on the basis of the previously defined $\sigma_t(g)$: $A_n^{calc} = f(v_b) \otimes f(v_{RG}) \otimes \sigma_t(g)$.
- the parameters in the supposed $\sigma_t(g)$ are determined with the χ^2 minimization: $\chi^2 = \sum \frac{(A_n^{calc} - A_n)^2}{\delta^2(A_n)}$.

- the different χ^2 obtained for the various $\sigma_t(g)$ are compared to each other in order to evaluate which of the different test functions best fits the experimental data: $\chi_{t1}^2 < \chi_{t2}^2$ means that $\sigma_{t1}(g)$ model is better than $\sigma_{t2}(g)$.

The analysis is in progress. Here we present some preliminary results.

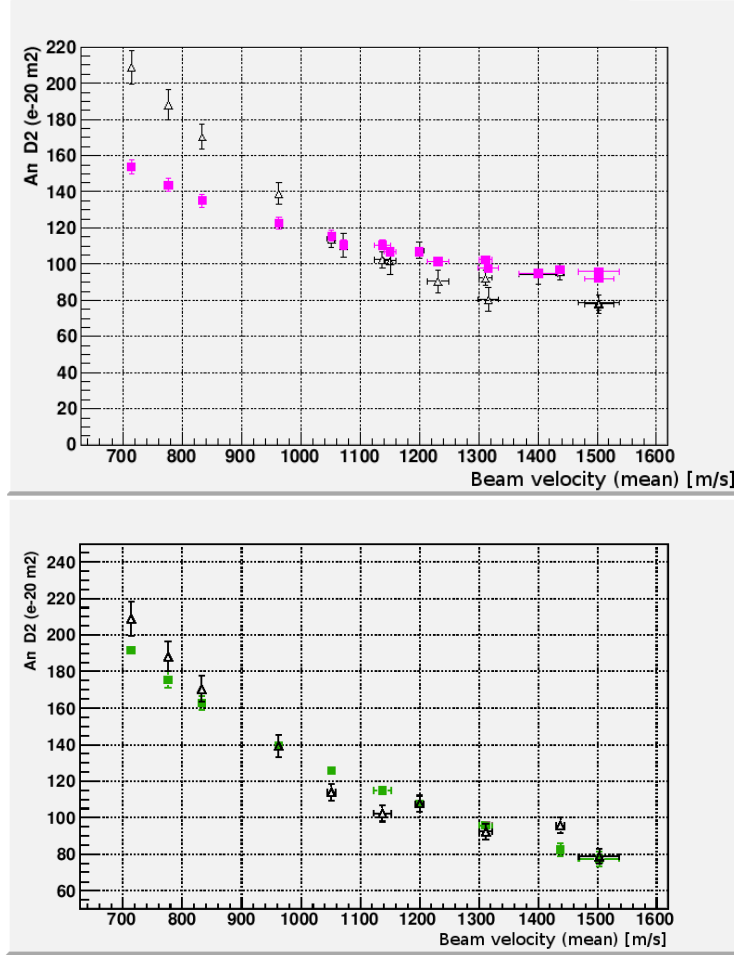


Figure 3.9: Attenuation coefficient A_n for molecular deuterium. Black triangles are the measured data, pink squares (top panel) are the data calculated using HS model and green squares (bottom panel) are the data calculated using VSS model.

Figure 3.9 shows the measured and calculated A_n coefficient for molecular deuterium. The top panel shows the calculated A_n^{calc} in the hypothesis of the HS model

$$\sigma_{tot} = \pi d^2 \quad (3.9)$$

as pink squares, while the triangles are the measured data. It is evident that this widely used model is inadequate to describe the experimental results.

The bottom panel of fig. 3.9 presents the calculated attenuation coefficients obtained with an empirical linear model for a pure molecular deuterium beam:

$$\sigma_{tot} = \pi d^2 - B(\bar{g} - \bar{v}) \quad (3.10)$$

where $\bar{v} = 1600 [m/s]$ is the mean value of the relative velocity of rest gas and beam particles. The measured data are much better represented, although this parameterization has no physical meaning.

Preliminary data on molecular hydrogen are shown in fig. 3.10. A_n have been calculated for the Hard Sphere model (red squares) expressed by equation 3.9 and the Variable Hard Sphere model (blue triangles), for which the parameterization is given by the equation:

$$\sigma_{tot} = \pi b^2, \quad b = (4.287B) \left(\frac{2467}{g} \right)^{0.8} \quad (3.11)$$

The black circles represent the measured data. A clear discrimination among model is pos-

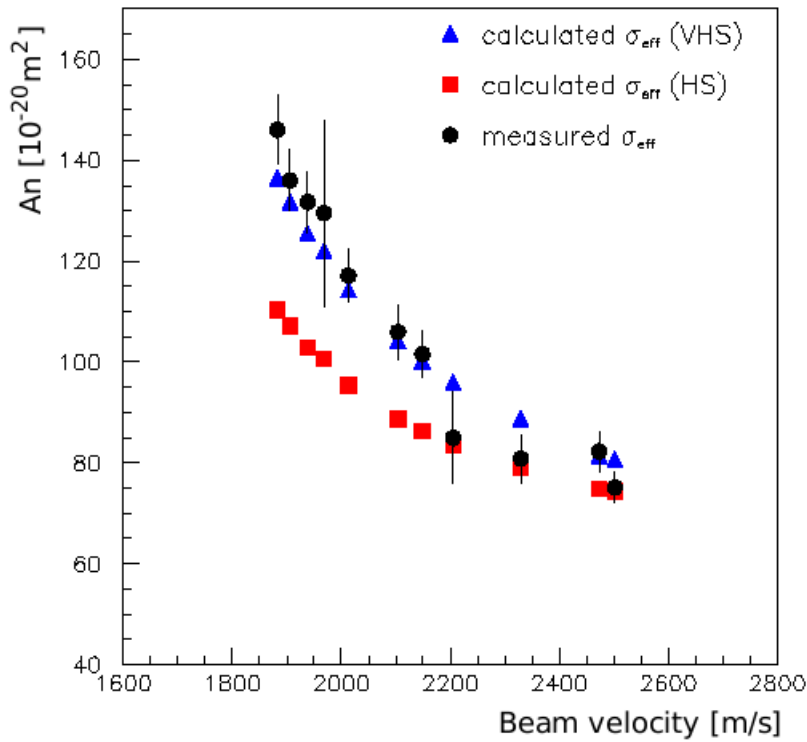


Figure 3.10: Measured and calculated values of A_n for different σ_{eff} models and values of the mean beam velocity.

sible. Furthermore the parameters determination for the VHS model allows the extraction of the total cross section σ_{tot} .

Chapter 4

New ideas part A: Finned injection tubes

4.1 Intensity of polarized internal targets

A standard Atomic Beam Source (ABS) produces a polarized hydrogen beam of about $10^{16}at/s$: the resulting integrated thickness (t) for the atomic jet, used as internal target in a storage ring, is quite low (of the order of $10^{11}at/cm^2$). The corresponding luminosity \mathcal{L} and event rate R can be calculated from eq. 4.1:

$$R = \sigma \mathcal{L} , \quad \mathcal{L} = t I \quad (4.1)$$

where I is the intensity of the stored particle beam (expressed in [*particles/sec*]) and σ is the reaction cross section. Typical intensities available in storage rings are of the order of $10^{18}s^{-1}$ (corresponding to a current of $160 mA$). The resulting luminosity is of the order of $10^{-29} cm^{-2}s^{-1}$, which is adequate for low energy reactions ($\sigma \approx 10^{-25} \div 10^{-31} cm^{-2}$), but not for high-energy particle reactions (Drell-Yan has a cross section of the order of $10^{-34} cm^{-2}$): the produced Drell-Yan event rate, with the intensity reported above, would be very low, of the order of one event per day.

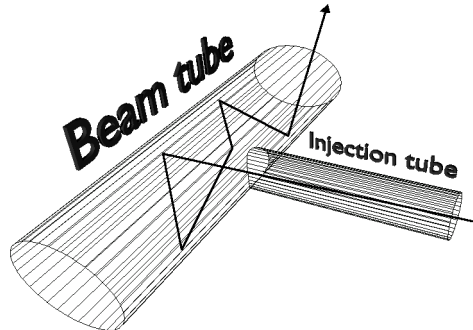


Figure 4.1: Example of storage cell geometry.

4.2 Finned injection tubes

In order to overcome this disadvantage one possibility (already proposed in 1966 by W. Haerberly[2]) is to inject the hydrogen jet in a *storage cell*. Since then many improvements have been done and today *storage cells* are commonly used as internal gaseous targets in nuclear physics experiments [60].

An exhaustive review of this technique is presented in ref. [4]. The base idea is to feed hydrogen atoms from an ABS into a ‘T’ shaped storage cell (see fig. 4.1): wall collisions slow down the atoms escaping from the cell, resulting in an increase in gas density and a wider stored-beam/target superposition.

In fact the target thickness traversed by the stored particle beam, integrated over the cell length, is about two order of magnitude higher than the atomic jet itself.

The atomic hydrogen from the collimated beam of an ABS enter the *storage cell* through an *injection tube* (IT), collide with the inner walls of the cell and diffuse out the cell through three possible paths: the two ends of the storage cell (*beam tube*) or back through the *injection tube* itself.

This section will explore the possibility to increase the target thickness by modifying the design of the *injection tube*.

In steady conditions, the target thickness (the gas density integrated along the cell length $2L$, [*atoms/cm²*]) depends on the intensity of the atomic beam entering the cell and the total cell conductance that results summing the *beam tube* C_{beam} and injection tube C_{inj} conductances[4]:

$$t = \frac{IL}{C_{tot}}, \quad C_{tot} = 2 \cdot C_{beam} + C_{inj} \quad (4.2)$$

If cell conductance C_{tot} could be reduced, the target thickness would be increased. For this purpose a test study has been performed, in which the standard injection tube was replaced by a *finned tube*, that is a cylindrical tube, with radial fins added in the inner part in order to decrease its conductance C_{inj} .

Figure 4.2 shows a standard and a finned injection tube.

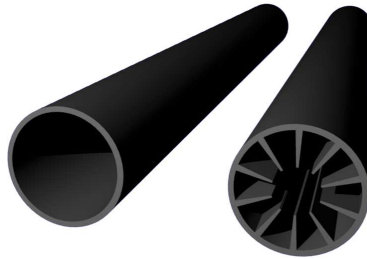


Figure 4.2: Standard injection tube (left) and finned injection tube (right).

The idea (see ref. [61]) behind this particular injection tube design is to reduce the conductance felt by the chaotic atoms that diffuse out from the cell, while (possibly) not affecting the intensity of the collimated beam transmitted by the injection tube to the cell. The

conductance of a generic tube of length L is inversely proportional to the inner perimeter s and directly proportional to the square area A of its cross section (see eq. 4.3, from [58]).

$$C = \frac{8}{3\sqrt{\pi}} \sqrt{2k_B \frac{T}{M}} \cdot \left(\frac{A^2}{sL} \right) \quad (4.3)$$

where k_B is the Boltzmann's constant ($1.38065 \cdot 10^{23} \text{ m}^2 \text{ kg s}^{-2} \text{ K}^{-1}$), T and M are the temperature and mass of the gas. Adding very thin fins, the inner perimeter is greatly increased, while the cross area (which influences also the transmitted collimated beam) is only slightly reduced.

In order to test the possible improvement in the target thickness induced by this kind of geometry, four injection tubes have been designed and realized in the mechanical workshop of Università di Ferrara, using the electro-erosion technique, starting from bulk aluminum. The transverse geometry of the four IT is presented in fig.4.3: all the tubes have an inner diameter of 10 mm and a length of 100 mm.

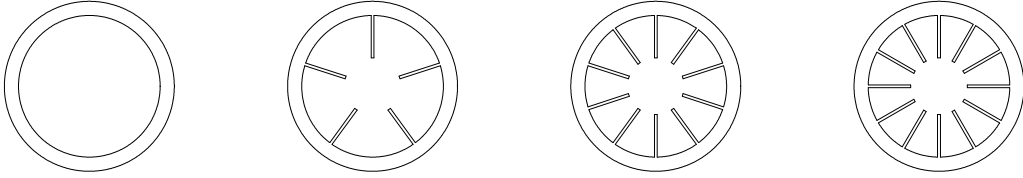


Figure 4.3: Injection tubes produced: 0, 5, 10, 12 fins.

The conductance of each tube has been measured separately, using the ABS2 setup described in chapter 2, section 2.3.

The standard storage cell was replaced by a compression volume connected to the exit of the injection tube (see for reference fig. 4.4 in next section). The pressure in the CV (called P_{CV}) is proportional to the flow Q of molecular hydrogen through the IT. Therefore the transmitted beam intensity I is expressed by eq. 4.4:

$$I = \frac{2}{k_B T} Q = \frac{2}{k_B T} P_{CV} C_{inj} \quad (4.4)$$

The '2' coefficient takes into account that, in the present case, atoms entering the CV recombine into molecules when they hit the inner walls of the compression volume (steel at room temperature), resulting in a detected intensity of half of the real atomic beam intensity entering the injection tube.

4.3 Measurements

4.3.1 Injection tube conductance

The first performed measurement was devoted to the determination of the injection tube conductance C_{inj} . For this purpose, the last part of the ABS was separated from the rest of the apparatus by means of a valve, and a calibrated gas injection system (see fig. 4.4) was connected to the compression volume. This system is able to provide a constant and calibrated flux of molecular hydrogen. As described in chapter 2 section 2.2, it is composed

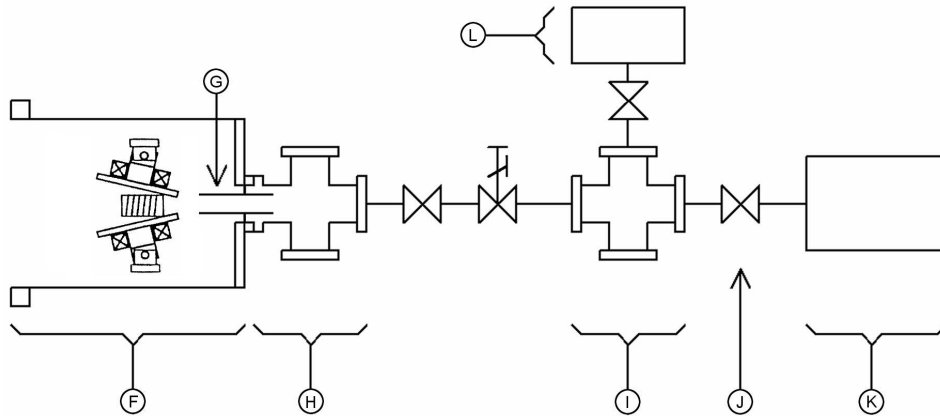


Figure 4.4: Calibrated gas injection system connected to the Compression Volume (H): (F) Chamber 5, (G) injection tube, (I) constant pressure volume (V_{cal}), (J)Regulating Valve, (K) Hydrogen gas buffer, (L) calibrated volume.

of a volume (V_{cal}), in which the pressure is kept constant by a regulating valve, driven by a PID controller that reads the actual pressure from a capacitive gauge. This volume is connected to the CV through an adjustable leak valve and a bellow. The flux supplied by the system depends therefore on the V_{cal} pressure and the opening of the leak valve. The measurement of C_{inj} has been performed by setting a fixed and known flow of molecular hydrogen through the injection tube and subsequently measuring the pressure P_{CV} . By measuring this pressure, the tube conductance can be calculated from the general equation $C_{inj} = Q/\Delta P$, where ΔP corresponds to the difference of pressure between the two ends of the injection tube. Since the pressure in the chamber is at least two orders of magnitude smaller than the pressure in compression volume $\Delta P \sim P_{CV}$, and the previous formula can be replaced by:

$$C_{inj} = Q/P_{CV} \quad (4.5)$$

The measurement has been repeated for the four different injection tubes. The main purpose of this measurement is to determine the difference between the four geometries, rather than expressing the conductances as absolute values. Therefore it results more convenient to express the conductance of the three injection tubes with fins relatively to the standard injection tube without fins. The results are presented in fig. 4.5

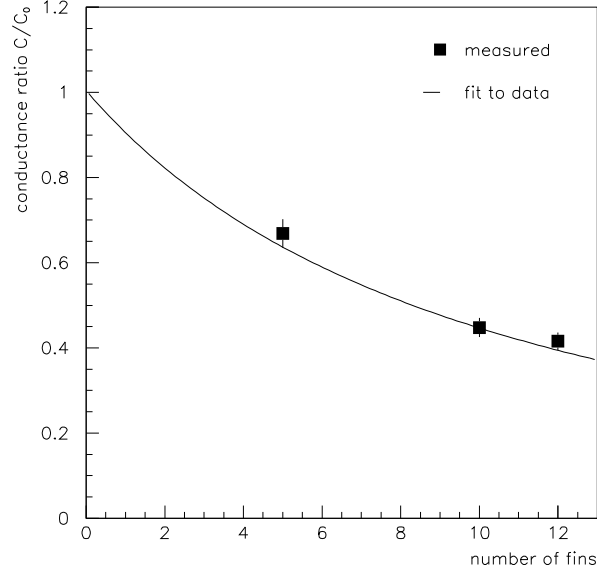


Figure 4.5: Measured (black squares) and calculated (line) conductance ratio as function of fins number. C_0 is the conductance in case of a tube without fins.

The choice of measuring the relative conductances instead of the absolute values leads also to an improvement in the precision of the measurement itself: the systematic error on the calibrated flux (5%) and the absolute precision of P_{CV} gauge (30%) cancel out in the ratio. The remaining reproducibility error has been estimated by repeating the measurement on the same injection tube (after removing and reinstalling it) and results to be 5% and is reported in the plot. In fig. 4.5 a fit to the measured data using the following equation (obtained from 4.3):

$$\frac{C}{C_0} = (76.4 \text{ cm}^{-2}) \frac{A^2}{sL} \left[c_1 + c_2 \frac{A}{sL} \right]^{-1} \quad (4.6)$$

is also reported. In equation 4.6 L is the length of the injection tube, d its diameter, A is the open area of the cross section of the injection tube and s its inner perimeter. For the case of a tube with n fins the last two quantities are:

$$A = \pi \frac{d^2}{4} - hln, \quad s = \pi d + 2ln \quad (4.7)$$

where d is the inner diameter of the tube and h and l are the thickness and length (in radial direction) of the fins. The two dimensionless parameters c_1 and c_2 are obtained from the fit to the experimental data and the result is: $c_1 = 0.75$, $c_2 = 30$. The coefficient 76.4 cm^{-2} has been chosen in order to obtain the normalization: $C/C_0 = 1$ for the case of no fins tube.

4.3.2 Atomic beam intensity

The intensity of the transmitted beam through the injection tube depends on the number and geometry of fins, since they partially obstruct the cross section of the tube. The intensity for each geometry has been determined using equation 4.4. If the conductance is expressed in l/s and the pressure in $mbar$, the resulting intensity will be in $atoms/s$.

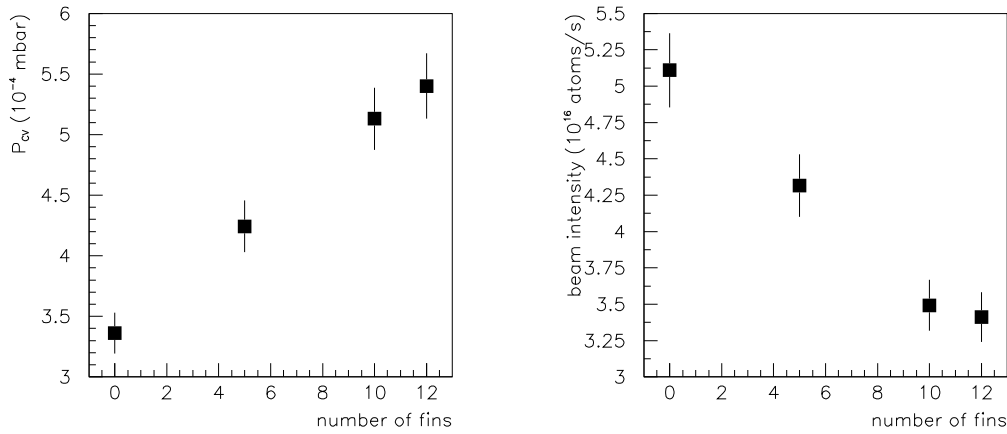


Figure 4.6: Left panel: measured P_{CV} in function of number of fins. Right panel: calculated transmitted beam intensity in function of number of fins.

In the left panel of fig. 4.6 the measured values of P_{CV} are displayed as a function of the number of fins. The indicated 5% error is related to the reproducibility of the ionization gauge used. From these data the corresponding beam intensity at the exit of the injection tube (the one inside the CV) for each tube geometry (see right panel of fig. 4.6) has been calculated. The 7% error is the sum in quadrature of the reproducibility of P_{CV} (5%) and systematic error on Q (5%).

4.4 Target thickness estimation

In order to prove whether this particular kind of injection tube can improve the target thickness, the measured conductance and intensity of transmitted beam have to be applied to a real storage cell geometry. The cell geometry used for this calculation is the present design for the future PAX storage cell: it consists in a beam tube whose cross section is a square of 10mm edge, a cylindrical injection tube of 10 mm inner diameter and 100 mm length and a sampling tube of 5 mm inner diameter and 100 mm length (see fig. 4.7).

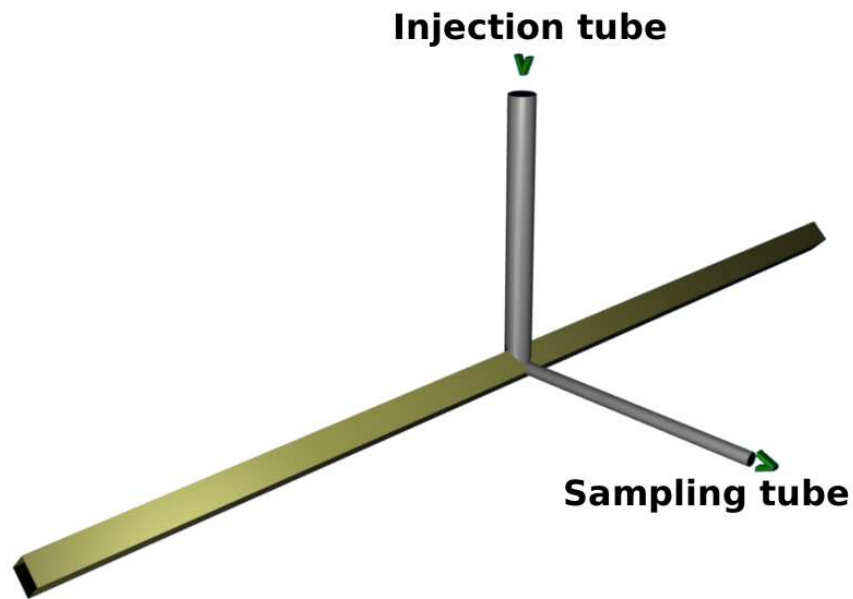


Figure 4.7: Present design for future PAX storage cell.

By using eq. 4.6 and data from fig. 4.6, it is possible to evaluate the contribution of different number and geometry of fins. The predicted target thickness for three types of fins, is presented in fig. 4.8.

As it can be deduced from the figure, the application of a finned tube to the PAX storage cell would produce only a slight increase in the target thickness. This is due to the not negligible beam intensity attenuation caused by the fins themselves (see right panel of fig. 4.6) and to the relatively low contribution of the injection tube (39%) to the total conductance of the cell. As result finned injection tubes are not useful for this particular storage cell geometry, but could be useful for different geometries.

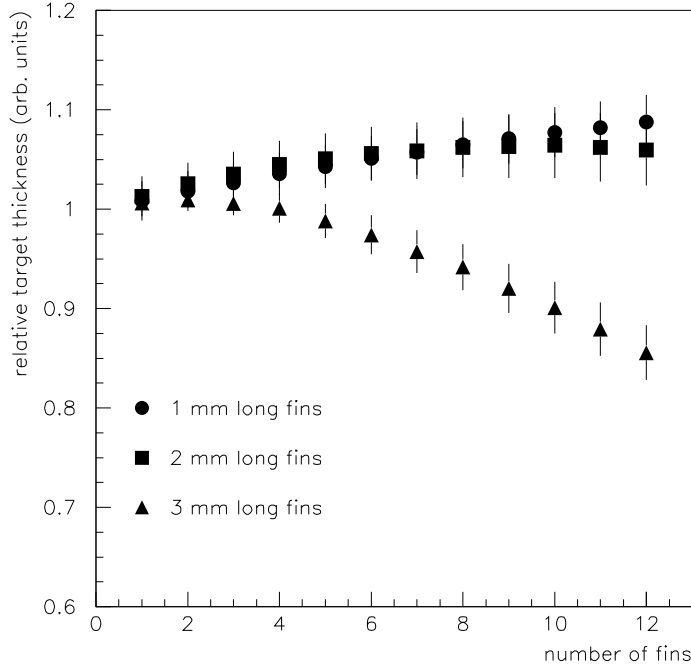


Figure 4.8: Estimated thickness for different fin length and number for the PAX cell geometry.

4.5 Comparison to simulations

The measured beam attenuation can be compared to the attenuation predicted using simulation software. Various software packages exist for this purpose, and they all are composed of two key parts: a *starting generator* and a *ray tracing* algorithm. While the ray tracing part is quite standard and similar in all the implementations, the starting generator is a more delicate part. It consists on an algorithm that creates, on a *starting surface*, the initial tracks (particles position and velocities). A track's origin is randomly chosen on this surface and its velocity is randomly chosen according to the measured beam velocity distribution. The present knowledge of the physical properties of beam formation is far from being complete: very little is known on what exactly happens after the particles exit the nozzle and before entering the magnet system, so it is quite difficult to decide which starting generator properties are the most suitable to properly simulate the real beam generation. For this reason different research groups have used different starting generators. The analysis of the data presented in this chapter can provide some important informations about the most appropriate starting generator for our ABS2.

The measured data were compared to the calculation obtained with a software library developed in Ferrara to project high intensity sources, called "SCAN". Since the ABS has a cylindrical symmetry, the starting surface chosen is a disc centered on the beam axis and perpendicular to it. The tracks origin is randomly chosen on this surface and its direction is randomly chosen in azimuthal angle ϕ from 0 to 2π and in θ from 0 to $\pi/2$, in order to

produce an isotropic distribution. Since the starting surface diameter is not known, three diameters (2, 3 and 4 mm) were chosen, and the corresponding track samples were generated. From each sample a sub-sample (called N_0) was extracted, consisting of tracks that would traverse a 0-fin tube; then for each of these three sub-samples the tracks evolution was followed in steps of $\Delta z = 0.5 \text{ mm}$, discarding tracks that correspond to an atom that hit a fin. The remaining tracks that survive after traversing the injection tube are called N . The survival fraction is therefore $S = N/N_0$ and is plotted (for all the three different starting surfaces used) in fig. 4.9: it is evident a strong correlation between the diameter of the starting surface used and the attenuation due to collisions with fins.

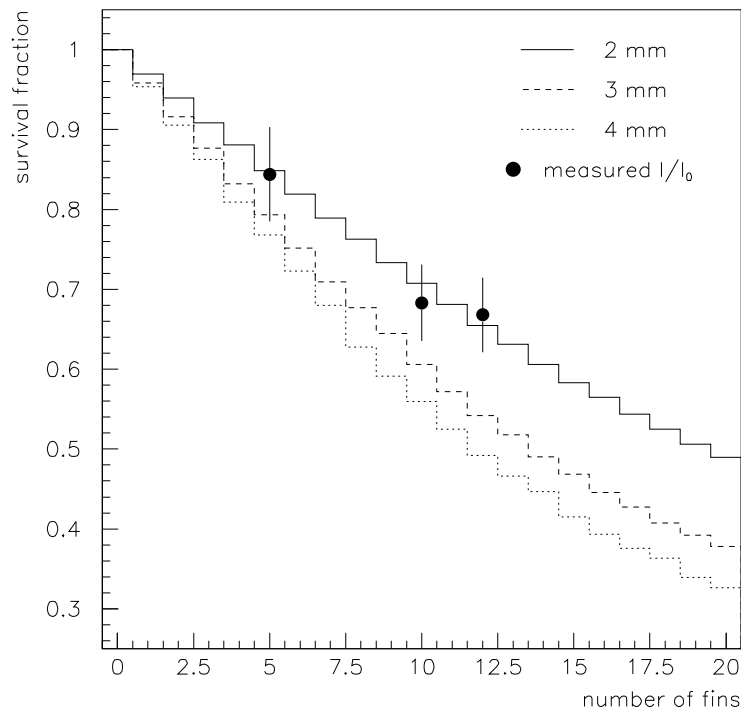


Figure 4.9: Survival fraction as a function of fins number: measured data and fits for different starting surfaces.

From fig. 4.9 is evident that the measured data fit the calculated attenuation in case of a 2 mm starting surface.

The position of the starting surface along the beam axis, instead, results in-influent from the nozzle exit to 3 cm downstream: no information about the z position of the starting surface can be obtained with this kind of measurements.

Supposing a collimated parallel beam in which all the particles velocities are almost parallel to beam axis (standard assumption up to now) the beam intensity attenuation measured is much stronger than the expected one. In order to explain such an intensity drop when

fins are added, it is necessary to consider the azimuthal velocity of beam particles not negligible. Considering a cylindrical coordinate system (ρ, ϕ, z) , where the z axis is coincident with the beam axis, ϕ is the azimuthal angle and ρ the distance from the beam axis, the z component of the angular momentum is $L_z = m\rho v_\phi$. The focusing force of the sextupolar magnetic system is radial and perpendicular to v_ϕ (azimuthal velocity), so L_z is not affected by the magnetic field. From this consideration a correlation between the starting generator used and v_ϕ can be induced: bigger diameter of the starting surface (and thus wider ρ distribution) give wider azimuthal velocities. Wider v_ϕ of particles imply higher probability that a particle collides with the radial fins and thus is removed from the collimated beam. This correlation is evident looking at the distribution of L_z presented in fig. 4.10: the top panel shows all trajectories, while the bottom panel shows only the trajectories that pass through a 10-fins tube.

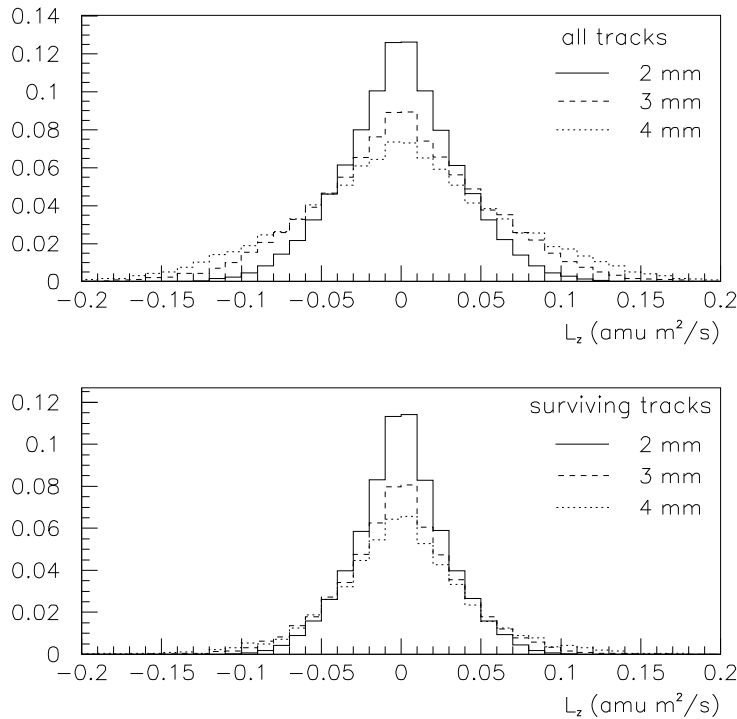


Figure 4.10: Distribution of L_z in case of no fins tube (top panel) and 10-fins tube (bottom panel). The three lines correspond to different starting surface diameters.

A finned injection tube selects the tracks with small azimuthal velocity component. Therefore the measured intensity attenuation provides interesting informations on the width of L_z distribution of the beam and also on the diameter of the most appropriate starting surface.

4.6 Conclusions

The performance of a *finned tube* (compared to standard hollow tubes) has been measured and the results have been applied to the real geometry of future PAX storage cell. The conclusion of the calculations is not encouraging for that particular geometry, but may be useful for different geometries. From the same experimental data new and unexpected results arise: the measured loss in transmitted beam intensity is a proof that atoms in the beam have a not negligible azimuthal velocity, that has to be taken into account in order to make accurate calculations. The calculated attenuation is directly correlated with the starting surface transverse diameter: from these measurements it is therefore possible to properly choose the most appropriate starting generator for our ABS2 system.

In the left panel the standard 2 mm *sonic* nozzle is shown, while the right panel depicts the *trumpet* nozzle. The *trumpet* nozzle has been produced in the mechanical workshop of Università di Ferrara, from a bulk cylinder of “anticorodal” aluminum, using a lathe. Its inner surface has been smoothed using alumina powder and subsequently cleaned with pure ethanol.

The experimental tests have been carried out on the ABS1 test bench described in chapter 2 section 2.1.

The Monte-Carlo calculations are discussed in the next section, where an example of the use of the SCAN program, in connection with the “starting surface” produced in the Monte-Carlo for the ABS2, is also shown.

Section 5.3 presents and discusses the measurements that, at present, are in agreement with the Monte-Carlo previsions.

5.2 Monte-Carlo simulations

The particle density involved in the expansion of an ABS molecular beam from the nozzle in the vacuum chambers is sufficiently low to allow a computational simulation, modelling a real gas with some thousands to millions of molecules. Velocity and position coordinates of these molecules are stored by the program DS2G in the computer and modified in time as the molecules are followed through collisions and boundary interactions in physical space. The program employs physical gas models which are described and validated in [57].

The flow in our case is an axially symmetric flow, whose longitudinal axis lies along the x axis and the y-coordinate is a radius perpendicular to that axis. The flow-field is divided into 10 four-sided regions, as can be seen in fig. 5.2), where the four sides are numbered from 1 to 4 in clockwise manner, as depicted in fig. 5.3. These sides are divided into a

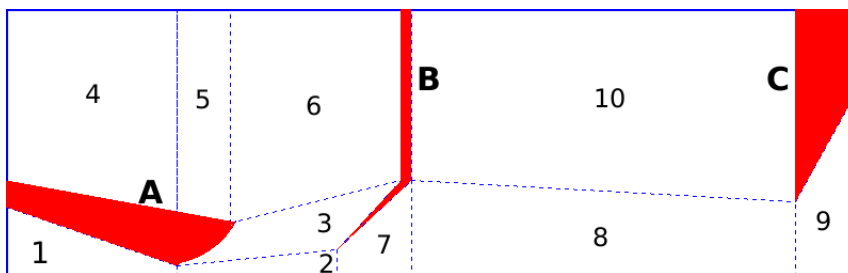


Figure 5.2: Simulation geometry. (A) nozzle, (B) skimmer, (C) collimator. Numbers indicate the simulation regions.

number of cell segments or elements and the number of elements on each side must be the same. The cell structure is defined by joining the corresponding points on each side of the region by straight lines and then dividing each of these lines into the same number of cell elements.

Side 2 and 4 must therefore be straight.

Figure 5.2 shows the geometry suggested and the “regions” used in the simulations.

For each of the two nozzle geometries, *sonic* and *trumpet*, three different distances nozzle-skimmer (see left table 5.1) and three different molecular hydrogen fluxes (see right table 5.1) have been simulated.

Table 5.1: Simulation parameters

Nozzle-skimmer		Fluxes	
label	distance [mm]	label	flux [sccm]
1	12.6	a	25
2	15.0	b	100
3	17.4	c	200

Besides the geometry for the flow-field, the simulation program needs additional inputs. The different steps necessary to prepare a simulation are listed below.

First of all the properties (viscosity, diameter, mass, etc.) of the gas to be simulated (in our case molecular hydrogen) have to be defined.

Then it is necessary to describe the position of gas flow source (*stream*), that in this case is the vertical left segment of region ‘1’ in fig. 5.2 and its density and velocity (see table 5.2 columns 4 and 5). With these data the program creates a gas source.

As a last step all the boundaries of the flow-field (represented as blue solid lines in fig. 5.2) have to be defined. In the simulation they consist in the interface to vacuum chambers, and therefore they have been set to source/sink with a constant gas density, defined by the measured pressures in ABS1.

One additional step useful for decreasing the simulation time required to reach the steady conditions is to set an initial gas density for regions 2 to 9, instead of starting from vacuum. In our case after few days steady conditions are reached and the simulation can be stopped.

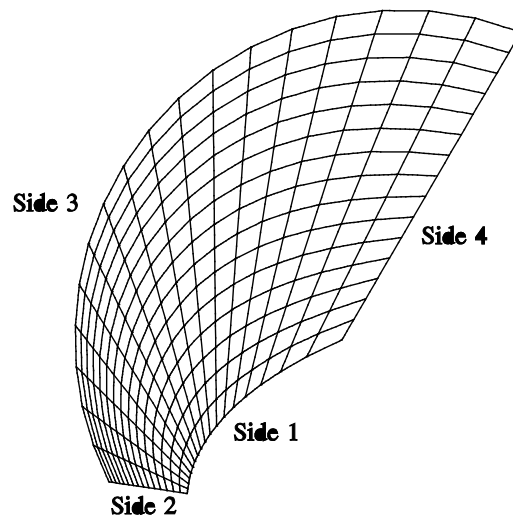


Figure 5.3: Scheme of a flow-field region.

The list of the main input data supplied to the software DS2G are presented in table 5.2 columns 4 to 7.

Table 5.2: Monte-Carlo input data

simulation name	noz-skim distance [mm]	nozzle flux [sccm]	stream density [m-3]	stream velocity [m/s]	Chamber 1 density [m-3]	Chamber 2 density [m-3]
sonic1a	12.6	25	9.18E+21	29.0	3.03E+18	1.49E+17
sonic1b	12.6	100	3.67E+22	29.0	1.21E+19	5.96E+17
sonic1c	12.6	200	7.34E+33	29.0	2.42E+19	1.19E+18
sonic2a	15.0	25	9.18E+21	29.0	3.13E+18	1.04E+17
sonic2b	15.0	100	3.67E+22	29.0	1.25E+19	4.15E+17
sonic2c	15.0	200	7.34E+33	29.0	2.50E+19	8.30E+17
sonic3a	17.4	25	9.18E+21	29.0	3.18E+18	7.73E+16
sonic3b	17.4	100	3.67E+22	29.0	1.27E+19	3.09E+17
sonic3c	17.4	200	7.34E+33	29.0	2.55E+19	6.19E+17
trumpet1a	12.6	25	9.18E+21	29.0	2.96E+18	2.09E+17
trumpet1b	12.6	100	3.67E+22	29.0	1.19E+19	8.37E+17
trumpet1c	12.6	200	7.34E+33	29.0	2.37E+19	1.67E+18
trumpet2a	15.0	25	9.18E+21	29.0	3.10E+18	1.39E+17
trumpet2b	15.0	100	3.67E+22	29.0	1.24E+19	5.55E+17
trumpet2c	15.0	200	7.34E+33	29.0	2.48E+19	1.11E+18
trumpet3a	17.4	25	9.18E+21	29.0	3.17E+18	1.02E+17
trumpet3b	17.4	100	3.67E+22	29.0	1.27E+19	4.07E+17
trumpet3c	17.4	200	7.34E+33	29.0	2.54E+19	8.14E+17

The output from the simulation software program DS2G are the fluxes, in [*particles/s*], between the different regions and a *dump* file, in which the program saves all the tracks informations, concerning particles that are contained in the “dump surface”. In our case the “dump surface” has been chosen coincident with the aperture of the collimator (see fig. 5.2) that is the entrance of the magnetic focusing system. The relevant fluxes for our simulation are listed in table 5.3.

In the first column the simulation names are listed. In the second and third column the nozzle-skimmer distances and the nozzle flux are reported.

In the sixth column “Nozzle flow” the molecular flows that exit the nozzle, resulting from the difference of out-coming flow (column 4) and backward flow (column 5) are listed.

In the seventh and eighth columns, “Skimmer” and “Collimator” the simulated fluxes of molecules through the skimmer and collimator (see fig. 5.2) are listed.

From the configurations of fluxes and distances, an increase of the skimmer and collimator fluxes results evident, when a *trumpet* nozzle is used instead of a standard *sonic* nozzle.

The difference is more evident in table 5.4, which shows the ratio between the skimmer and collimator fluxes for a *trumpet* and *sonic* nozzle for all the possible configurations.

An increase of about 60% for skimmer flux and 40% for collimator flux is expected. The

Table 5.3: Monte-Carlo Simulations data

simulation name	noz-skim [mm]	flux [sccm]	(1 \Rightarrow 2)	(2 \Rightarrow 1)	Nozzle flow (1 $>$ 2)-(2 $>$ 1)	Skimmer (2 \Rightarrow 7)	Collimator (8 \Rightarrow 9)
sonic1a	12.6	25	1.05E+19	2.59E+17	1.019E+19	7.752E+17	1.603E+17
sonic1b	12.6	100	4.22E+19	2.03E+18	4.015E+19	3.111E+18	6.087E+17
sonic1c	12.6	200	8.45E+19	4.75E+18	7.980E+19	5.981E+18	1.067E+18
sonic2a	15.0	25	1.05E+19	2.51E+17	1.026E+19	5.572E+17	1.471E+17
sonic2b	15.0	100	4.49E+19	2.15E+18	4.277E+19	2.355E+18	5.777E+17
sonic2c	15.0	200	8.48E+19	4.69E+18	8.014E+19	4.246E+18	9.150E+17
sonic3a	17.4	25	1.05E+19	2.40E+17	1.025E+19	4.131E+17	1.332E+17
sonic3b	17.4	100	4.22E+19	1.94E+18	4.031E+19	1.654E+18	4.905E+17
sonic3c	17.4	200	8.47E+19	4.62E+18	8.013E+19	3.134E+18	8.305E+17
trumpet1a	12.6	25	1.07E+19	1.13E+18	9.609E+18	1.195E+18	2.147E+17
trumpet1b	12.6	100	4.29E+19	4.35E+18	3.855E+19	5.170E+18	8.407E+17
trumpet1c	12.6	200	8.57E+19	8.38E+18	7.735E+19	1.070E+19	1.572E+18
trumpet2a	15.0	25	1.07E+19	1.12E+18	9.542E+18	8.344E+17	1.940E+17
trumpet2b	15.0	100	4.29E+19	4.37E+18	3.854E+19	3.621E+18	7.563E+17
trumpet2c	15.0	200	8.51E+19	8.33E+18	7.681E+19	7.464E+18	1.376E+18
trumpet3a	17.4	25	1.07E+19	1.12E+18	9.567E+18	6.153E+17	1.782E+17
trumpet3b	17.4	100	4.29E+19	4.37E+18	3.854E+19	2.650E+18	6.769E+17
trumpet3c	17.4	200	8.55E+19	8.37E+18	7.716E+19	5.474E+18	1.225E+18

best solution among the simulated one seems to be “trumpet2c”, which presents a nozzle-skimmer distance of 15 *mm* and an hydrogen flux of 200 *sccm*.

Table 5.4: Ratio of simulated fluxes

ratio of	Nozzle flow ratio (1 \rightarrow 2)(2 \rightarrow 1)	Skimmer ratio (2 \rightarrow 7)	Collimator ratio (8 \rightarrow 9)
trumpet1a/sonic1a	0.943	1.541	1.340
trumpet1b/sonic1b	0.960	1.662	1.381
trumpet1c/sonic1c	0.969	1.789	1.473
trumpet2a/sonic2a	0.930	1.497	1.319
trumpet2b/sonic2b	0.901	1.537	1.309
trumpet2c/sonic2c	0.958	1.758	1.503
trumpet3a/sonic3a	0.933	1.489	1.339
trumpet3b/sonic3b	0.956	1.602	1.380
trumpet3c/sonic3c	0.963	1.746	1.475

From the second column of table 5.4 it is also evident that the nozzle net fluxes for the *trumpet* geometry are slightly smaller than the one for the *sonic* nozzle. This is probably due to the higher backward flux from region 2 to region 1, as evident from column 4 of

table 5.3.

An example of gas number density in the flowfield region is presented in fig. 5.4.

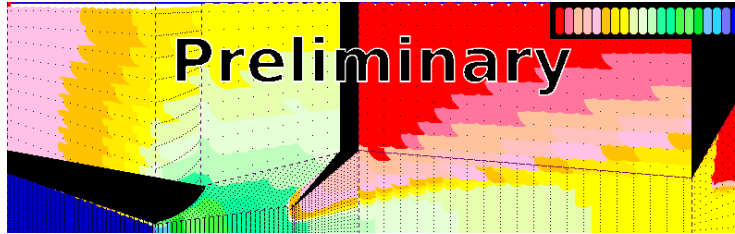


Figure 5.4: Gas number density obtained from the output of DS2G (simulation “trumpet2b”).

The Monte Carlo simulation program produces a binary file called DGMOF1.DAT that contains all the tracks on the “dump surface” at the time when the simulation was stopped. From this file it is possible to extract the tracks direction on the “starting surface” that can be used on the program “SCAN” (see section 4.5 of chapter 4) that allows to follow the particles motion up to the end of the magnetic system. In this way it is possible to judge if the tracks can be focused and evaluate the expected intensity at the focal point, at the end of the magnetic system, where the *injection tube* to the cell is located (see chapter 4).

The file-format is different for the two programs; the DS2G output has to be converted to a suitable input file for SCAN. This is accomplished with the Fortran program, reported in Appendix C. It reads the binary file generated by the simulation program and produces a file that can be loaded by SCAN as a “starting surface”.

The obtained results are promising: a double intensity injected in the storage cell is expected, when using a *trumpet* nozzle instead of a *sonic* nozzle:

Table 5.5: SCAN results

simulation name	intensity [at/s]
sonic2b	$5.60 \cdot 10^{16}$
trumpet2b	$1.09 \cdot 10^{17}$

5.3 Measurements

The results of the simulation motivated the construction of a real *trumpet* nozzle (see fig. 5.1), that has been tested on the ABS1 apparatus, described in chapter 2 section 2.1. The measurements consisted in evaluating the difference in beam intensity, measured by Chamber 2 and CV, and beam density, measured by the QMA, when a *trumpet* nozzle is used instead of the standard *sonic* nozzle.

The measurements have been repeated for the six different dissociator hydrogen fluxes, listed in table 5.6, and three different nozzle-skimmer distances, listed in table 5.7.

Table 5.6: Hydrogen fluxes

Hydrogen flux [sccm]
25 - 50 - 100 - 150 - 200 - 237.5

Table 5.7: Nozz-skim distances

label	distance [mm]
1	12.6
2	15.0
3	17.4

5.3.1 Procedure for data-taking

All the data were taken after the system had reached stable conditions. The fixed parameters for all the measurements are listed in table 5.8 (a drawing of the dissociator can be found in fig. 2.2 of chapter 2). For each hydrogen flux in the dissociator, listed in table

Table 5.8: Fixed parameters

Collar heater	135 K
Nozzle temperature	75 K

5.6, the procedures for QMA measurement and CV measurement have been applied, as described in the following two sections. The data are shown and discussed in section 5.3.2. Additional useful informations have been collected from Chamber 2 pressure P_{HV2} in a parasitic way, as may be seen below and in section 5.3.2.

QMA measurement

After setting the hydrogen flux to 25 *sccm*, ABS1 was let stabilize until all the measured values of temperatures, pressures and QMA signals were stable. The initial conditions were recorded, then the flux was increased according to the values reported in table 5.6. After 5 minutes, enough to reach stable conditions, new data were recorded and the flux was increased again.

The signal from the spectrometer (QMA) and the measured hydrogen flux are the relevant informations on which this measurement is based.

After recording the data corresponding to the highest hydrogen flux (237.5 *sccm*), the flux was set back to the starting value of 25 *sccm*. In this case, since the change in flux is much higher then the previous ones, the new data were recorded after 10 minutes instead of 5 minutes.

This last set of data corresponding to once more the minimum flux is useful to cross-check the stability and reproducibility of the ABS1.

The measurement took about 35 minutes.

CV measurement

The hydrogen flux was already set to 25 *sccm* from the previous measurement, so the ABS1 had already reached stable conditions.

The Compression Volume valve V_{CV} was closed and after 5 minutes the initial conditions were recorded.

The *flag* was then moved to the “ON” position¹ in order to record the background of Chamber 2 in CV. After 5 minutes the new data were recorded and the flux of hydrogen was increased according to table 5.6.

After additional 5 minutes the new data were recorded and the *flag* was put back to the “OFF” position.

In this measurement the relevant signals are the pressure in the CV volume (P_{CV}) and the hydrogen flux ($H2$).

Also for this case, after recording the data corresponding to the highest hydrogen flux, the flux was set back to the starting value, in order to check the stability and reproducibility of the apparatus.

The measurement took about 70 minutes.

Chamber 2 measurement

Chamber 2 (see chapter 2) can be used as a big compression volume. It is pumped by two turbo pumps, whose pumping speed is constant. Only a small fraction (less than 1%) of the beam that passes through the skimmer, exits Chamber 2 and reaches the diagnostic system.

The pressure in Chamber 2 (P_{HV2}) is therefore directly proportional to the skimmer flux Q_{sk} , through the following equation:

$$Q_{sk} = P_{HV2} \cdot S \quad (5.1)$$

where S is the total pumping speed of the two turbomolecular pumps.

This measurement was done in a parasitic way as it did not require any special procedure: $H2$ and P_{HV2} , were continuously monitored by the DAQ system.

Nozzle change

After completing the measurements for the first nozzle-skimmer distance, the distance itself was changed, according to table 5.7 and the QMA measurement and CV measurement were repeated.

Upon completing the measurements for all the three nozzle-skimmer distances, the *sonic* nozzle was replaced by the *trumpet* one, following these steps:

- Vacuum-insulation of diagnostic system from ABS1 and warming-up of the nozzle and collar to room temperature.

¹ON means flag on the axis of the beam, in order to block the beam and prevent it from entering the CV; OFF means off axis, so that the beam can pass through and reach the CV.

- Venting of ABS1 (Chamber 1 and 2) with N_2 .
- Removing of the installed nozzle.
- Installation of the new nozzle (checking that the distance nozzle-skimmer is correct).
- Restart of the ABS1 pumps.
- Absolute calibration the P_{HV2} and P_{CV} gauges, by using a baratron.

In order to check the reproducibility of the nozzle exchange procedure, each nozzle was installed twice, according to the following chronological list:

- Install *sonic* nozzle and measure.
- Install *trumpet* nozzle and measure.
- Install *sonic* nozzle and measure.
- Install *trumpet* nozzle and measure.

5.3.2 Data analysis and results

Chamber 2

The data collected have been analyzed using *root* programs.

The first data to be analyzed was the pressure in Chamber 2: figure 5.5 plots P_{HV2} as function of the hydrogen flux through the dissociator; the transition points have been removed with the same algorithm discussed in chapter 3 and the remaining point fitted. The slope given by the fit has been recorded, as P_{HV2} is proportional to the skimmer flux shown in fig.5.5.

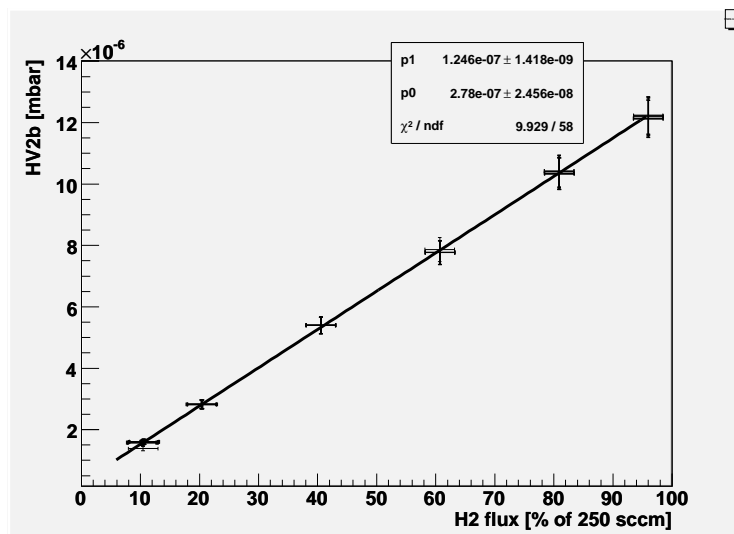


Figure 5.5: Result of root analysis for Chamber 2 data. Pressure HV2b is plotted as a function of the hydrogen flux through the nozzle.

This slope represents the skimmer flux normalized to the input dissociator flux. The results of this procedure, repeated for all the nozzle positions are reported in fig. 5.6. The

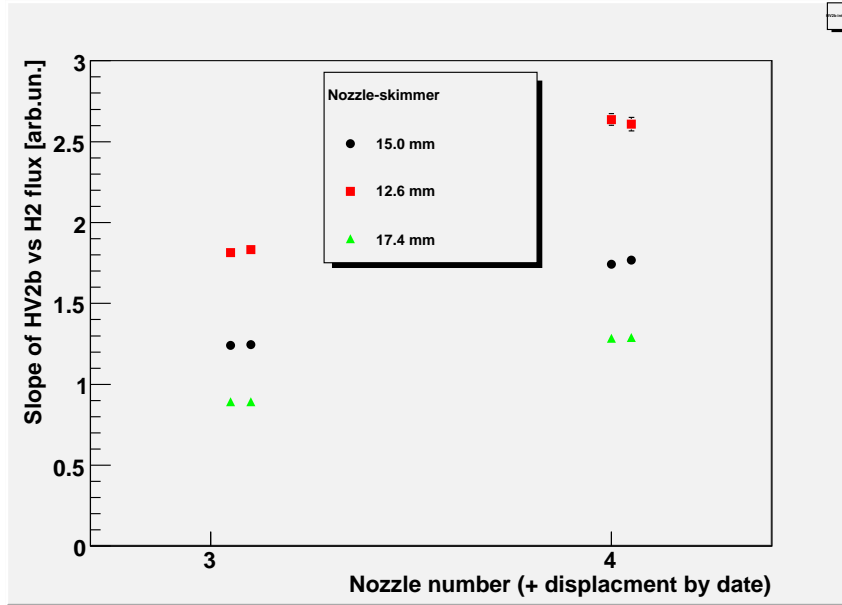


Figure 5.6: Chamber 2 fluxes comparison. Label ‘3’ corresponds to *sonic* nozzle data, label ‘4’ to *trumpet* nozzle data.

x-axis of fig. 5.6 represents the nozzle type (‘3’ means *sonic* and ‘4’ means *trumpet*). The y-axis is the flux through the skimmer, normalized to the dissociator hydrogen flux H_2 .

Two series of data have been collected for each nozzle.

The different shape and color of the points correspond to the different distances nozzle-skimmer, according to the figure legend.

The errors are usually not visible since they are smaller than the dimensions of the marks. Two important informations can be derived from fig. 5.6.

First, by comparing the same nozzle type, position and flux the very good reproducibility of the data corresponding to subsequent re-installation of the nozzle is evident.

The second important conclusion is that comparing the two nozzles, for the same nozzle-skimmer distance, *trumpet* nozzle presents an increase in intensity with respect to a *sonic* nozzle.

Quadrupole Mass Analyzer

The data obtained with the Quadrupole Mass Analyzer are presented in fig. 5.7.

From the plot it emerges that the measurement reproducibility is not consistent with the calculated errors. Therefore, even if there is a hint that the *trumpet* nozzle improves beam density measured by the QMA, these data are not conclusive and further investigation to improve the reproducibility of the system seem necessary.

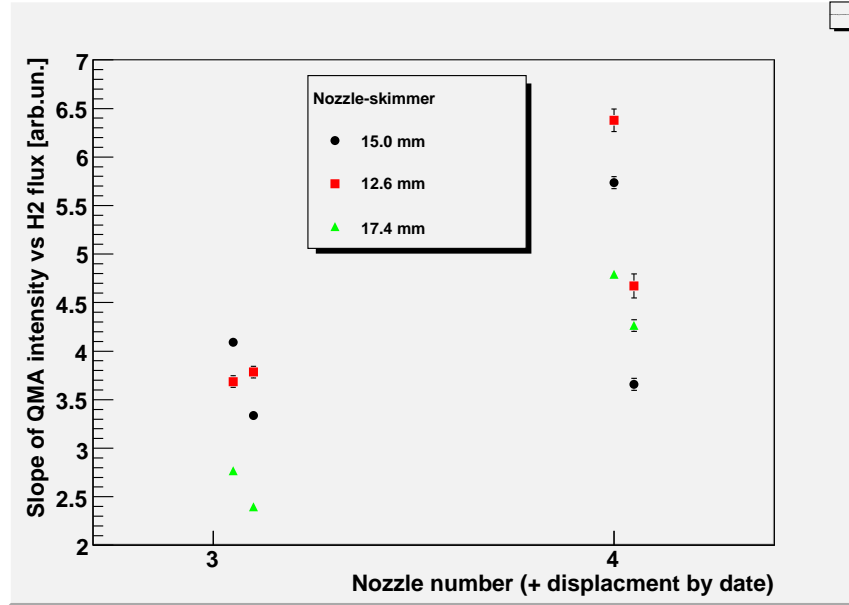


Figure 5.7: QMA density comparison. Label ‘3’ corresponds to *sonic* nozzle, label ‘4’ to *trumpet* nozzle.

Compression volume

The analysis of compression volume data consists in measuring the difference (ΔP_{CV}) between the pressure measured in the CV with flag “ON” and “OFF” (see footnote of sec. 5.3.1). This difference is proportional to the incoming beam intensity I_{CV} , according to equation:

$$I_{CV} = \frac{1}{k_B T} \cdot \Delta P_{CV} \cdot C_{CT} \quad (5.2)$$

where C_{CT} is the conductance of the compression tube connected with CV (see also chapter 4).

The beam intensity measured by the CV is not the “real” intensity at the nozzle as the beam, traversing Chamber 2, is attenuated due to *rest gas* (see chapter 3).

It is therefore necessary to correct the measured beam intensity for attenuation. The correction is performed using the following equation (derived from eq. 3.1 of chapter 3, section 3.1.2):

$$I_0 = I \exp \left[\frac{A_I P L}{k_B T_{RG}} \right] \quad (5.3)$$

The results have been corrected for Chamber 2 attenuation and are presented in fig. 5.8. The x-axis of fig. 5.8 is the same as previous fig. 5.6. The beam intensity measured by Compression Volume, normalized to the nozzle input flux, is reported in the y-axis.

In this case the reproducibility of the system, after subsequent re-installation of the same nozzle is consistent with the calculated errors.

Comparing data for the two nozzle geometries, for the same skimmer distance, it is clearly visible an increase in CV intensity, consistent with the measurement of P_{HV2} .

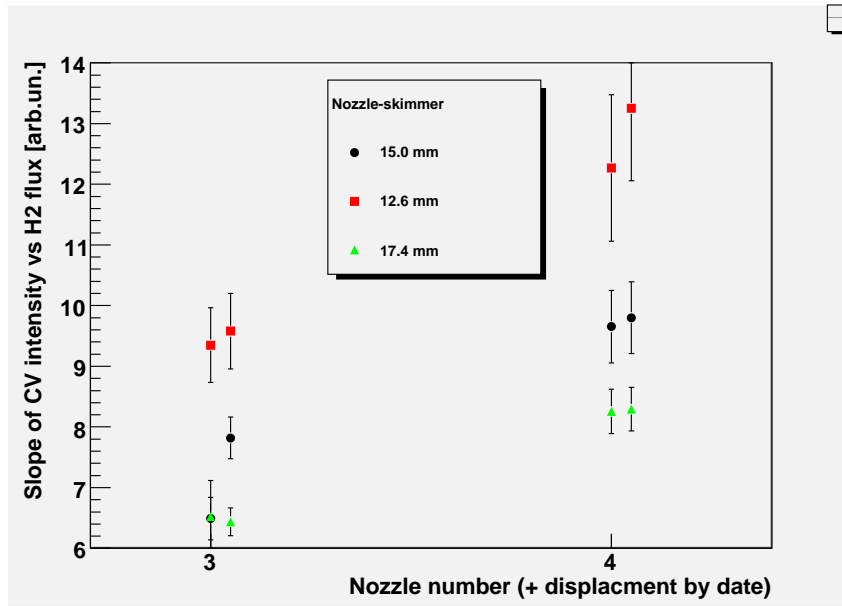


Figure 5.8: Chamber 2 fluxes comparison. Label ‘3’ corresponds to *sonic* nozzle, label ‘4’ to *trumpet* nozzle. Data are corrected for beam attenuation in Chamber 2.

5.4 Conclusions

The data presented in fig. 5.6 evidence an increase in skimmer flux of more than 40% when the standard *sonic* nozzle is replaced by a *trumpet* nozzle. The experimental results are smaller than the calculations, which foresee an increase of about 60%, but it still represents a promising result.

The collimator flux obtained with the Monte-Carlo cannot be compared with the experimental result, since in the used apparatus (ABS1) such a collimator is not present. It is instead possible to measure the intensity of the beam that enters the compression volume: from fig. 5.8 it is evident that *trumpet* nozzle geometry give an increase in measured intensity of about 30%.

Furthermore simulations of the trajectories of the particles starting from the dump surface through the magnetic field to the focal point have been carried out with the program “SCAN” and the results are favorable.

In conclusion the experimental tests on this particular nozzle geometry, carried out on the ABS1 in SpinLab give very promising results and suggest further investigation on the possibility to use a *trumpet* nozzle in order to improve the intensity of an Atomic Beam Source.

Appendix A

Atomic Beam Sources magnetic system

A multi-polar magnetic system is used in Atomic Beam Sources (ABS) to focus hydrogen/deuterium atomic beams. The resulting magnetic field gradient produces a Stern-Gerlach spin separation, providing focusing of the $+1/2 m_j$ electronic spin state and defocusing of the $-1/2$ spin state.

The ABS magnetic system has three main functions: accept large fraction of the atoms from the divergent beam, transport the largest part of them to the target region and to deflect out of the beam axis the unwanted spin states.

The Stern-Gerlach spin separation affects electron spin polarization, while the required polarization is in nuclear spin. In order to obtain it, two techniques can be used: spin-transitions by means of radio-frequency or electron polarization transfer to the nuclei, using a weak magnetic field. In this way it is possible to obtain a nuclear-polarized atomic beam of hydrogen or deuterium.

The most used magnetic systems are composed of multiple discrete magnets, which are axially symmetric in order to obtain a large acceptance and thus produce higher focused beam intensity. Multiple sections design, instead of a single long bulky magnet, is chosen in order to improve pumping speed, by providing pumping gaps. In this way background gas density inside magnets can be decreased and therefore the beam attenuation due to rest gas scattering can be lowered.

Each section is composed of single segments, joined together to form a multi-polar magnet: in this case the pole tip field is almost independent of the bore and is of the order of $2 T$ for permanent magnets, $1 T$ for normal conducting magnets and $4 T$ for super-conducting ones.

For the standard geometry used, the beam solid angle accepted at the magnetic system entrance is proportional to the magnetic field strength B_m at the largest usable radius of the magnet (“pole tip”)[56]. Therefore higher flux of particles can be obtained with stronger magnetic fields.

High poles number would be preferred because it would give higher acceptance at the same value of the magnetic field, but in practice only *quadrupoles* and *sextupoles* are used, since it is difficult to maintain the same B_m for higher-polarity magnets. The most used are *sextupoles*, because of their additional harmonic focusing field. This kind of multi-pole magnets produce a magnetic field whose strength B depends only on the distance r from

the magnetic axis, as reported in the following equation:

$$B(r) = B_m \left(\frac{r}{r_m} \right)^2 \quad (\text{A.1})$$

where B_m is the field at the pole-tip position r_m .

The potential energy W of an atom, with dipole moment μ , inside a magnetic field B is:

$$W = \mu B \quad (\text{A.2})$$

and thus the force of the magnetic field on the atom is radial.

If the magnetic moment of the atom is approximated to the Bohr magneton μ_B , the atoms travelling inside a *sextupole* magnet experience a harmonic oscillator potential that is attractive (toward the axis) for $+1/2$ electronic spin state and repulsive for $-1/2$.

Considering a magnet with a cylindrical bore of radius r_m (see fig. A.1) and a point-like source of atoms located on the magnetic axis, atoms entering the magnet with an angle smaller than α_m will make harmonic oscillations about the axis with an amplitude $< r_m$ without hitting the pole pieces. The resulting magnet acceptance solid angle is $\Delta\Omega = \pi\alpha_m^2$,

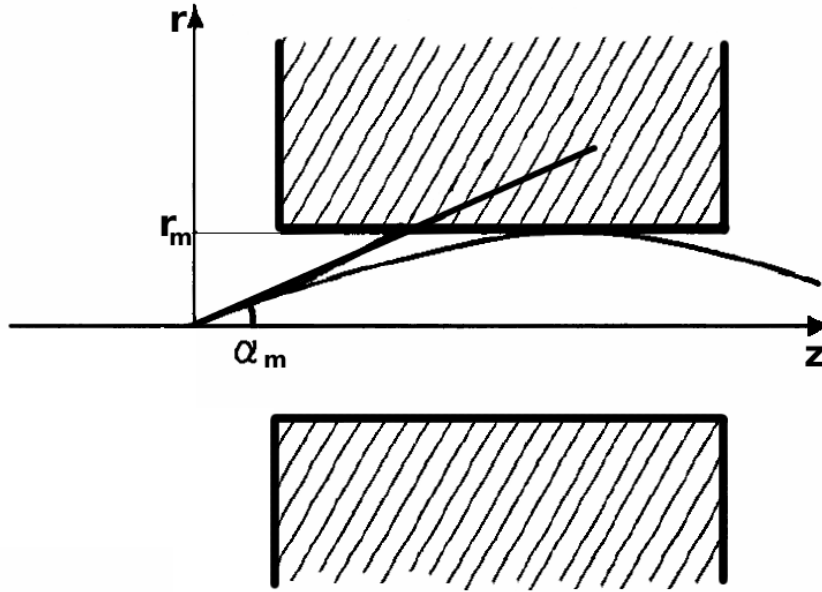


Figure A.1: Atom inside a sextupolar magnet. The indicated trajectory corresponds to the maximum accepted angle α_m . The beam axis is coincident with the magnetic axis (z).

which, averaged over the velocity distribution of the beam, becomes [55]:

$$\Delta\Omega = \pi\mu_b \frac{B_m}{k_B T} \quad (\text{A.3})$$

where T is the temperature of the source and k_B is the Boltzmann constant. It is evident that the acceptance angle increases with increasing pole-tip magnetic field and with lower beam temperature, but does not depend on the magnet diameter and length.

As an example for a magnet producing $B_m = 1 \text{ T}$ and a source at a temperature of $T = 100 \text{ K}$, the acceptance solid angle is $\alpha_m = 80 \text{ mrad}$ and $\Delta\Omega = 0.02 \text{ sr}$. Unfortunately

it is not possible to decrease beam temperature beyond a certain limit, because at low beam temperature the rest gas attenuation increases, resulting in a decreased beam intensity. As a result common temperatures used for beam sources are 65 to 80 K.

The effect of the velocity spread of beam particles (“chromatic aberration”) can be reduced using tapered inner diameter and by arranging the magnets in two groups, separated by a drift space.

The best geometry used for producing *sextupoles* is the result of calculations that take into account both theoretical aspects (geometry of the beam, geometry of the magnets, magnetic field etc.) and also empirical data such as the measured velocity distribution of atomic beam, the dissociation degree and rest gas attenuation.

Appendix B

Beer law

Both the ABS beam and the residual gas can be considered very diluted gas systems, where the collisions are most likely to be binary collisions, defined as collision in which there is no interchange between translational and internal energy. As a result of the collision, the velocity of the beam particle will be changed and the particle removed from the beam, resulting in beam attenuation.

Under this hypothesis the attenuation law can be deduced in the following way. Consider an atomic or molecular *monochromatic* beam emanating from an effusive source and moving through a rarefied gas, called *rest gas* or *residual gas*, in equilibrium in the space, at constant temperature and pressure. Interactions between beam and rarefied gas are assumed to be totally elastic and it is supposed that every collision removes the particle from the beam.

The infinitesimal number of collisions in the volume dV in the time dt is:

$$dm = g\sigma_{tot}n_1n_2dVdt \quad (\text{B.1})$$

where σ_{tot} is the cross section, n_1 is the number density of the beam (in [*particles/m³*]), n_2 is the number density of the residual gas, g is the relative velocity of beam and residual gas, in the hypothesis that all the beam particles have the same velocity \vec{v}_b and are uniformly distributed over a transverse beam surface S .

The infinitesimal variation of the number density of the beam is:

$$\frac{dn_1}{dt} = -\frac{dm}{dV} = -g\sigma_{tot}n_1n_2 \quad (\text{B.2})$$

If the beam particles travels a path dl in the time dt ,

$$\frac{dn_1}{dt} \cdot \frac{dl}{dl} = \frac{dn_1}{dl} \cdot v_b = -g\sigma_{tot}n_1n_2 \quad (\text{B.3})$$

the linear change in the beam number density with the path dl is:

$$\frac{dn_1}{dl} = -\frac{g}{v_b}\sigma_{tot}n_1n_2$$

From the previous equation it is easily obtained:

$$\frac{dn_1}{n_1} = -\frac{g}{v_b}\sigma_{tot}n_2dl \quad (\text{B.4})$$

Integrating over the path of the beam in the residual gas:

$$\int_0^L \frac{dn_1}{n_1} = \ln(n_1) = -\frac{g}{v_b} \sigma_{tot} \int_0^L n_2 dl + const \quad (\text{B.5})$$

with $const = \ln(n_0)$, where n_0 is the initial beam number density at time $t = 0$ and $l = 0$. It is possible to consider the residual gas a perfect gas and apply the law of the perfect gas to n_2 :

$$n_2 = \frac{N}{V} = \frac{P}{k_B T} \quad (\text{B.6})$$

where N is the total number of particles of the residual gas, V is the volume, P is the pressure and T the temperature.

We have therefore

$$\ln(n_1) = -\frac{g}{v_b} \cdot \frac{1}{k_B T} \int_0^L P dl + const \quad (\text{B.7})$$

The number density of the beam after it has travelled the length L is therefore:

$$n_1(L) = n_0 \exp \left[-\frac{g \sigma_{tot}}{v_b k_B T} \right] \int_0^L P dl \quad (\text{B.8})$$

If P is assumed constant over the distance L , we obtain:

$$n_1(L) = n_0 \exp \left[-\frac{g \sigma_{tot}}{v_b} \cdot \frac{1}{k_B T} \right] PL \quad (\text{B.9})$$

In our condition the quantity

$$\frac{g}{v_b} \sigma_{tot}$$

is a constant, with the dimension of an area (or a cross section): it is often called “*effective cross section*” σ_{eff} (see for instance ref. [59]) and the total cross section σ_{tot} is assumed independent from g .

This definition is exact if we assume a monochromatic beam, which means that all the particles in the beam have the same v_b at every instant and they are uniformly distributed on the transverse section of the beam. Although not fully realistic, these assumptions suggest a valid model to treat the realistic case.

In fact, in general, the attenuation of a diluted beam of particles of initial intensity I_0 [*particles/sec*] travelling a path of length L through a gas of known temperature T_{RG} and pressure P , is given by the Beer’s law, as can be found in the book of ref. [58]:

$$I = I_0 \exp \left[-\frac{A_I}{k_B T_{RG}} \int_0^L P dl \right] \quad (\text{B.10})$$

where I is the attenuated beam intensity, A_I is the attenuation coefficient, P and T_{RG} are

the rest gas pressure and temperature and k_B is the Boltzmann constant. For the case of constant gas pressure equation B.10 can be simplified as follows:

$$I = I_0 \exp \left[-\frac{A_I PL}{k_B T_{RG}} \right] \left[\frac{\text{particles}}{\text{sec}} \right] \quad (\text{B.11})$$

It is convenient to relate the attenuation to the “beam number density” n (particles per unit of volume, $[m^{-3}]$). The “number density” n of a beam with a velocity distribution function $f(v)$ is given by:

$$n = \int n f(v) dv \left[\frac{\text{particles}}{m^3} \right] \quad (\text{B.12})$$

For a monochromatic beam the velocity distribution corresponds to a δ Dirac function:

$$f(v) = \delta(v - \bar{v}) \quad (\text{B.13})$$

where \bar{v} is the mean velocity of the beam. Assuming a uniform beam density over its cross area S , the intensity of the beam can be related to the number density by the following equation:

$$I = S \int_S n f(v) v dv = S n \bar{v} \quad (\text{B.14})$$

Eq. B.11 can therefore be written in terms of density n as:

$$n = n_0 \exp \left[-\frac{A_n PL}{k_B T_{RG}} \right] \quad (\text{B.15})$$

where A_n is the same as A_I in the case of a monochromatic beam.

As explained in chapter 2 the spectrometer (QMA) can measure A_n , while a compression volume measure A_I .

In the real case, however, the beam velocity distribution is far from being a *delta* function: its FWHM is about 30% of its mean velocity. Both attenuation coefficients depend on the total cross section and on the velocity distribution, as expressed by the following equations:

$$A_n = \frac{\int f(v_b) \sigma_{eff}(v_b) dv_b}{\int f(v_b) dv_b} \quad (\text{B.16})$$

$$A_I = \frac{\int v_b f(v_b) \sigma_{eff}(v_b) dv_b}{\int v_b f(v_b) dv_b} \quad (\text{B.17})$$

where v_b is the velocity of a beam particle, $f(v_b)$ is the velocity distribution of beam particles, σ_{eff} is the effective cross section.

According to [58], the definition of the effective cross section σ_{eff} is:

$$\sigma_{eff} = \int f(v_b) \sigma_{tot}(v_b) dv_b \quad (\text{B.18})$$

The density of the residual gas in the vacuum chamber can be considered constant and the effective cross section σ_{eff} can be expressed by:

$$\sigma_{eff}(v_b) = \int f(\vec{v}_{RG}) \sigma_{tot}(\vec{g}) \frac{g}{v_b} d\vec{v}_{RG} \quad (\text{B.19})$$

where $\vec{g} = \vec{v}_b - \vec{v}_{RG}$ is the vectorial relative velocity between the beam particle and the rest gas. A geometrical representation of \vec{g} is given in fig. B.1.

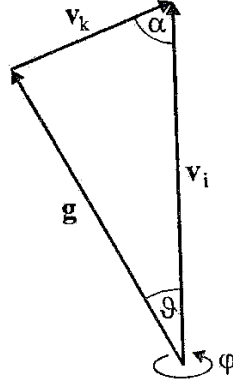


Figure B.1: Relative velocity between beam particle and RG.

$\sigma_{tot}(\vec{g})$ is the total cross section for a relative velocity \vec{g} and the function $f(\vec{v}_{RG})$ is the Maxwellian velocity distribution of the RG:

$$f(\vec{v}_{RG}) = \frac{4}{\sqrt{\pi}} \left(\frac{m}{2k_b T} \right)^{3/2} v_{RG}^2 \exp \left[-\frac{m v_{RG}^2}{2k_b T} \right] \quad (\text{B.20})$$

Equation B.19 can be simplified by making use of the following considerations:

- the total cross section is independent from the direction of motion of the particles, therefore $\sigma_{tot}(\vec{g}) = \sigma_{tot}(g)$
- the vectorial velocity of RG particles can be written in the form $v_{RG}^2 = v_b^2 + g^2 - 2v_b g \cos \theta$;

On the basis of these considerations, equation B.19 can be integrated over θ . The result is ([58], p.41):

$$\sigma_{eff}(v_b) = \frac{1}{v_{mp}} \int_0^\infty \sigma_{tot}(g) \frac{g}{v_b} f(g, v_b) dg \quad (\text{B.21})$$

where v_{mp} is the most probable Maxwellian velocity ($\sqrt{2k_b T/m}$). The function $f(g, v_b)$ is the distribution of relative velocities expressed by the following formula([58], p.42):

$$f(g, v_b) = \frac{2}{\sqrt{\pi}} \frac{g}{v_b} \exp \left[-\frac{g^2 + v_b^2}{v_{mp}^2} \right] \sinh \left[\frac{2g v_b}{v_{mp}^2} \right] \quad (\text{B.22})$$

Equation B.21 can be used to calculate the total σ_{eff} , that results to be the integral of $\sigma_{eff}(v_b)$ weighted with $f(v_b)$, with the following formula:

$$\sigma_{eff} = \frac{\int \sigma_{eff}(v_b) f(v_b) dv_b}{\int f(v_b) dv_b} \quad (\text{B.23})$$

where $\sigma_{eff}(v_b)$ is given by the formula B.21.

Appendix C

Files for trumpet nozzle simulation program DS2G

C.1 read_1000.f

```

    program readv2
    implicit none
    integer i,j,k
    integer reclen,nmol,nrec
    character*100 filename
    C nmol is the input parameter to DSMC "Number of mols per record"
    parameter(nmol=1000)
    integer il
    real r1
    real time1,time2
    C pos(1,i) is z ; pos(2,i) is r ; vel(1,i) is z comp ; vel(2,i) is r
    C   vel(3,i) is azim ; vel(4,i) has to do with rotational energy
    real pos(2,nmol),vel(4,nmol)
    integer species(nmol)

    filename='filein.dat'
    C Record Length is determined by DSMC program's write statements
    reclen=4*(4+7*nmol)
    C Some arbitrarily large value for nrec
    nrec=5000000

    open(98,file='atoms.dat')
    open(99,file='molecules.dat')

    open(11,file=filename,form='unformatted',
    &   access='direct',recl=reclen)

```

10

20

```

C Skip the first record because it's always empty
  do j=2,nrec
    write(6,*)"record ",j
C***** 30
C Details of record structure
C
C i1 should be 1 for axially symmetric flows
C r1 is FNUM(NR)*MUF*WFMAX(1)
*—FNUM is the number of real molecules represented by each simulated
* molecule in region NR
*—MUF is the molecule multiplication factor
!—WFMAX(1) is the maximum weighting factor
!—TIMI(1) is the time at which the molecule sample started for the record
!—A is the time at which it ended) 40
C*****

    read(11,rec=j,err=999)i1,r1,pos,vel,species,time1,time2
    write(6,*)time1,time2
    do i=1,nmol
      if (species(i).eq.2) then
        write(98,1000)pos(2,i),vel(1,i),vel(2,i),vel(3,i)
      else
        write(99,1000)pos(2,i),vel(1,i),vel(2,i),vel(3,i)
      endif
    enddo
  enddo
1000 format(4(e12.6,1x))
999 continue
close(98)
close(99)
close(11)

stop
end 60

```

C.2 DS2GD-trumpet2b.TXT

The data was generated by Version 3. 2
 The flow is axially symmetric
 A time average is made after the assumed establishment of steady flow
 There are no radial weighting factors
 The basic ratio of the number of real mols. rep. by each sim. mol. is 0.200000E+11
 The basic time step is 0.100000E-06
 The gas is a custom specification
 The number of regions is 10
 The number of species is 2
 Mean values are used for cross-collision data 10
 The number of species groups is 1
 There are 1 chemical reactions
 The number of associated third-body probability tables is 1
 The following data is for species 1
 The reference diameter is 0.350000E-09
 This is at the reference temperature 273.000
 The viscosity-temperature power law is 0.670000
 The reciprocal of the VSS scattering param. is 1.35000
 The molecular mass is 0.334000E-26
 The species is in group number 1 20
 The number of rotational degrees of freedom is 2
 The rotational coll. number is temperature independent
 The rotational and vibrational data is independent of other species
 The rotational collision number is 350.000
 Vibration is not taken into account
 The following data is for species 2
 The reference diameter is 0.350000E-09
 This is at the reference temperature 273.000
 The viscosity-temperature power law is 0.670000
 The reciprocal of the VSS scattering param. is 1.35000 30
 The molecular mass is 0.334000E-26
 The species is in group number 1
 The number of rotational degrees of freedom is 2
 The rotational coll. number is temperature independent
 The rotational and vibrational data is independent of other species
 The rotational collision number is 350.000
 Vibration is not taken into account
 The following data is for reaction 1
 Species code of one molecule is 1
 Species code of the other molecule is 1 40
 The reaction is a recombination
 The post-recombination species code 2
 The species code of the third-body is 1
 The number of contributing internal degrees of freedom 0.000000
 The activation energy 0.000000
 1.E10 times the pre-exponential parameter 1.00000
 The temperature exponent in the rate equation 0.000000
 The energy of the reaction 0.000000
 The following data is for third-body probability 1
 That for species 1 is 0.000000 50
 That for species 2 is 0.000000
 There is a stream or initial gas
 The number of molecule input files is 0
 The number of molecule output files is 1
 The stream temperature is 300.000
 The stream number density is 0.367000E+23
 The velocity component in the x direction is 29.0000
 The velocity component in the y direction is 0.000000
 The initial flowfield is specified for each region

```

Fraction of species      1 in the stream is      1.00000
Fraction of species      2 in the stream is      0.00000
The initial gas is set region by region
Region      1 initially has :-
  a temperature of      0.000000
  a number density of    0.000000
  an x velocity component of    0.000000
  a y velocity component of    0.000000
  a fraction      0.000000 of species      1
  a fraction      0.000000 of species      2
Region      2 initially has :-
  a temperature of      300.000
  a number density of    0.124000E+20
  an x velocity component of    0.000000
  a y velocity component of    0.000000
  a fraction      0.000000 of species      1
  a fraction      1.000000 of species      2
Region      3 initially has :-
  a temperature of      300.000
  a number density of    0.124000E+20
  an x velocity component of    0.000000
  a y velocity component of    0.000000
  a fraction      0.000000 of species      1
  a fraction      1.000000 of species      2
Region      4 initially has :-
  a temperature of      300.000
  a number density of    0.124000E+20
  an x velocity component of    0.000000
  a y velocity component of    0.000000
  a fraction      0.000000 of species      1
  a fraction      1.000000 of species      2
Region      5 initially has :-
  a temperature of      300.000
  a number density of    0.124000E+20
  an x velocity component of    0.000000
  a y velocity component of    0.000000
  a fraction      0.000000 of species      1
  a fraction      1.000000 of species      2
Region      6 initially has :-
  a temperature of      300.000
  a number density of    0.124000E+20
  an x velocity component of    0.000000
  a y velocity component of    0.000000
  a fraction      0.000000 of species      1
  a fraction      1.000000 of species      2
Region      7 initially has :-
  a temperature of      300.000
  a number density of    0.555000E+18
  an x velocity component of    0.000000
  a y velocity component of    0.000000
  a fraction      0.000000 of species      1
  a fraction      1.000000 of species      2
Region      8 initially has :-
  a temperature of      300.000
  a number density of    0.555000E+18
  an x velocity component of    0.000000
  a y velocity component of    0.000000
  a fraction      0.000000 of species      1
  a fraction      1.000000 of species      2
Region      9 initially has :-
  a temperature of      300.000

```

```

a number density of      0.555000E+18
an x velocity component of      0.000000
a y velocity component of      0.000000
a fraction      0.000000      of species      1
a fraction      1.00000      of species      2
Region      10      initially has :-
a temperature of      300.000
a number density of      0.555000E+18
an x velocity component of      0.000000
a y velocity component of      0.000000
a fraction      0.000000      of species      1
a fraction      1.00000      of species      2
The following data is for region      1
Ratio of FNUM and DTM to the basic values are      1.00000
The number of cell segments along sides 1 and 3 is      32
The number of cell segments along sides 1 and 3 is      20
Side 1 is straight and the endpoints are specified
Side 3 is straight and the endpoints are specified
The segments along side 2 are of equal length
The segments along side 4 are of equal length
The division of the intermediate lines joining sides1 and 3 is weighted by      1.00000
The x coord. of the startpoint on side 1 is      -0.310000E-01
The y coord. of the startpoint on side 1 is      0.000000
The x coord. of the endpoint on side 1 is      -0.150000E-01
The y coord. of the endpoint on side 1 is      0.000000
The size ratio of cell at side 4 to that at side 2 is      1.00000
The x coord. of the startpoint on side 3 is      -0.310000E-01
The y coord. of the startpoint on side 3 is      0.650000E-02
The x coord. of the endpoint on side 3 is      -0.150000E-01
The y coord. of the endpoint on side 3 is      0.100000E-02
The size ratio of cell at side 4 to that at side 2 is      1.00000
The following data is for side      1
The side is an axis
The following data is for side      2
The side is a stream boundary
The following data is for side      3
The side is a solid surface
Conditions are constant along the side
The following data is for the whole side
The following data is for species      1
The surface temperature is      100.000
The reflection is diffuse
The fraction of molecules that are adsorbed is      0.000000
The in-plane surface velocity is      0.000000
The normal-to-plane surface velocity is      0.000000
The catalytic fraction is      0.000000
The following data is for species      2
The surface temperature is      100.000
The reflection is diffuse
The fraction of molecules that are adsorbed is      0.000000
The in-plane surface velocity is      0.000000
The normal-to-plane surface velocity is      0.000000
The catalytic fraction is      0.000000
The following data is for side      4
The side is an interface with other regions
The number of adjoining sides is      1
The following data is for matching side      1
The code of the side is      2
and it is in region      2
The x displacement to side is      0.000000
The y displacement to side is      0.000000

```

The following data is for region 2
 Ratio of FNUM and DTM to the basic values are 1.00000
 The number of cell segments along sides 1 and 3 is 30
 The number of cell segments along sides 1 and 3 is 20
 Side 1 is straight and the endpoints are specified
 Side 3 is straight and the endpoints are specified
 The segments along side 2 are of equal length
 The segments along side 4 are of equal length
 The division of the intermediate lines joining sides1 and 3 is weighted by 1.00000 190
 The x coord. of the startpoint on side 1 is $-0.150000E-01$
 The y coord. of the startpoint on side 1 is 0.000000
 The x coord. of the endpoint on side 1 is 0.000000
 The y coord. of the endpoint on side 1 is 0.000000
 The size ratio of cell at side 4 to that at side 2 is 1.00000
 The x coord. of the startpoint on side 3 is $-0.150000E-01$
 The y coord. of the startpoint on side 3 is $0.100000E-02$
 The x coord. of the endpoint on side 3 is 0.000000
 The y coord. of the endpoint on side 3 is $0.300000E-02$
 The size ratio of cell at side 4 to that at side 2 is 1.00000 200
 The following data is for side 1
 The side is an axis
 The following data is for side 2
 The side is an interface with other regions
 The number of adjoining sides is 1
 The following data is for matching side 1
 The code of the side is 4
 and it is in region 1
 The x displacement to side is 0.000000
 The y displacement to side is 0.000000 210
 The following data is for side 3
 The side is an interface with other regions
 The number of adjoining sides is 1
 The following data is for matching side 1
 The code of the side is 4
 and it is in region 3
 The x displacement to side is 0.000000
 The y displacement to side is 0.000000
 The following data is for side 4
 The side is an interface with other regions 220
 The number of adjoining sides is 1
 The following data is for matching side 1
 The code of the side is 2
 and it is in region 7
 The x displacement to side is 0.000000
 The y displacement to side is 0.000000
 The following data is for region 3
 Ratio of FNUM and DTM to the basic values are 1.00000
 The number of cell segments along sides 1 and 3 is 20
 The number of cell segments along sides 1 and 3 is 20 230
 Side 1 is a segment of a conic surface
 Side 3 is straight and the endpoints are specified
 The segments along side 2 are of equal length
 The segments along side 4 are of equal length
 The division of the intermediate lines joining sides1 and 3 is weighted by 1.00000
 The x coord. of the focus is $-0.190000E-01$
 The y coord. of the focus is $0.107000E-01$
 The parameter p is $0.104924E-01$
 The eccentricity is 0.000000
 The angle from x dirn. to side 2 corner is 5.72503 240
 The angle from x dirn. to side 4 corner is 5.10351
 The size ratio of cell at side 4 to that at side 2 is 1.00000


```

The x coord. of the startpoint on side 3 is      0.600000E-02
The y coord. of the startpoint on side 3 is      0.900000E-02
The x coord. of the endpoint on side 3 is        0.000000
The y coord. of the endpoint on side 3 is        0.300000E-02
The size ratio of cell at side 4 to that at side 2 is 1.00000
The following data is for side                    1
The side is a solid surface
Conditions are constant along the side                                250
The following data is for the whole side
The following data is for species                    1
The surface temperature is      100.000
The reflection is diffuse
The fraction of molecules that are adsorbed is      0.000000
The in-plane surface velocity is    0.000000
The normal-to-plane surface velocity is    0.000000
The catalytic fraction is      0.000000
The following data is for species                    2
The surface temperature is      100.000                                260
The reflection is diffuse
The fraction of molecules that are adsorbed is      0.000000
The in-plane surface velocity is    0.000000
The normal-to-plane surface velocity is    0.000000
The catalytic fraction is      0.000000
The following data is for side                    2
The side is an interface with other regions
The number of adjoining sides is          1
The following data is for matching side          1
The code of the side is                    1                                270
and it is in region                          6
The x displacement to side is    0.000000
The y displacement to side is    0.000000
The following data is for side                    3
The side is a solid surface
Conditions are constant along the side
The following data is for the whole side
The following data is for species                    1
The surface temperature is      300.000
The reflection is diffuse                                280
The fraction of molecules that are adsorbed is      0.000000
The in-plane surface velocity is    0.000000
The normal-to-plane surface velocity is    0.000000
The catalytic fraction is      0.500000
The following data is for species                    2
The surface temperature is      300.000
The reflection is diffuse
The fraction of molecules that are adsorbed is      0.000000
The in-plane surface velocity is    0.000000
The normal-to-plane surface velocity is    0.000000                                290
The catalytic fraction is      0.000000
The following data is for side                    4
The side is an interface with other regions
The number of adjoining sides is          1
The following data is for matching side          1
The code of the side is                    3
and it is in region                          2
The x displacement to side is    0.000000
The y displacement to side is    0.000000
The following data is for region                    4                                300
Ratio of FNUM and DTM to the basic values are 1.00000
The number of cell segments along sides 1 and 3 is 20
The number of cell segments along sides 1 and 3 is 10

```

Side 1 is straight and the endpoints are specified
 Side 3 is straight and the endpoints are specified
 The segments along side 2 are of equal length
 The segments along side 4 are of equal length
 The division of the intermediate lines joining sides1 and 3 is weighted by 1.00000
 The x coord. of the startpoint on side 1 is -0.310000E-01
 The y coord. of the startpoint on side 1 is 0.800000E-02 310
 The x coord. of the endpoint on side 1 is -0.150000E-01
 The y coord. of the endpoint on side 1 is 0.100000E-02
 The size ratio of cell at side 4 to that at side 2 is 1.00000
 The x coord. of the startpoint on side 3 is -0.310000E-01
 The y coord. of the startpoint on side 3 is 0.250000E-01
 The x coord. of the endpoint on side 3 is -0.150000E-01
 The y coord. of the endpoint on side 3 is 0.250000E-01
 The size ratio of cell at side 4 to that at side 2 is 1.00000
 The following data is for side 1
 The side is a solid surface 320
 Conditions are constant along the side
 The following data is for the whole side
 The following data is for species 1
 The surface temperature is 100.000
 The reflection is diffuse
 The fraction of molecules that are adsorbed is 0.000000
 The in-plane surface velocity is 0.000000
 The normal-to-plane surface velocity is 0.000000
 The catalytic fraction is 0.500000
 The following data is for species 2 330
 The surface temperature is 100.000
 The reflection is diffuse
 The fraction of molecules that are adsorbed is 0.000000
 The in-plane surface velocity is 0.000000
 The normal-to-plane surface velocity is 0.000000
 The catalytic fraction is 0.000000
 The following data is for side 2
 The side is a stream boundary
 Conditions are constant along the side
 The following data is for the whole side 340
 The velocity comp. in the x direction is 0.000000
 The velocity comp. in the y direction is 0.000000
 The temperature is 300.000
 The number density is 0.124000E+20
 The fraction of species 1 is 0.000000
 The fraction of species 2 is 1.00000
 The following data is for side 3
 The side is a stream boundary
 Conditions are constant along the side
 The following data is for the whole side 350
 The velocity comp. in the x direction is 0.000000
 The velocity comp. in the y direction is 0.000000
 The temperature is 300.000
 The number density is 0.124000E+20
 The fraction of species 1 is 0.000000
 The fraction of species 2 is 1.00000
 The following data is for side 4
 The side is an interface with other regions
 The number of adjoining sides is 1
 The following data is for matching side 1 360
 The code of the side is 2
 and it is in region 5
 The x displacement to side is 0.000000
 The y displacement to side is 0.000000

The following data is for region 5
 Ratio of FNUM and DTM to the basic values are 1.00000
 The number of cell segments along sides 1 and 3 is 20
 The number of cell segments along sides 1 and 3 is 10
 Side 1 is a segment of a conic surface
 Side 3 is straight and the endpoints are specified 370
 The segments along side 2 are of equal length
 The segments along side 4 are of equal length
 The division of the intermediate lines joining sides 1 and 3 is weighted by 1.00000
 The x coord. of the focus is $-0.190000E-01$
 The y coord. of the focus is $0.107000E-01$
 The parameter p is $0.104924E-01$
 The eccentricity is 0.000000
 The angle from x dirn. to side 2 corner is 5.10351
 The angle from x dirn. to side 4 corner is 5.72503
 The size ratio of cell at side 4 to that at side 2 is 1.00000 380
 The x coord. of the startpoint on side 3 is $-0.150000E-01$
 The y coord. of the startpoint on side 3 is $0.250000E-01$
 The x coord. of the endpoint on side 3 is $-0.100000E-01$
 The y coord. of the endpoint on side 3 is $0.250000E-01$
 The size ratio of cell at side 4 to that at side 2 is 1.00000
 The following data is for side 1
 The side is a solid surface
 Conditions are constant along the side
 The following data is for the whole side
 The following data is for species 1 390
 The surface temperature is 100.000
 The reflection is diffuse
 The fraction of molecules that are adsorbed is 0.000000
 The in-plane surface velocity is 0.000000
 The normal-to-plane surface velocity is 0.000000
 The catalytic fraction is 0.500000
 The following data is for species 2
 The surface temperature is 100.000
 The reflection is diffuse
 The fraction of molecules that are adsorbed is 0.000000 400
 The in-plane surface velocity is 0.000000
 The normal-to-plane surface velocity is 0.000000
 The catalytic fraction is 0.000000
 The following data is for side 2
 The side is an interface with other regions
 The number of adjoining sides is 1
 The following data is for matching side 1
 The code of the side is 4
 and it is in region 4
 The x displacement to side is 0.000000 410
 The y displacement to side is 0.000000
 The following data is for side 3
 The side is a stream boundary
 Conditions are constant along the side
 The following data is for the whole side
 The velocity comp. in the x direction is 0.000000
 The velocity comp. in the y direction is 0.000000
 The temperature is 300.000
 The number density is $0.124000E+20$
 The fraction of species 1 is 0.000000 420
 The fraction of species 2 is 1.00000
 The following data is for side 4
 The side is an interface with other regions
 The number of adjoining sides is 1
 The following data is for matching side 1

The code of the side is 2
 and it is in region 6
 The x displacement to side is 0.000000
 The y displacement to side is 0.000000
 The following data is for region 6 430
 Ratio of FNUM and DTM to the basic values are 1.00000
 The number of cell segments along sides 1 and 3 is 10
 The number of cell segments along sides 1 and 3 is 10
 Side 1 is straight and the endpoints are specified
 Side 3 is straight and the endpoints are specified
 The segments along side 2 are of equal length
 The segments along side 4 are of equal length
 The division of the intermediate lines joining sides 1 and 3 is weighted by 1.00000
 The x coord. of the startpoint on side 1 is $-0.101000E-01$
 The y coord. of the startpoint on side 1 is $0.514302E-02$ 440
 The x coord. of the endpoint on side 1 is $0.600000E-02$
 The y coord. of the endpoint on side 1 is $0.900000E-02$
 The size ratio of cell at side 4 to that at side 2 is 1.00000
 The x coord. of the startpoint on side 3 is $-0.100000E-01$
 The y coord. of the startpoint on side 3 is $0.250000E-01$
 The x coord. of the endpoint on side 3 is $0.600000E-02$
 The y coord. of the endpoint on side 3 is $0.250000E-01$
 The size ratio of cell at side 4 to that at side 2 is 1.00000
 The following data is for side 1
 The side is an interface with other regions 450
 The number of adjoining sides is 1
 The following data is for matching side 1
 The code of the side is 2
 and it is in region 3
 The x displacement to side is 0.000000
 The y displacement to side is 0.000000
 The following data is for side 2
 The side is an interface with other regions
 The number of adjoining sides is 1
 The following data is for matching side 1 460
 The code of the side is 4
 and it is in region 5
 The x displacement to side is 0.000000
 The y displacement to side is 0.000000
 The following data is for side 3
 The side is a stream boundary
 Conditions are constant along the side
 The following data is for the whole side
 The velocity comp. in the x direction is 0.000000
 The velocity comp. in the y direction is 0.000000 470
 The temperature is 300.000
 The number density is $0.124000E+20$
 The fraction of species 1 is 0.000000
 The fraction of species 2 is 1.00000
 The following data is for side 4
 The side is a solid surface
 Conditions are constant along the side
 The following data is for the whole side
 The following data is for species 1
 The surface temperature is 300.000 480
 The reflection is diffuse
 The fraction of molecules that are adsorbed is 0.000000
 The in-plane surface velocity is 0.000000
 The normal-to-plane surface velocity is 0.000000
 The catalytic fraction is 0.500000
 The following data is for species 2

```

The surface temperature is      300.000
The reflection is diffuse
The fraction of molecules that are adsorbed is      0.000000
The in-plane surface velocity is      0.000000      490
The normal-to-plane surface velocity is      0.000000
The catalytic fraction is      0.000000
The following data is for region      7
Ratio of FNUM and DTM to the basic values are      1.00000
The number of cell segments along sides 1 and 3 is      20
The number of cell segments along sides 1 and 3 is      20
Side 1 is straight and the endpoints are specified
Side 3 is straight and the endpoints are specified
The segments along side 2 are of equal length
The segments along side 4 are of equal length      500
The division of the intermediate lines joining sides1 and 3 is weighted by      1.00000
The x coord. of the startpoint on side 1 is      0.000000
The y coord. of the startpoint on side 1 is      0.000000
The x coord. of the endpoint on side 1 is      0.700000E-02
The y coord. of the endpoint on side 1 is      0.000000
The size ratio of cell at side 4 to that at side 2 is      1.00000
The x coord. of the startpoint on side 3 is      0.000000
The y coord. of the startpoint on side 3 is      0.300000E-02
The x coord. of the endpoint on side 3 is      0.700000E-02
The y coord. of the endpoint on side 3 is      0.900000E-02      510
The size ratio of cell at side 4 to that at side 2 is      1.00000
The following data is for side      1
The side is an axis
The following data is for side      2
The side is an interface with other regions
The number of adjoining sides is      1
The following data is for matching side      1
The code of the side is      4
and it is in region      2
The x displacement to side is      0.000000      520
The y displacement to side is      0.000000
The following data is for side      3
The side is a solid surface
Conditions are constant along the side
The following data is for the whole side
The following data is for species      1
The surface temperature is      300.000
The reflection is diffuse
The fraction of molecules that are adsorbed is      0.000000
The in-plane surface velocity is      0.000000      530
The normal-to-plane surface velocity is      0.000000
The catalytic fraction is      0.500000
The following data is for species      2
The surface temperature is      300.000
The reflection is diffuse
The fraction of molecules that are adsorbed is      0.000000
The in-plane surface velocity is      0.000000
The normal-to-plane surface velocity is      0.000000
The catalytic fraction is      0.000000
The following data is for side      4      540
The side is an interface with other regions
The number of adjoining sides is      1
The following data is for matching side      1
The code of the side is      2
and it is in region      8
The x displacement to side is      0.000000
The y displacement to side is      0.000000

```

The following data is for region 8
Ratio of FNUM and DTM to the basic values are 1.00000
The number of cell segments along sides 1 and 3 is 20 550
The number of cell segments along sides 1 and 3 is 20
Side 1 is straight and the endpoints are specified
Side 3 is straight and the endpoints are specified
The segments along side 2 are of equal length
The segments along side 4 are of equal length
The division of the intermediate lines joining sides1 and 3 is weighted by 1.00000
The x coord. of the startpoint on side 1 is 0.700000E-02
The y coord. of the startpoint on side 1 is 0.000000
The x coord. of the endpoint on side 1 is 0.430000E-01
The y coord. of the endpoint on side 1 is 0.000000 560
The size ratio of cell at side 4 to that at side 2 is 1.00000
The x coord. of the startpoint on side 3 is 0.700000E-02
The y coord. of the startpoint on side 3 is 0.900000E-02
The x coord. of the endpoint on side 3 is 0.430000E-01
The y coord. of the endpoint on side 3 is 0.600000E-02
The size ratio of cell at side 4 to that at side 2 is 1.00000
The following data is for side 1
The side is an axis
The following data is for side 2
The side is an interface with other regions 570
The number of adjoining sides is 1
The following data is for matching side 1
The code of the side is 4
and it is in region 7
The x displacement to side is 0.000000
The y displacement to side is 0.000000
The following data is for side 3
The side is an interface with other regions
The number of adjoining sides is 1
The following data is for matching side 1 580
The code of the side is 1
and it is in region 10
The x displacement to side is 0.000000
The y displacement to side is 0.000000
The following data is for side 4
The side is an interface with other regions
The number of adjoining sides is 1
The following data is for matching side 1
The code of the side is 2
and it is in region 9 590
The x displacement to side is 0.000000
The y displacement to side is 0.000000
The following data is for region 9
Ratio of FNUM and DTM to the basic values are 1.00000
The number of cell segments along sides 1 and 3 is 10
The number of cell segments along sides 1 and 3 is 10
Side 1 is straight and the endpoints are specified
Side 3 is straight and the endpoints are specified
The segments along side 2 are of equal length
The segments along side 4 are of equal length 600
The division of the intermediate lines joining sides1 and 3 is weighted by 1.00000
The x coord. of the startpoint on side 1 is 0.430000E-01
The y coord. of the startpoint on side 1 is 0.000000
The x coord. of the endpoint on side 1 is 0.490000E-01
The y coord. of the endpoint on side 1 is 0.000000
The size ratio of cell at side 4 to that at side 2 is 1.00000
The x coord. of the startpoint on side 3 is 0.430000E-01
The y coord. of the startpoint on side 3 is 0.600000E-02

The x coord. of the endpoint on side 3 is 0.490000E-01
 The y coord. of the endpoint on side 3 is 0.160000E-01 610
 The size ratio of cell at side 4 to that at side 2 is 1.00000
 The following data is for side 1
 The side is an axis
 The following data is for side 2
 The side is an interface with other regions
 The number of adjoining sides is 1
 The following data is for matching side 1
 The code of the side is 4
 and it is in region 8
 The x displacement to side is 0.000000 620
 The y displacement to side is 0.000000
 The following data is for side 3
 The side is a vacuum or molecule entry
 The following data is for side 4
 The side is a vacuum or molecule entry
 The following data is for region 10
 Ratio of FNUM and DTM to the basic values are 1.00000
 The number of cell segments along sides 1 and 3 is 20
 The number of cell segments along sides 1 and 3 is 10
 Side 1 is straight and the endpoints are specified 630
 Side 3 is straight and the endpoints are specified
 The segments along side 2 are of equal length
 The segments along side 4 are of equal length
 The division of the intermediate lines joining sides 1 and 3 is weighted by 1.00000
 The x coord. of the startpoint on side 1 is 0.700000E-02
 The y coord. of the startpoint on side 1 is 0.900000E-02
 The x coord. of the endpoint on side 1 is 0.430000E-01
 The y coord. of the endpoint on side 1 is 0.600000E-02
 The size ratio of cell at side 4 to that at side 2 is 1.00000
 The x coord. of the startpoint on side 3 is 0.700000E-02 640
 The y coord. of the startpoint on side 3 is 0.250000E-01
 The x coord. of the endpoint on side 3 is 0.430000E-01
 The y coord. of the endpoint on side 3 is 0.250000E-01
 The size ratio of cell at side 4 to that at side 2 is 1.00000
 The following data is for side 1
 The side is an interface with other regions
 The number of adjoining sides is 1
 The following data is for matching side 1
 The code of the side is 3
 and it is in region 8 650
 The x displacement to side is 0.000000
 The y displacement to side is 0.000000
 The following data is for side 2
 The side is a solid surface
 Conditions are constant along the side
 The following data is for the whole side
 The following data is for species 1
 The surface temperature is 300.000
 The reflection is diffuse
 The fraction of molecules that are adsorbed is 0.000000 660
 The in-plane surface velocity is 0.000000
 The normal-to-plane surface velocity is 0.000000
 The catalytic fraction is 0.500000
 The following data is for species 2
 The surface temperature is 300.000
 The reflection is diffuse
 The fraction of molecules that are adsorbed is 0.000000
 The in-plane surface velocity is 0.000000
 The normal-to-plane surface velocity is 0.000000

The catalytic fraction is 0.000000 670
 The following data is for side 3
 The side is a stream boundary
 Conditions are constant along the side
 The following data is for the whole side
 The velocity comp. in the x direction is 0.000000
 The velocity comp. in the y direction is 0.000000
 The temperature is 300.000
 The number density is 0.555000E+18
 The fraction of species 1 is 0.000000
 The fraction of species 2 is 1.000000 680
 The following data is for side 4
 The side is a solid surface
 Conditions are constant along the side
 The following data is for the whole side
 The following data is for species 1
 The surface temperature is 300.000
 The reflection is diffuse
 The fraction of molecules that are adsorbed is 0.000000
 The in-plane surface velocity is 0.000000
 The normal-to-plane surface velocity is 0.000000 690
 The catalytic fraction is 0.500000
 The following data is for species 2
 The surface temperature is 300.000
 The reflection is diffuse
 The fraction of molecules that are adsorbed is 0.000000
 The in-plane surface velocity is 0.000000
 The normal-to-plane surface velocity is 0.000000
 The catalytic fraction is 0.000000
 Program stops when file is completed
 The file output side is in region 2 700
 and is side 4
 The number of mols in a record is 1000
 The total number of records is 5000
 The number of time steps in a sampling interval is 10
 The number of samples in a print interval is 20
 The number of samples to steady flow is 500
 At 80% steady flow time the number of molecules increases by a factor of 10
 The number of print intervals to STOP is 6000
 The maximum number of simulated molecules is 2000000

Appendix D

Time Of Flight

D.1 Time Of Flight analysis procedure

Time Of Flight (TOF) allows to determine the beam velocity, by analyzing the signal from the Quadrupole Mass Analyzer (QMA), when the beam is chopped by the disc called *wheel* (see chapter 2, section 2.2).

Since the slits on the wheel are narrow, the signal is quite small, so it is necessary to use the SEM (Secondary Electron Multiplier) in order to obtain a sufficient amplification. In this case the absolute value of the signal is in-influent for the analysis, because it is based on the waveform shape, rather than its amplitude; for this reason the SEM degradation in time is not a problem and an absolute calibration is not necessary.

The trigger for the acquisition is provided by a fast optical device (described in chapter 2, section 2.2).

The QMA signal in Volts is acquired by the computer *spinlab2* at a sampling speed of $1 \mu s$ and saved to human-readable text files by the program *TOF.vi*, shown in fig. D.1.

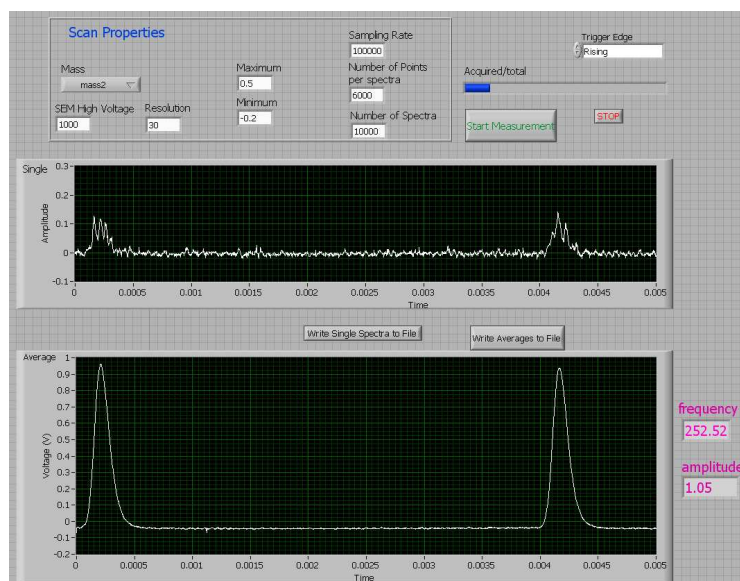


Figure D.1: TOF.vi front panel.

This program acquires thousands of single spectra (top panel) from the QMA and averages them in order to reduce the noise: the resulting waveform is shown in the bottom panel. The number of spectra to average is chosen depending on the experimental conditions that influence the signal amplitude (hydrogen/deuterium flux, nozzle temperature etc.).

The name of the output text file is chosen by the operator and usually contains details of the actual measurement step: hydrogen flux in case of flow-scan, nozzle temperature in case of temp-scan etc.

The file is composed by a header, that reports the acquisition time interval and the columns label, and two columns: time and QMA signal. The first column is not useful in this case, because its precision (1 minute) is too rough for this kind of fast signals. The second column reports the measured data from the QMA, in Volts. The raw data files are copied automatically every night from the acquisition PC *spinlab2* to the backup server *hermes1*, where they can be reformatted by the program *cleanup_single.csh*: it reads the file specified on the command line and produces an output file with the same name of the input file, but with extension *.txt*.

The resulting data-file is a text file with two columns and no labels: time in milliseconds, with a precision of $0.1 \mu s$, and QMA signal in millivolts, with a precision of $1 mV$. These

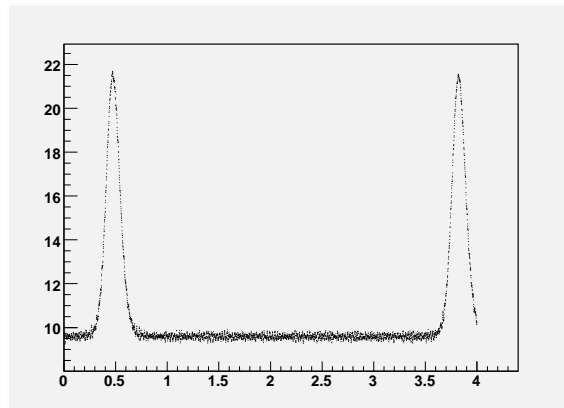


Figure D.2: Raw signal in mV from the QMA ($T_{noz} = 20K$, data set 1).

data are then plotted with *PAW* or *ROOT* (see fig. D.2) in order to check that the data were properly acquired and to extract some preliminary informations:

- background level of the signal in mV.
- estimation of the statistical fluctuations in mV.
- *wheel* frequency in Hz (standard frequency is about 150 Hz).

After this initial checks the procedure of analysis is the following:

- copy header.dat to FILENAME.dat (FILENAME is a name chosen by the operator).
- change the value of V_{err} in FILENAME.dat to match the statistical error estimated above.
- change the value of wheel frequency in FILENAME.dat according to the one measured above.

- change the value of the two geometrical parameters (beam radius and distance chop-beam) determined with calibrations.
- set the mass to the correct value (molecular/atomic hydrogen or deuterium).
- add to FILENAME.dat the first 2000 lines of the data-file.
- copy the file template.ctr to FILENAME.ctr.
- change the value of V_{off} in FILENAME.ctr to the background level determined above.
- change the value of T_{off} in FILENAME.ctr to the trigger offset determined with calibrations.
- change the value of τ_{Det} to the appropriate RC time constant of the electronics (electrometer preamplifier + cabling + NI PCI-board).
- if necessary to help the fit convergence change the starting values (first number in the row, after the label) of the three free parameters.
- run the script *runfit.csh* FILENAME (takes about 2 to 5 minutes to complete).

The result are written to the following text files:

- FILENAME.result: result of the fit (v_{drift} and t_{beam}).
- FILENAME.scan: summary of the input and output parameters.
- FILENAME.minuit: the raw output of the fitter minuit.
- FILENAME.conv: text file containing, in the third column, the waveform resulting from the fit.

In fig. D.3 is presented the result of the fit (red line) compared to the measured data (blue points); background level has already been subtracted from the measured data. From the fit result file *FILENAME.result* it is possible to obtain the beam temperature t_{beam} and beam drift velocity v_{drift} that is fundamental for rest gas attenuation measurements, presented in chapter 3.

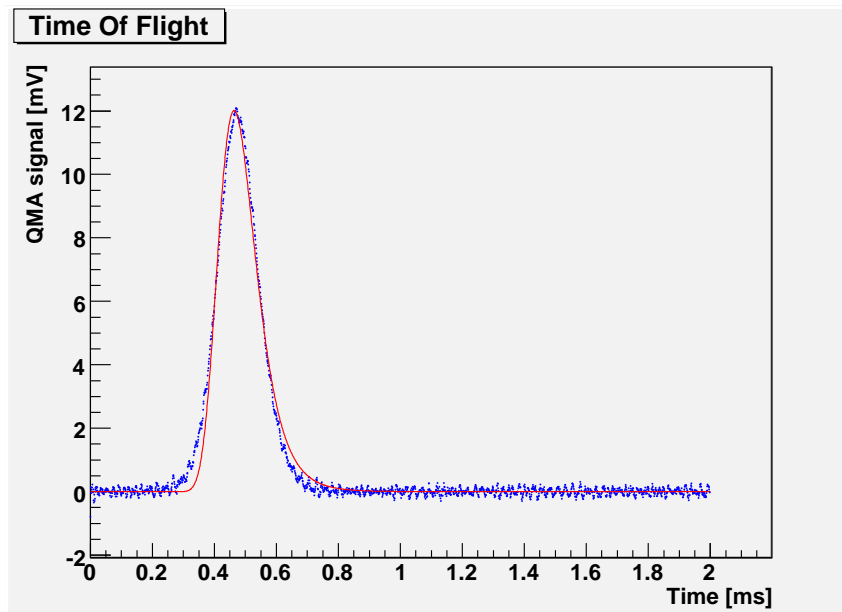


Figure D.3: Result of the fit (red line), compared to QMA measured signal (blue points), ($T_{noz} = 20K$, data set 1).

D.2 Program sources

D.2.1 cleanup_single.csh

```
#!/bin/tcsh
```

```
setenv LANG C
set file = $1
if ($file == "") then
echo "specify the input file"
exit
endif
```

```
set temp = ${file:r}
if ( -f ${temp:t}.txt ) then
echo "output file already existing"
exit
endif
```

```
awk 'if (NR>4) {printf("%7.4f %10.3f\n", (NR-5)*0.001+0.0005, 1000*$3)}' \
$file >! ${temp:t}.txt
```

10

D.2.2 header.dat

```
N. measurements..... 2000
Time step (ms)..... 0.001
```

```

Error on signal, Verr (mV)..... 0.
Mass (amu) ..... 2.000
Frequency (Hz) ..... 150.
Slit Radius (mm) ..... 1.000
Beam Radius (mm) ..... 0.600
Distance chop-beam (mm)..... 34.250
Distance chop-QMA (m)..... 0.510

```

10

```

Time (ms) Signal (mV)
-----

```

D.2.3 template.ctr

```

Time of Flight Deconvolution
 1 'Kamp'          0.85      0.001      0.0      1000.0
 2 'Voff (mV)'    95.00     5.0       0.0      500.0
 3 'vdrift(m/s)' 1040.0    20.0     50.0    4000.0
 4 'tbeam (K)'   47.0      0.1       0.5      250.0
 5 'toff (ms)'   0.0600    0.001     -1.0     1.0
 6 'tauDet(ms)' 0.001     0.0001

```

```

fix 2 6 5

```

```

migrad

```

10

```

call 3

```

```

save

```

```

y

```

```

exit

```

D.2.4 conv.inc

```

integer nptmax
parameter(nptmax=1000000)

common/convres/signal1(nptmax),signal2(nptmax),s1(nptmax),
& s2(nptmax)

real signal1,signal2
real s1,s2

common/comput/dt,ndt
double precision dt
integer ndt

common/vdparam/vnorm,c

```

10

```
double precision vnorm,c
```

D.2.5 labparam.inc

```
C*****
C
C Laboratory parameters
C-----
C alpha opening angle of chopper hole
C beta opening angle corresponding to beam diameter
C ngap number of chopper holes
C freq chopper frequency
C rbeam radius of atomic/molec. beam 10
C Dcb distance from chopper axis to beam axis
C Lcq distance from chopper to QMS
C tauDet RC response time of detection system
C Wion Width of the ionizing volume along the beam axis
C ttoff offset for time
C
C*****

common/labparam/alpha,beta,rbeam,Dcb,Lcq,freq,tauDet,
& invTauDet,bigT,mass,pi,Rhole,ttoff,wion,ngap 20
double precision alpha,beta,rbeam,Dcb,Lcq,freq,tauDet,
& invTauDet,bigT,pi,mass,Rhole,ttoff,wion
integer ngap
```

D.2.6 shared.inc

```
integer nmaxpnt
parameter(nmaxpnt=100000)

C Data from experiment
common/expdata/QMAsig(nmaxpnt),dtt,vverr
double precision QMAsig,dtt,vverr

C Parameters 10
common/parameters/Vd,Tbeam,Voff,toff,Kamp
double precision Vd,Tbeam,Voff,toff,Kamp
```

D.2.7 convolute.f

```
subroutine convolute
```

```

implicit none
integer i,j,ind

include 'conv.inc'
include 'labparam.inc'
include 'shared.inc'

```

10

C Variables for numerical integration

```

external veldis,conv1,conv1b,conv1c,conv1d,veldis2
double precision a,b,reltol,abstol,result,verr
integer nseg
1 real omega,am,kb
common/ul/tvar,Lcq1
double precision tvar,Lcq1

```

C Initialize and normalize velocity distribution

```

vnorm=1.0
am=1.6605E-4          ! atomic mass unit in E-23 kg
kb=1.38065            ! Boltzmann constant in E-23 J/K
c=0.5*mass*am/kb/tbeam
a=0.0
b=10000.0
reltol=0.0001
abstol=0.0
nseg=100

```

20

C veldis2 for Bird-style

```

C call DADAPT(veldis2,a,b,nseg,reltol,abstol,result,verr)
call DADAPT(veldis,a,b,nseg,reltol,abstol,result,verr)
vnorm=1000.0/result

```

30

C calculate bigT and invtaudet here

```

pi=3.14159
alpha=2.0*atan2(Rhole,Dcb) ! opening angle of chopper hole
beta=2.0*atan2(Rbeam,Dcb) ! opening angle of beam diameter
omega=freq*2.0*pi
bigT=(alpha+beta)/omega ! in seconds
invTauDet=1000.0/tauDet !taudet in ms, invtaudet in s-1
dt=dttd/1000.0          ! dttd in ms, dt in sec

```

40

C write(6,)bigT*

```


```

C Do first convolution (vel dist and opening function)

```

Lcq1=Lcq
do i=1,ndt
  b=i*dt
  tvar=b
  a=0.0
  reltol=0.0

```

50

```

        abstol=0.0001
        nseg=100
        call DADAPT(conv1,a,b,nseg,reltol,abstol,result,verr)
C 1b,1d = trapezoidal gate function
C 1,1b= standard veldis
C 1c,1d = new veldis2
C      call DADAPT(conv1b,a,b,nseg,reltol,abstol,result,verr)
C      call DADAPT(conv1c,a,b,nseg,reltol,abstol,result,verr)
C      call DADAPT(conv1d,a,b,nseg,reltol,abstol,result,verr)
        s1(i)=result
    enddo

C      call scopy      ! instead of one of the second convolutions below
C      call IVlength2  ! new method - correction is negligible
C      call IVlength   ! add finite length of ionization volume
        call tdetconv   ! add exp tail from electronics RC
C Now adjust for time offset
        call timeoffset

    return
end
C+++++

subroutine conv2(time,result)

implicit none
include 'labparam.inc'
double precision time,result
common/ul/tvar,Lcq1
double precision tvar,Lcq1

result=invtaudet*exp(-1.0*invtaudet*(tvar-time))

return
end
C+++++

double precision function conv1(time)

implicit none
include 'labparam.inc'
include 'conv.inc'
include 'shared.inc'
double precision time,vel,temp,a,b,omega
common/ul/tvar,Lcq1
double precision tvar,Lcq1

temp=tvar-time
if (temp.gt.bigT) then

```



```

        conv1=0.0
    else if (temp.lt.0) then
        write(6,*)"Bad time inside conv1"
    else
        vel=Lcq1/time
        conv1=vel*vel*vnorm*vel*vel*exp(-1.0*c*(vel-vd)**2.0)
C sine opening function
        conv1=conv1*sin(3.1416*temp/bigT)
    endif
end
C+++++
double precision function conv1b(time)

    implicit none
    include 'labparam.inc'
    include 'conv.inc'
    include 'shared.inc'
    double precision time,vel,temp,a,b,omega
    common/ul/tvar,Lcq1
    double precision tvar,Lcq1

    temp=tvar-time
    if (temp.gt.bigT) then
        conv1b=0.0
    else if (temp.lt.0) then
        write(6,*)"Bad time inside conv1"
    else
        vel=Lcq1/time
        conv1b=vel*vel*vnorm*vel*vel*exp(-1.0*c*(vel-vd)**2.0)
C trapezoid opening function
        omega=freq*2*3.1416
        if (alpha.le.beta) then
            a=alpha/omega
            b=(beta-alpha)/omega
        else
            a=beta/omega
            b=(alpha-beta)/omega
        endif
        if (temp.le.a) then
            conv1b=conv1b*temp/a
        else if (temp.gt.(a+b)) then
            conv1b=conv1b*(2*a+b-temp)/a
        endif
    endif
end
C+++++
double precision function conv1c(time)

```

```

implicit none
include 'labparam.inc'
include 'conv.inc'
include 'shared.inc'
double precision time,vel,temp,a,b,omega
common/ul/tvar,Lcq1
double precision tvar,Lcq1

temp=tvar-time
if (temp.gt.bigT) then
    conv1c=0.0
else if (temp.lt.0) then
    write(6,*)"Bad time inside conv1c"
else
    vel=Lcq1/time
    conv1c=vel*vel*vnorm*exp(-1.0*c*(vel-vd)**2.0)
C sine opening function
    conv1c=conv1c*sin(3.1416*temp/bigT)
endif
end
C+++++
double precision function conv1d(time)

implicit none
include 'labparam.inc'
include 'conv.inc'
include 'shared.inc'
double precision time,vel,temp,a,b,omega
common/ul/tvar,Lcq1
double precision tvar,Lcq1

temp=tvar-time
if (temp.gt.bigT) then
    conv1d=0.0
else if (temp.lt.0) then
    write(6,*)"Bad time inside conv1"
else
    vel=Lcq1/time
    conv1d=vel*vel*vnorm*exp(-1.0*c*(vel-vd)**2.0)
C trapezoid opening function
    omega=freq*2*3.1416
    if (alpha.le.beta) then
        a=alpha/omega
        b=(beta-alpha)/omega
    else
        a=beta/omega
        b=(alpha-beta)/omega
    endif

```

```

        if (temp.le.a) then
            conv1d=conv1d*temp/a
        else if (temp.gt.(a+b)) then
            conv1d=conv1d*(2*a+b-temp)/a
        endif
    endif
end
end
C+++++
double precision function veldis(vel)

implicit none
include 'conv.inc'
include 'shared.inc'
double precision vel

veldis=vnorm*vel*vel*exp(-1.0*c*(vel-vd)**2.0)

end
C+++++
double precision function veldis2(vel)

implicit none
include 'conv.inc'
include 'shared.inc'
double precision vel

veldis2=vnorm*exp(-1.0*c*(vel-vd)**2.0)

end
C+++++
subroutine writeresult

implicit none
include 'shared.inc'
include 'conv.inc'
integer i
real time
character*300 filename

call getenv('CURVE',filename)
if(filename(1:4).eq.'    ') then
    filename='signal.dat'
endif
time=-0.5*dtt
open(95,file=filename,status='unknown')
do i=1,ndt
    time=time+dtt
    write(95,1001)time,signal1(i),Kamp*signal2(i)

```

```

    enddo
1001 format(2x,f10.5,2x,f15.6,2x,f15.6)
    close(95)

    return
    end
C+++++ 250
    subroutine tdetconv
C moved here from inside convolute

    implicit none
    include 'conv.inc'
    include 'labparam.inc'
    include 'shared.inc'

    integer i,j
    double precision result,scale,time 260
    common/ul/tvar,Lcq1
    double precision tvar,Lcq1

C Do second convolution numerically, trapeziod rule
C chapter 4 of Numerical Methods in FORTRAN
    scale=dt*0.2
    s2(1)=s1(1)*scale
    call conv2(dt,result)
    s2(2)=s1(1)*0.5*result*scale 270
    call conv2(2*dt,result)
    s2(2)=s2(2)+s1(2)*0.5*result*scale
    do i=3,ndt
        tvar=i*dt
        call conv2(dt,result)
        s2(i)=s1(1)*0.5*result*scale
        do j=2,i-1
            time=j*dt
            call conv2(time,result)
            s2(i)=s2(i)+scale*result*s1(j) 280
        enddo
        time=i*dt
        call conv2(time,result)
        s2(i)=s2(i)+scale*0.5*s1(i)*result
    enddo

    return
    end
C+++++
    subroutine IVlength 290
C moved here from inside convolute

```

```

implicit none
include 'conv.inc'
include 'labparam.inc'
include 'shared.inc'

integer i,j,istart,indu,indl,iold
double precision hw,utime,ltime,scale,start,tvar
double precision uweight,lweight,norm
300

iold=0
hw=0.005*wion/Lcq ! dL/2L (wion in cm)
start=Lcq/15000.0 !start at 15000 m/s (upper limit for vel dist)
istart=nint(start/dt)
scale=dt*1000
do i=1,istart-1
    s2(i)=s1(i)*scale
enddo
do i=istart,ndt
310
    tvar=(i-0.5)*dt
    utime=(1.0+hw)*tvar
    ltime=(1.0-hw)*tvar
    indu=int(utime/dt)
    indl=int(ltime/dt)
    uweight=utime/dt-indu
    lweight=ltime/dt-indl
    if (indu.eq.indl) then
        uweight=uweight-lweight
        lweight=0.0
320
    else
        lweight=1.0-lweight
    endif
    indu=indu+1
    indl=indl+1
    s2(i)=uweight*s1(indu)+lweight*s1(indl)
C    s2(i)=uweight*(1.0+0.5*uweight)*(s1(indu)+s1(indu-1))*0.5
C    s2(i)=s2(i)+lweight*(1.0+0.5*lweight)*(s1(indl)+s1(indl+1))*0.5
if (indu-indl.gt.2) then
    do j=indl+1,indu-1
330
        s2(i)=s2(i)+s1(j)
    enddo
endif
    norm=uweight+lweight+indu-indl
    s2(i)=scale*s2(i)/tvar/norm
C    s2(i)=scale*s2(i)/tvar
C    write(6,*)indu-indl,tvar,utime,ltime,indu,indl,uweight,lweight
enddo

```

```

return
end

```

340

```

C+++++

```

```

subroutine IVlength2

```

```

implicit none
include 'conv.inc'
include 'labparam.inc'
include 'shared.inc'

```

350

```

integer i,j
external veldis,conv1,conv1b
double precision a,b,reltol,abstol,result,verr
integer nseg

```

```

common/ul/tvar,Lcq1
double precision tvar,Lcq1

```

```

C Rough numerical integration

```

360

```

do i=1,ndt
  b=i*dt
  tvar=b
  a=0.0
  reltol=0.0
  abstol=0.0001
  nseg=100
  s2(i)=2.0*s1(i)
  Lcq1=Lcq+0.01*wion*2.0
  call DADAPT(conv1,a,b,nseg,reltol,abstol,result,verr)
  s2(i)=s2(i)+result
  Lcq1=Lcq+0.005*wion*2.0
  call DADAPT(conv1,a,b,nseg,reltol,abstol,result,verr)
  s2(i)=s2(i)+2.0*result
  Lcq1=Lcq-0.005*wion*2.0
  call DADAPT(conv1,a,b,nseg,reltol,abstol,result,verr)
  s2(i)=s2(i)+2.0*result
  Lcq1=Lcq-0.01*wion*2.0
  call DADAPT(conv1,a,b,nseg,reltol,abstol,result,verr)
  s2(i)=s2(i)+result
  s2(1)=s2(1)/8.0

```

370

380

```

enddo

```

```

return
end

```

```

C+++++

```

```

subroutine scopy
                                                                 390
implicit none
include 'conv.inc'
include 'labparam.inc'
include 'shared.inc'

integer i,j,ind

do i=1,ndt
    s2(i)=s1(i)
enddo
return
end

```

C+++++

```

subroutine timeoffset
                                                                 410
implicit none
include 'conv.inc'
include 'labparam.inc'
include 'shared.inc'

integer i,j,ind

```

C *Now adjust for time offset*

```

if (ttoff.gt.0) then      ! move signal to the right
    j=nint(ttoff/dtt)
    do i=1,j
        signal1(i)=s1(1)
        signal2(i)=s2(1)
    enddo
    do i=1,ndt-j
        ind=i+j
        signal1(ind)=s1(i)
        signal2(ind)=s2(i)
    enddo
else                      ! move signal to the left
    j=nint(-1.0*ttoff/dtt)
    do i=1,ndt-j
        ind=i+j
        signal1(i)=s1(ind)
        signal2(i)=s2(ind)
    enddo
    do i=1,j
        ind=ndt-j+i

```

```

        signal1(ind)=s1(ndt)
        signal2(ind)=s2(ndt)
    enddo
endif

return
end

```

440

D.2.8 fitit.f

```

program fitit
implicit none

external chisq

open(99,file='result.dat',status='unknown')
call MINTIO(98,97,99)
call minuit(chisq,0)

stop
end

```

10

SUBROUTINE CHISQ(NPAR,G,F,X,IFLAG,FUTIL)

```

implicit none

include 'conv.inc'
include 'shared.inc'
include 'labparam.inc'

```

20

```

integer i

```

C Arguments: x is the array of parameters
C npar is the number of parameters
C F is the value of the function returned to the calling
C program
C iflag tells chisq what to do (1 => init, 2=> calculate
C 3 => wrap up)

```

integer iflag,npar
double precision f,x,g,futil
dimension x(*),g(*)
double precision chi2,sum
integer indoff,icount
double precision ep1,em1,epa1,ep3,ep4,em3,em4,epa3,epa4,globcc

```

30

```

Kamp=X(1)

```

```

Voff=X(2)

```

```

vd=X(3)

```



```

    tbeam=X(4)
    toff=X(5)
    tauDet=X(6)
    ngap=1
    ttoff=toff
    wion=1.0 ! length of IV in cm

```

C... Initialization

```

IF(IFLAG.eq.1) CALL READDATA
call convolute

```

C... Loop over measurements and calculate the chisq for each

```

sum=0.0
icount=0
C   indoff=nint(toff/dtt)
do i=1,ndt
    chi2=(QMAsig(i)-Voff)-(Kamp*signal2(i))
    sum=sum+chi2*chi2
enddo
f=sum/ndt/vverr/vverr

```

C... Dump minuit results to file

```

IF(IFLAG.EQ.3) then
    call MNERRS(1,ep1,em1,epa1,globcc)
    call MNERRS(3,ep3,em3,epa3,globcc)
    call MNERRS(4,ep4,em4,epa4,globcc)
    call writeresult ! dump convoluted curve to file
    write(95,1234)vd,epa3,tbeam,epa4,Kamp,epa1,toff,Rbeam,Dcb,Lcq,f
1234 format(4(f8.2,1x),2(f8.4,1x),f8.4,1x,3(f6.2,1x),f10.4)
endif

```

return

```

end

```

C*****

```

subroutine readdata

implicit none
include 'shared.inc'
include 'labparam.inc'
include 'conv.inc'
integer i
real time
character*40 temp
character*300 filename

call getenv('DATAIN',filename)

```

```

if(filename(1:4).eq.'    ') then
  filename='datain.dat'
endif
                                                                    90

open(91,file=filename,status='unknown')
read(91,5041)temp,ndt
read(91,5042)temp,dtc
read(91,5042)temp,vverr
read(91,5042)temp,mass
read(91,5042)temp,freq
read(91,5042)temp,Rhole
read(91,5042)temp,Rbeam
read(91,5042)temp,Dcb
read(91,5042)temp,Lcq
                                                                    100
5041 format(a37,4x,i12)
5042 format(a37,4x,f12.3)
write(6,*)"ndt: ",ndt," dtc: ",dtc," vverr: ",vverr
write(6,*)"mass: ",mass," freq: ",freq," Rhole: ",rhole
write(6,*)"Rbeam: ",rbeam," dcb: ",dcb," Lcq: ",lcq
if (vverr.le.0) then
  write(6,*)" zero value for vverr"
  vverr=1.0
endif
read(91,5043)
                                                                    110
5043 format(//)
do i=1,ndt
  read(91,*,end=101)time,QMAsig(i)
enddo
101 continue
close(91)
if (i.lt.ndt) then
  write(6,*)"insufficient data points ",i," instead of ",ndt
  ndt=i-1
endif
                                                                    120

return
end

```

D.2.9 runfit.csh

```

#!/bin/tcsh

cp $1.ctr fort.98
rm $1.conv
setenv CURVE $1.conv

setenv DATAIN $1.dat

```

```
#nice ./fitit.x >E! $1.out  
nice ./fitit.x
```

10

```
# minuit dialog  
mv fort.97 $1.minuit  
# parameters only  
mv result.dat $1.result  
cat fort.95 >> $1.scan
```


List of Figures

1.1	Elastic Scattering.	4
1.2	(a) Deep Inelastic Scattering, (b) Semi Inclusive Deep Inelastic Scattering.	4
2.1	Atomic Beam Source “ABS1” scheme. (a) dissociator, (b) skimmer, (c) Compression Volume, (RG inlet) Rest Gas inlet.	11
2.2	ABS1 dissociator. (MW) Microwave cavity, (1) Water cooling, (2) Collar, (3) Nozzle.	12
2.3	Available Nozzles: (a) sonic 4 mm, (b) sonic 2 mm, (c) trumpet 2 mm.	13
2.4	Skimmers: 6 mm diameter (left) and 2 mm diameter (right).	13
2.5	Diagnostic system composed of Compression Volume (CV), Chamber 3 (CW chamber) and Chamber 4 (QMA chamber).	14
2.6	ABS1 compression tube geometry. Its conductance is equivalent to a cylindrical tube of 10 cm length and 1 cm diameter.	15
2.7	Calibrated gas injection system connected to the Compression Volume (H): (G) compression tube, (I) constant pressure volume (V_{cal}), (J) Regulating Valve, (K) Hydrogen gas buffer, (L) calibrated volume.	15
2.8	Chopper (left) and Wheel (right) geometries.	16
2.9	Chopper signal directly seen on a digital oscilloscope. Single spectrum (no average).	17
2.10	Chopper signal (average of 40 spectra) obtained with Labview dedicated program.	17
2.11	Quadrupole Mass Analyzer scheme (model Pfeiffer QMA-410).	18
2.12	Scheme of the regulating electronic circuit.	19
2.13	Scheme of electrical connections of the regulating circuit.	20
2.14	Chopper frequency stability check before the implementation of the stabilization circuit. Top panel shows measured frequency f , while bottom panel shows ratio between f and setpoint $f_0 = 16.5 \text{ Hz}$	21
2.15	Chopper frequency stability check after the implementation of the stabilization circuit. Top panel shows measured frequency f , while bottom panel shows ratio between f and setpoint $f_0 = 16.5 \text{ Hz}$ (vertical scales are different from the previous picture).	21
2.16	Detail of the detection system showing the distance between <i>wheel</i> and QMA.	22
2.17	Time Of Flight basic scheme. The areas highlighted in grey represent the evolution of the shape of the signal while it travels from the wheel to the detector.	23

2.18	Atomic Beam Source “ABS2”: (A) Dissociator, (B) nozzle, (C) skimmer, (D) sextupole magnets, (E) RF transition units, (F) injection tube, (CV) compression volume.	25
2.19	ABS2 pumping system. (A) Prevacuum Leybold trivac D60A pump, (B) Root Pfeiffer WKP250A SP pump, (C) Root Leybold ruvac WSU1001H pump, (D) Turbomolecular Pfeiffer TPU2200 pumps, (E) Cryogenic Ricor coolstar 1500 pump, (F) Cryogenic Varian HV8 pump, (G) Cryogenic Varian HV8 pump.	26
2.20	ABS2 nozzle and skimmer detail: (a) water cooling, (b) indium vacuum seal, (c) PTFE thermal insulator, (d) liquid N_2 cooling, (e) copper to pyrex indium joint, (f) nozzle, (g) skimmer, (h) collimator, (i) first magnet element.	27
2.21	Magnetization direction of a 24-segments sextupolar permanent magnet.	28
2.22	Measured quadratic coefficient k for the magnetic field in a 12 segment conical bore permanent sextupole magnet. The dashed line shows the field calculated. The points correspond to the measured data.	29
2.23	Data acquisition system scheme for ABS1.	31
2.24	Control_ABS1.vi front panel.	32
2.25	MonitPx_Pressioni.vi front panel.	33
2.26	Data acquisition system scheme for ABS2.	36
2.27	MonitPx_ABS2.vi front panel.	37
2.28	FOX box front panel with LCD display, reboot button, LCD contrast adjust knob and control buttons.	39
3.1	RHIC ABS beam intensity (in arbitrary units) as a function of input flux.	41
3.2	Atomic Beam Sources intensities in [<i>atoms/s</i>] listed according to publication year.	42
3.3	Nozzles geometries. Left: 2 mm (standard), right: 4mm.	45
3.4	Data analysis first step. Pressure in scattering chamber (Chamber 2) and raw signal from QMA are plotted as a function of time ($T_{noz} = 20K$, data set 1).	51
3.5	Data analysis procedure. In the left panel the QMA raw signal is plotted as a function of the Chamber 2 pressure. In the right panel a correction for time drift (see eq. 3.7) has been applied to the QMA signal and transition points (those outside the red lines in left panel) have been removed; the fit is performed on the remaining data. ($T_{noz} = 20K$, data set 1).	51
3.6	Measured attenuation coefficient for molecular hydrogen beams as function of nozzle temperature (top panel) and beam mean velocity (bottom panel).	54
3.7	Measured attenuation coefficient for deuterium molecular beams as function of beam mean velocity.	55
3.8	Measured attenuation coefficient for hydrogen and deuterium atomic beam as function of beam mean velocity.	56
3.9	Attenuation coefficient A_n for molecular deuterium. Black triangles are the measured data, pink squares (top panel) are the data calculated using HS model and green squares (bottom panel) are the data calculated using VSS model.	57
3.10	Measured and calculated values of A_n for different σ_{eff} models and values of the mean beam velocity.	58

4.1	Example of storage cell geometry.	59
4.2	Standard injection tube (left) and finned injection tube (right).	60
4.3	Injection tubes produced: 0, 5, 10, 12 fins.	61
4.4	Calibrated gas injection system connected to the Compression Volume (H): (F) Chamber 5, (G) injection tube, (I) constant pressure volume (V_{cal}), (J)Regulating Valve, (K) Hydrogen gas buffer, (L) calibrated volume. . . .	62
4.5	Measured (black squares) and calculated (line) conductance ratio as func- tion of fins number. C_0 is the conductance in case of a tube without fins. . .	63
4.6	Left panel: measured P_{CV} in function of number of fins. Right panel: calculated transmitted beam intensity in function of number of fins.	64
4.7	Present design for future PAX storage cell.	65
4.8	Estimated thickness for different fin length and number for the PAX cell geometry.	66
4.9	Survival fraction as a function of fins number: measured data and fits for different starting surfaces.	67
4.10	Distribution of L_z in case of no fins tube (top panel) and 10-fins tube (bottom panel). The three lines correspond to different starting surface diameters.	68
5.1	Standard <i>sonic</i> nozzle (a) and <i>trumpet</i> nozzle (b).	71
5.2	Simulation geometry. (A) nozzle, (B) skimmer, (C) collimator. Numbers indicate the simulation regions.	72
5.3	Scheme of a flow-field region.	73
5.4	Gas number density obtained from the output of DS2G (simulation “trum- pet2b”).	76
5.5	Result of root analysis for Chamber 2 data. Pressure HV2b is plotted as a function of the hydrogen flux through the nozzle.	79
5.6	Chamber 2 fluxes comparison. Label ‘3’ corresponds to <i>sonic</i> nozzle data, label ‘4’ to <i>trumpet</i> nozzle data.	80
5.7	QMA density comparison. Label ‘3’ corresponds to <i>sonic</i> nozzle, label ‘4’ to <i>trumpet</i> nozzle.	81
5.8	Chamber 2 fluxes comparison. Label ‘3’ corresponds to <i>sonic</i> nozzle, label ‘4’ to <i>trumpet</i> nozzle. Data are corrected for beam attenuation in Chamber 2. . .	82
A.1	Atom inside a sextupolar magnet. The indicated trajectory corresponds to the maximum accepted angle α_m . The beam axis is coincident with the magnetic axis (z).	84
B.1	Relative velocity between beam particle and RG.	90
D.1	TOF.vi front panel.	107
D.2	Raw signal in mV from the QMA ($T_{noz} = 20K$, data set 1).	108
D.3	Result of the fit (red line), compared to QMA measured signal (blue points), ($T_{noz} = 20K$, data set 1).	110

List of Tables

2.1	Vacuum pumps	26
2.2	Magnets geometry (element number follows beam direction)	28
3.1	Nozzle temperatures	45
3.2	Data sets	47
3.3	Fixed parameters for hydrogen	47
3.4	Fixed parameters for deuterium	47
3.5	Acquired data	48
3.6	Data set 1	49
3.7	Data set 2 and 3	49
3.8	Data set 4	50
3.9	Rest Gas attenuation data for sets 1 and 2	52
3.10	Rest Gas attenuation data for sets 3 and 4	53
5.1	Simulation parameters	73
5.2	Monte-Carlo input data	74
5.3	Monte-Carlo Simulations data	75
5.4	Ratio of simulated fluxes	75
5.5	SCAN results	76
5.6	Hydrogen fluxes	77
5.7	Nozz-skim distances	77
5.8	Fixed parameters	77

Bibliography

Introduction

- [1] **PAX Technical Proposal**
<http://www.fz-juelich.de/ikp/pax>
- [2] **Proceedings of 2nd International Symposium on Polarization Phenomena of Nucleons**
W. Haeberli, Supplementum vol. 12, p. 64 (1966)
- [3] **Spin physics at HERMES** - D. Hasch, AIP Conf. Proc. 915 p. 307 (2007)
- [4] **Polarized gas targets**
W. Haeberli and E. Steffens, Rep. Prog. Phys. 66, p. 1887 (2003)
- [5] **Consistent definitions for, and relationships among, cross sections for elastic scattering of hydrogen ions, atoms, and molecules**
P. S. Krstic and D. R. Schultz, Phys. Rev. A60, p. 2118 (1999)
- [6] **Experimental determination of total H⁰-H⁰ scattering cross section at 2 K from intrabeam collisions**
A. Hershcovitch, Phys. Rev. Lett. 63, p. 750 (1989)
- [7] **Low conductance injection tubes for storage cell targets** - L. Barion, M. Capiluppi, G. Ciullo, M. Contalbrigo, P.F. Dalpiaz, A. Drago, P. Lenisa, M. Stancari, M. Statera, E. Steffens, M. Wang, NIM A 594, p. 126 (2008)

Chapter 1: Spin-physics and polarized antiprotons

- [8] **The Scattering of the α and β Rays and the Structure of the Atom**
E. Rutherford, Proceedings of the Manch. Lit. and Phil. Soc., IV 55, 1820 (1911)
- [9] **Magnetic deflection of hydrogen molecules and the magnetic moment of the proton. I**
Frisch and Stern, Zeits. f. Physik 85, p. 4 (1933)
- [10] **Magnetic deflection of hydrogen molecules and the magnetic moment of the proton. II**
Estermann and Stern, Zeits. f. Physik 85, p. 17 (1933)

-
- [11] **Electron Scattering from the Proton**
R. Hofstadter and R. W. McAllister, Phys. Rev. Lett. 98, p. 217 (1955)
- [12] **Elastic Scattering of 188-Mev Electrons from the Proton and the Alpha Particle**
R. W. McAllister and R. Hofstadter, Phys. Rev. Lett. 102, p. 851 (1956)
- [13] **Observed behavior of highly inelastic electron - proton scattering**
M. Breidenbach et al., Phys. Rev. Lett. 23, p. 935 (1969)
- [14] **High-energy inelastic e - p scattering at 6° and 10°**
E. D. Bloom et al., Phys. Rev. Lett. 23, p. 930 (1969)
- [15] **Inelastic Electron-Proton and γ -Proton Scattering and the Structure of the Nucleon** J. D. Bjorken and E. A. Paschos Phys. Rev. 185, p. 1975 (1969)
- [16] **A schematic model of baryons and mesons**
M. Gellmann, Phys. Rev. Lett. 8, p. 214 (1964)
- [17] **A measurement of the spin asymmetry and determination of the structure function g1 in deep inelastic muon-proton scattering; An investigation of the spin structure of the proton in deep inelastic scattering of polarised muons on polarised protons**
Ashman J., et al., Phys. Rev. Lett. B 206, p 364 (1988); Nucl. Phys. B 328, p. 1 (1989)
- [18] **A measurement of the spin asymmetry and determination of the structure function g1 in deep inelastic muon proton scattering**
J. Ashman et al., Phys. Rev. Lett. B206, p. 206 (1988)
- [19] **Transversity and Collins functions from SIDIS and e+ e- data - M. Anselmino, M. Boglione, U. D'Alesio, A. Kotzinian, F. Murgia, A. Prokudin, and C. Trk, Phys. Rev. D 75, 054032 (2007)**
- [20] **Polarized Anti-protons - the Quest for a Missing Tool** E. Steffens, Proceedings of workshop "SPIN 2008" (to be published)
- [21] **Polarized beams at SSC (Ann Arbor, MI 1985) // Polarized antiprotons (Bodega Bay, CA 1985): proceedings**
Workshop on Polarized Beams at SSC, Ann Arbor, Mich., Jun 14, 1985 AND Workshop on Polarized Antiproton Sources, Bodega Bay, Calif., Apr 18-21, 1985 Editors A.D. Kirsch, A.M.T. Lin, O. Chamberlain. 1986 American Inst. Phys. AIP Conference Proceedings, 145
- [22] **Proceedings of the 8th International Symposium on High-Energy Spin Physics, Minneapolis 1988**
A. Yokosawa, K.J. Heller (edt), AIP Conf. Proc. 187 (1989)
- [23] **Proceedings of workshop "Polarized Antiproton Beams - How?"**
Cockcroft Institute, Daresbury (2007)

- [24] **Nuclear Studies with Neutrons**
F.L. Shapiro, Proc.Int.Conf. Study on Nucl. Structure with Neutrons, Antwerp 1965, North-Holland, p. 588 (1966)
- [25] **Proc 3rd Int. Symp.on Polarization Phenomena in Nuclear Reactions**
G.A. Keyworth and J.R.Lemley, Madison, p873 (1970)
- [26] **Neutron polarization with a polarized ^3He spin filter**
K.P. Coulter et al. NIM A 288, p. 463 (1990)
- [27] **Could we build polarized proton storage rings?**
P.L. Csonka, NIM 63, p. 247 (1968)
- [28] **Proceedings of the 2nd LEAR Workshop**
K. Kilian and D. Mohl, Erice, p. 701 (1982)
- [29] **Proceedings of the 3rd LEAR Workshop**
E. Steffens et al., Tignes p. 245 and CERN/PSCC/85-80 (1985)
- [30] **New method to polarize protons in a storage ring and implications to polarize antiprotons**
F. Rathmann et al., Phys. Rev. Lett. 71, p. 1379 (1993)
- [31] **Nucleon-nucleon partial-wave analysis to 1100 MeV**
R.A. Arndt, J.S.Hyslop III and I.D.Roper, Phys Rev D 35, p. 128 (1987)
- [32]
F. Rathmann, Ph. D. thesis, Phillips-Universitaet Marburg (1994)
- [33] **Polarizing a stored proton beam by spin flip?**
H.O. Meyer et al., to be published
- [34] **Effect of a polarized hydrogen target on the polarization of a stored proton beam**
H.O. Meyer, Phys. Rev. E 50, p. 1485 (1994)
- [35] **Proton-proton spin correlation measurements at 200 MeV with an internal target in a storage ring** - W. Haeberli et al., Phys. Rev. C 55, p. 597 (1997)
- [36] **Polarizing stored beams by interaction with polarized electrons** - C. J. Horowitz and H. O. Meyer, Phys. Rev. Lett. 72, p. 3981 (1994)
- [37] **Polarizing mechanisms for stored p and pbar beams interacting with a polarized target** - A.I. Milstein and V.M. Strakhovenko Phys. Rev. E 72, 066503 (2005)
- [38] **Spin filtering in storage rings** - N.N. Nikolaev, F.F. Pavlov, arXiv:hep-ph/0512051v1 (2005)
- [39] **A surprising method for polarising antiprotons**
T. Walcher et al., EPJ A 34, p. 447 (2007)

- [40] **Measurement of the depolarizing p(pol)e cross section using co-moving electrons (Proposal)**
<http://www.fz-juelich.de/ikp/pax/proposals/files/proposal20071020.pdf> (2007)
- [41] **Depolarization measurements at COSY**
Hans Strher, VIQCD meeting, Ferrara, June 1 (2008)
- [42] **Letter Of Intent for Measurement of the spin dependence of the pbar-p interaction at the AD ring - PAX Collaboration, arXiv:hep-ex/0512021** (2005)

Chapter 2: The Spinlab facility in Ferrara

- [43] **Metodologie ottiche per la diagnostica di fasci atomici polarizzati intensi di idrogeno e deuterio**
L. Barion, Diploma Thesis, Università di Ferrara (2005)
- [44] **The waveguide surfatron: a high power surface-wave launcher to sustain large-diameter dense plasma columns**
M. Moisan et al., J. Phys E 20, p. 1356 (1987)
- [45] **SDCC - Small Device C Compiler**
<http://sdcc.sourceforge.net/>
- [46] **Picprog - PIC16, PIC12 and PIC18 microcontroller programmer for Linux**
<http://hyvatti.iki.fi/~jaakko/pic/picprog.html> - Jaakko Hyvätti
- [47] **PIC-Programmer 2 for PIC16C84**
<http://www.jdm.homepage.dk/newpics.htm> - Jens Dyekjaer Madsen
- [48] **A high-brightness source for polarized atomic hydrogen and deuterium**
T. Wise, A.D. Roberts and W. Haeberli, NIM A 336 p. 410 (1993)
- [49] **Medium field rf transitions for polarized beams of hydrogen and deuterium**
A.D. Roberts, P. Elmer, M.A. Ross, T. Wise and W. Haeberli, NIM A 322, p. 6 (1992)
- [50] **National Instruments**
<http://www.ni.com/>
- [51] **Acme Systems**
<http://acmesystems.it/>
- [52] **Idam**
http://www.icpdas.com/products/Remote_IO/i-7000/i-7000_introduction.htm

Chapter 3: Rest Gas Attenuation

- [53] **An optimization study for the RHIC polarized jet target**
T. Wise, M.A. Chapman, W. Haeberli, H. Kolsterb, P.A. Quin, NIM A 556, p 1 (2006)

-
- [54] **Absolute polarized H-jet polarimeter development, for RHIC**
A. Zelenski et al., NIM A 536, p.248 (2005)
- [55] **Sources of polarized ions**
W. Haeberli, Ann. Rev. Nucl. Sci. 17, p. 373 (1967)
- [56] **High field superconducting sextupoles magnets**
L.G. Isaeva et al., NIM A 411, p. 201 (1998)
- [57] **Molecular Gas Dynamics and the Direct Simulation of Gas Flows**
G.A. Bird, Oxford University Press (1994)
- [58] **“Atom, molecule and cluster Beams I & II”**
H. Pauly, (2000)
- [59] **A study on the Production of Intense Cold Atomic Beams for Polarized Hydrogen and Deuterium Targets**
N. Koch, Ph.D theis, Friedrich-Alexander-Universitaet Erlangen-Nuernberg, DESY-THESIS-1999-015 (1999)

Chapter 4: Finned injection tubes

- [60] **Internal target experiments in the storage rings**
D. Toporkov, XL PNPI Winter School, 24 February 2006
- [61] **Proceedings of the Workshop on Polarized Gas Targets for Storage Rings**
H.-G. Gaul, E. Steffens, K. Zapfe, MPI Kernphysik Internal Report, p. 4550 (1991)